Universidad de Valladolid

Escuela de Doctorado Universidad de Valladolid

PROGRAMA DE DOCTORADO EN INGENIERÍA INDUSTRIAL

TESIS DOCTORAL:

IMÁGENES DE ELECTROLUMINESCENCIA Y FOTOLUMINESCENCIA NO INVASIVA MEDIANTE ELECTRÓNICA A NIVEL DE MÓDULO EN PLANTAS FOTOVOLTAICAS

Presentada por Alberto Gregorio Redondo Plaza para
optar al grado de
Doctor por la Universidad de Valladolid

Dirigida por:
Dr. Luis Hernández Callejo
Dr. Victor Alonso Gómez

Universidad de Valladolid

Escuela de Doctorado Universidad de Valladolid

PHD PROGRAMME IN INDUSTRIAL ENGINEERING

DOCTORAL THESIS:

NON-INVASIVE ELECTROLUMINESCENCE AND PHOTOLUMINESCENCE IMAGING THROUGH MODULE-LEVEL ELECTRONICS IN PHOTOVOLTAIC POWER PLANTS

Submitted by Alberto Gregorio Redondo Plaza in fulfilment of the requirements for the PhD degree by the Universidad de Valladolid

Supervised by:
Dr. Luis Hernández Callejo
Dr. Victor Alonso Gómez

Acknowledgments / Agradecimientos

El proceso de esta tesis, aunque en algunos momentos ha sido duro y lleno de desafíos, ha resultado una experiencia muy enriquecedora tanto a nivel académico como personal. Este logro no es únicamente mío, ya que no habría sido posible sin la ayuda y el apoyo de muchas personas que me han acompañado a lo largo de este camino.

Quisiera comenzar agradeciendo a mis directores y tutor de tesis, quienes me introdujeron al mundo de la investigación y me han guiado durante todo este proceso. Su dedicación y conocimientos han sido fundamentales para mi formación y la realización de este trabajo. También quiero agradecer a mis compañeros del departamento, así como a los investigadores y docentes con los que he tenido la oportunidad de colaborar durante las estancias que he realizado. Todas estas experiencias han sido muy valiosas y permanecerán siempre en mi recuerdo.

Quisiera expresar también mi agradecimiento a la Universidad de Valladolid por brindarme la oportunidad de desarrollar esta tesis, así como al Ministerio de Universidades por la financiación de mi contrato predoctoral. De igual manera, agradezco todas las ayudas que han hecho posibles las estancias de investigación y la asistencia a congresos, así como los diversos proyectos de investigación que han permitido la adquisición del material y los equipos necesarios para llevar a cabo este trabajo.

Finalmente, quiero dar las gracias a mis seres más cercanos. A mis amigos, por ser un apoyo y una forma de desconexión en los momentos más difíciles. A mi pareja, por acompañarme y apoyarme incondicionalmente durante todo este proceso. Y, por supuesto, a mi familia, por la educación y los valores que me han transmitido; especialmente a mi madre, cuyo sacrificio y ejemplo me han permitido llegar hasta aquí.

A todos ustedes, mi más sincero agradecimiento.

Abstract

Photovoltaic technology has experienced a rapid increase in global capacity in recent years, becoming one of the renewable energy sources with the greatest potential. The operation and maintenance of photovoltaic plants require inspection techniques to detect faults and analyse degradation. Among the most common inspection methods for in-field modules are current-voltage curve tracing, infrared thermography, and luminescence imaging. Luminescence imaging (electroluminescence and photoluminescence) is particularly valuable, as it reveals the internal structure of solar cells, enabling fault detection and performance assessment.

Conventional luminescence imaging relies on acquiring the electroluminescence signal under dark conditions, requiring module disconnection, external power supplies, and nighttime measurements. These requirements make the method invasive, slow, and logistically complex. This thesis explores non-invasive, daylight-capable luminescence imaging based on module-level electronic devices to overcome the main drawbacks of the conventional technique.

Chapter I presents the research background and motivation for developing and improving non-invasive luminescence imaging techniques, as well as the general and specific objectives of the thesis, which are aligned with the following chapters. **Chapter II** provides the theoretical and technical background that facilitates a better understanding of the subsequent chapters, especially for readers without deep expertise in the field. **Chapter III** reviews the state of the art of luminescence techniques in photovoltaic power plants, highlighting the novelty of the proposed research.

Chapter IV describes the design and validation of an electronic architecture that enables the modulation of both electroluminescence and photoluminescence signals. The installation of this device at the module level allows electroluminescence and photoluminescence imaging to be performed non-invasively. Furthermore, these measurements do not require external power sources and can be carried out during daytime operation of the photovoltaic plant.

In **Chapter V**, different strategies are explored to extract the luminescence signal from the background generated by sunlight. First, time-domain processing is studied using two approaches: a synchronous strategy, which requires continuous communication between the developed electronic device and the camera; and an asynchronous strategy, which does not require continuous communication and relies on an algorithm to automatically classify the images. Secondly, frequency-domain processing based on the Fast Fourier Transform is successfully validated, enabling effective background removal when luminescence is modulated with any periodic waveform.

In **Chapter VI**, photoluminescence signal modulation is integrated into the topology of a module-level photovoltaic optimizer. Additionally, current-voltage curve tracing is incorporated. The resulting device integrates maximum power point tracking together with photoluminescence modulation and current-voltage curve tracing in a non-invasive manner, two inspection techniques that are conventionally invasive.

Finally, **Chapter VII** summarizes the main conclusions of the thesis, highlighting its innovations and key contributions.

Resumen

La tecnología fotovoltaica ha experimentado un rápido aumento de capacidad a nivel mundial en los últimos años, convirtiéndose en una de las fuentes de energía renovable con mayor potencial. La operación y el mantenimiento de las plantas fotovoltaicas requieren técnicas de inspección para detectar fallos y analizar la degradación. Entre los métodos de inspección más comunes aplicados a los módulos en campo se encuentran el trazado de curvas corriente-tensión, la termografía infrarroja y la obtención de imágenes de luminiscencia. Las imágenes de luminiscencia (electroluminiscencia y fotoluminiscencia) son especialmente valiosas, ya que revelan la estructura interna de las células solares, lo que permite detectar defectos y evaluar el rendimiento.

La obtención convencional de imágenes de luminiscencia se basa en la adquisición de la señal de electroluminiscencia en condiciones de oscuridad, lo que requiere la desconexión de los módulos, fuentes de alimentación externas y mediciones nocturnas. Estos requisitos hacen que el método sea invasivo, lento y logísticamente complejo. Esta tesis explora una técnica de obtención de imágenes de luminiscencia no invasiva y operativa a la luz del día, basada en dispositivos electrónicos a nivel de módulo, con el objetivo de superar las principales limitaciones del enfoque convencional.

El **Capítulo I** presenta el contexto de la investigación y la motivación para desarrollar y mejorar las técnicas de obtención de imágenes de luminiscencia no invasiva, así como los objetivos generales y específicos de la tesis, que se alinean con los capítulos posteriores. El **Capítulo II** proporciona los fundamentos teóricos y técnicos que facilitan una mejor comprensión de los capítulos siguientes, especialmente para los lectores sin una formación profunda en el área. El **Capítulo III** revisa el estado del arte de las técnicas de luminiscencia aplicadas a plantas fotovoltaicas, destacando la novedad de la investigación propuesta.

El **Capítulo IV** describe el diseño y la validación de una arquitectura electrónica que permite la modulación tanto de señales de electroluminiscencia como de fotoluminiscencia. La instalación de este dispositivo a nivel de módulo posibilita la obtención de imágenes de electroluminiscencia y fotoluminiscencia de forma no invasiva. Además, estas mediciones no requieren fuentes de energía externas y pueden realizarse durante el funcionamiento diurno normal de la planta fotovoltaica.

En el **Capítulo V** se exploran diferentes estrategias para extraer la señal de luminiscencia del fondo generado por la luz solar. En primer lugar, se estudia el procesamiento en el dominio temporal mediante dos enfoques: una estrategia síncrona, que requiere comunicación continua entre el dispositivo electrónico desarrollado y la cámara; y una estrategia asíncrona, que no requiere comunicación continua y se basa en un algoritmo que clasifica automáticamente las imágenes. En segundo lugar, se valida con éxito el procesamiento en el dominio frecuencial basado en la Transformada Rápida de Fourier, que permite eliminar eficazmente la señal de fondo cuando la luminiscencia se modula con cualquier forma de onda periódica.

En el **Capítulo VI**, la modulación de la señal de fotoluminiscencia se integra en la topología de un optimizador fotovoltaico a nivel de módulo. Además, se incorpora el trazado de curvas corriente-tensión. El dispositivo resultante integra el seguimiento del punto de máxima potencia junto con la modulación de fotoluminiscencia y el trazado de curvas corriente-tensión de manera no invasiva, dos técnicas de inspección que convencionalmente son invasivas.

Finalmente, el **Capítulo VII** resume las principales conclusiones de la tesis, destacando sus innovaciones y contribuciones más relevantes.

Index

List of Figures

List of Tables

List of Acronyms and Abreviations

AC	Alternating Current
ADC	Analog-to-Digital Converter
a-Si	Amorphous Silicon
CCD	Charge-Coupled Device
CdTe	Cadmium telluridT
CMOS	Complementary Metal-Oxide-Semiconductor
c-Si	Crystalline Silicon
d	Duty cycle
DC	Direct Current
EL	Electroluminescence
FB	Forward-Bias
FFT	Fast Fourier Transform
fps	Frames per second
IBC	Interdigitated Back Contact
IGBT	Insulated Gate Bipolar Transistor
I_{MPP}	Maximum Power Point Current
InGaAs	Indium Gallium Arsenide
IPCC	Intergovernmental Panel on Climate Change
I_{SC}	Short Circuit Current
I-V	I (Current) - V (Voltage)
LC	L (Inductor) C (Capacitor)
LCOE	Levelized Cost of Energy
MLPE	Module-Level Power Electronics
MOSFET	Metal–Oxide–Semiconductor Field-Effect Transistor
MPP	Maximum Power Point
MPPT	Maximum Power Point Tracking
NIR	Near Infrared
OC	Open Circuit
P&O	Perturb and Observe
PCB	Printed Circuit Board
PID	Potential Induced Degradation
PL	Photoluminescence
PLC	Power Line Communication
PV	Photovoltaic
P-V	P (Power) - V (Voltage)
PWM	Pulse-Width Modulation
SC	Short Circuit
SNR	Signal-to-Noise Ratio
STC	Standard Test Conditions
SWIR	Short-Wave Infrared
UART	Universal Asynchronous Receiver/Transmitter
UAVs	Unmanned Aerial Vehicles
V_{MPP}	Maximum Power Point Voltage
V_{OC}	Open Circuit Voltage

Chapter I

Introduction

1.1. Framework

Global warming is arguably the most urgent environmental issue requiring immediate attention. It has already caused an increase of 1.47 °C in the average global temperature since pre-industrial times [1]. The Intergovernmental Panel on Climate Change (IPCC) indicates that limiting global warming to below a 1.5 °C increase could significantly reduce the impacts and consequences of climate change [2]. This objective is reflected in international cooperation through the Paris Agreement [3], a global accord signed by the European Union and 193 countries. The agreement establishes a set of policies aimed at limiting global warming to below 2 °C, with a preferred target of 1.5 °C.

Global warming is mainly driven by anthropogenic greenhouse gas emissions, which reached a new record of 36.3 Gt of CO_2-equivalent in 2024 [4]. Governments worldwide are incorporating strategies into their policies to limit carbon emissions and achieve a net-zero scenario by mid-century. Several sectors require profound transformations to reach this goal. One of the most critical is the power sector, which accounts for 38.7% of global emissions [4] and is currently undergoing a major transition, shifting from fossil fuels to renewable energy sources.

Meanwhile, electricity demand continues to increase each year, as shown in Figure 1, reaching 30,915 TWh of electricity generation in 2024 [5]. Currently, 41% of electricity generation comes from greenhouse gas emission-free sources, while 32% corresponds to renewable sources. Among these, hydropower leads with 14.2%, followed by wind and solar technologies, accounting for 8.1% and 6.9%, respectively. As illustrated in Figure 1, the latter two technologies have experienced a strong growth in recent years.

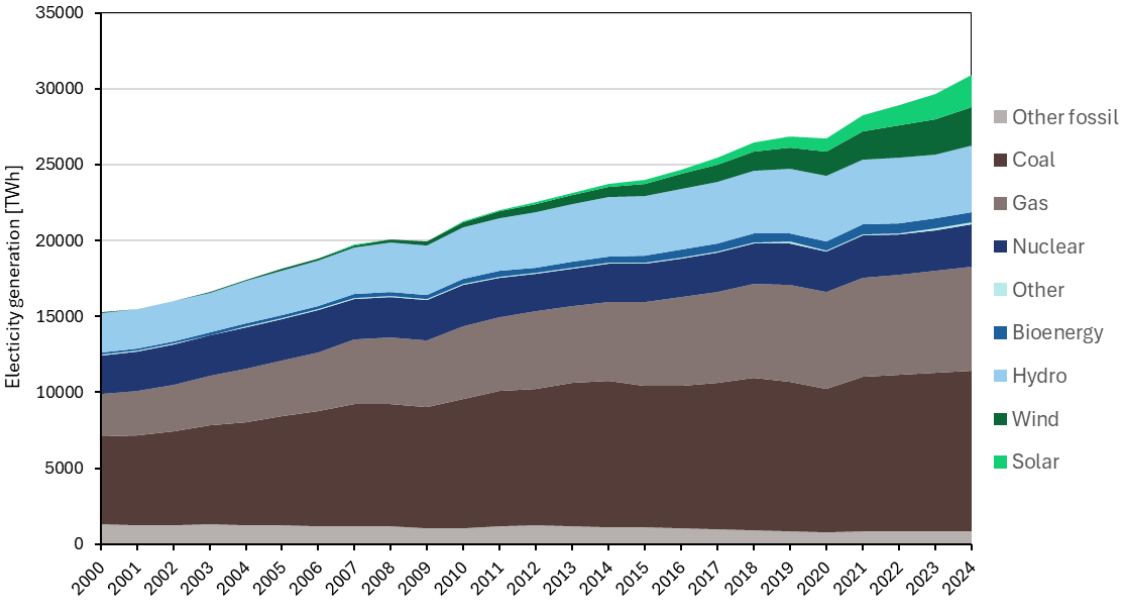

Figure 1. Evolution of electricity generation by source from 2000 to 2024. Data adapted from EMBER [5].

Photovoltaics (PV) is undergoing rapid growth in global capacity, which recently reached 2.2 TW_p in 2024 [6]. Additionally, forecasts indicate that PV will become the leading renewable energy technology by 2029 [7]. This growth is largely driven by the reduction in PV module manufacturing costs, which have plummeted from 2.0 USD/W_p in 2010 to less than 0.2 USD/W_p in 2020 [8]. As PV modules are the most expensive hardware component in utility-scale power plants, this cost reduction has allowed initial investment costs to fall from 5,283 USD/kW_p in 2010 to 691 USD/kW_p in 2024 [9].

In fact, electricity generated by photovoltaics is currently the most cost-effective form of power production, along with onshore wind energy, with a levelized cost of electricity (LCOE) of 43 and 34 USD/MWh, respectively, in 2024 [9]. This reduction in LCOE is also driven by the continuous improvement in solar cell technologies, with commercial silicon PV modules achieving an average absolute efficiency increase of 0.3–0.4% per year [10]. As a result, current commercial modules can reach efficiencies of up to 25% [10].

PV is not only deployed in utility-scale solar farms but also enables decentralized generation through self-consumption systems, with strong potential for rooftop installations in both urban and rural settings [11,12]. Furthermore, the modularity, scalability, and relatively short installation times of PV systems make them highly suitable for accelerating electrification in remote or off-grid areas, contributing directly to energy access and resilience [13]. Finally, PV also stands out for its low carbon footprint, estimated at 43 g of CO_2-equivalent per kWh [14], positioning this technology as a powerful tool for meeting global carbon emission reduction goals.

As installed PV capacity continues to grow, ensuring long-term performance and reliability becomes increasingly important, making advanced monitoring and inspection techniques a crucial part of PV operation and maintenance strategies [15–17]. PV modules are exposed to various environmental stressors such as soiling, humidity, ultraviolet radiation, hail, or extreme temperatures, among others [18]. These factors lead to degradation rates typically ranging from 0.5% to 0.8% per year [19–21]; and can also result in the development of faults such as microcracks, delamination, bypass diode failures, disconnections, potential-induced degradation (PID), and so forth [18,21,22].

These faults not only reduce the power output of the PV system but can also pose safety risks, including fire hazards [18]. Therefore, conducting periodic inspections of the PV field to analyse both degradation and emerging faults becomes essential for optimizing system performance. This includes inspections at various stages, from initial manufacturing to end-of-life operation [23], such as post-production testing, inspections after transportation, routine maintenance during regular operation, and assessments following extreme weather events like hailstorms or strong winds.

As utility-scale PV installations continue to grow with new systems commonly exceeding 100 MW_p [24] (around 200,000 modules), inspection and advance monitoring become increasingly challenging due to the vast number of modules that must be analysed. In this context, field inspection techniques need to be fast and cost-effective to be feasible as part of routine maintenance tasks [25]. Moreover, it is desirable for these inspection methods to be non-invasive, meaning they do not require electrical disconnection or system shutdown, and can therefore be performed during normal operation with null or minimal impact on energy generation.

In the context of advanced monitoring of PV systems, monitoring the electrical parameters of these systems can aid in the detection of faults within the plants. Both statistical methods [26] and artificial intelligence-based approaches [27–30] can be used to automatically detect faults in PV plants by analysing the power output of the PV array along with environmental parameters. Beyond advanced monitoring, whose effectiveness depends on the level at which the plant is monitored (array, string, or module), inspection techniques such as I–V curve tracing, thermography, and electroluminescence imaging enable a more detailed analysis of the performance of each module.

Firstly, the measurement of the electrical characteristic curve of PV modules, known as the current-voltage (I-V) curve, is quite common. I-V curve tracing is considered a valuable tool for analysing the electrical behaviour of a module, including its power output and other electrical parameters [21]. However, its main drawback is that it requires the disconnection of the module to connect it to the testing device, making it an invasive technique with low throughput.

On the other hand, infrared thermography is a non-invasive and contactless imaging technique that can be performed during the normal operation of the PV system [31,32]. Thermal images reveal the temperature distribution of the module, enabling the detection of thermal patterns that indicate the presence of faults. Moreover, the integration of infrared thermal cameras into unmanned aerial vehicles (UAVs) has led to a fast and cost-effective technique suitable for inspecting large numbers of PV modules [32–35]. Nevertheless, the main drawbacks of infrared thermography are the need for a threshold irradiation level so that defects generate thermal gradients revealing faults, and the low spatial resolution due to heat distribution across the solar cells, which hinders the detection of minor defects.

Luminescence, which includes both electroluminescence (EL) and photoluminescence (PL), is another imaging technique, based on capturing the electromagnetic emission generated by the solar cells [36,37]. These images reveal the internal structure of the cells, enabling the detection of a wider range of faults compared to previous techniques as well as a better understanding of the optical and electrical performance of the PV solar cells [38]. While EL and PL imaging are standard and widely used techniques in laboratories and manufacturing facilities worldwide, their application in field inspections is limited by certain technical constraints, including their invasive nature and the need for an external energy source to generate the luminescent signal [36,37,39].

In this context, the exploration of novel methods and techniques that overcome the main limitations of conventional luminescence imaging has gained increasing interest within the scientific community. In the present thesis, a novel non-invasive luminescence imaging method, encompassing both EL and PL, is investigated.

1.2. Objectives

The **main objective** of the present thesis is to develop and validate a non-invasive technique for EL and PL imaging, based on an electronic device integrated at the module-level that does not require external energy sources.

This main objective can be broken down into the following **specific objectives**:

1. Analyse the limitations of conventional EL and PL techniques, as well as review different and novel methods proposed by the scientific community. This objective is addressed in Chapter III (State of the Art).
2. Design and validate an embedded electronic architecture that enables EL modulation using the current generated by the PV string and PL modulation using sunlight as the excitation source. This objective is addressed in Chapter IV (Design of Module-level Electronics for Non-Invasive Luminescence Signal Modulation).
3. Develop and validate image processing approaches capable of extracting the luminescence signal from background noise generated by sunlight. This objective is addressed in Chapter V (Luminescence Imaging Acquisition Processing).
4. Integrate the proposed non-invasive luminescence technique into module-level solar optimizer topologies, along with non-invasive I-V curve tracing. This objective is addressed in Chapter VI (Integration of Non-Invasive PL and I-V tracing Functionalities into a Module-Level PV Optimizer).

Chapter II

Theoretical and Technical Framework

This chapter provides the theoretical framework and technical background necessary to understand the developments and research presented in the subsequent chapters. First, the concept of the I–V curve is introduced to describe the electrical behaviour of a PV module. Second, the nature of the luminescence signal is discussed, including its generation mechanisms and the sensors used for its detection. Third, the lock-in detection technique is explained, which enables the measurement of weak signals superimposed on stronger ones. In the context of this thesis, the lock-in technique allows the extraction of the luminescence signal from the background signal generated by sunlight, which is significantly more intense. Finally, since the thesis involves the development of a module-level solar optimizer, the concept of maximum power point tracking (MPPT) is addressed, with a particular focus on the buck converter topology, which has been selected to integrate both I–V curve tracing and luminescence measurement functionalities.

2.1. I-V Curve

The electrical performance of a PV module is characterized by its I–V curve, which describes the relationship between the output current and voltage of the module under specific operating conditions [21,40]. This curve defines all the possible operating points of the module, ranging from short-circuit conditions (maximum current and zero voltage) to open-circuit conditions (zero current and maximum voltage). A typical illuminated I–V curve for a PV module is shown in Figure 2, indicating the short-circuit current (I_{SC}) and the open-circuit voltage (V_{OC}).

Since the output power of the module is the product of current and voltage, a power–voltage (P–V) curve can also be defined. In this curve, no power is delivered under open-circuit (OC) or short-circuit (SC) conditions. The curve exhibits a clear maximum corresponding to the point where the power output is highest. This point is known as the maximum power point (MPP), and it is defined by current (I_{MPP}) and voltage (V_{MPP}) at which it occurs.

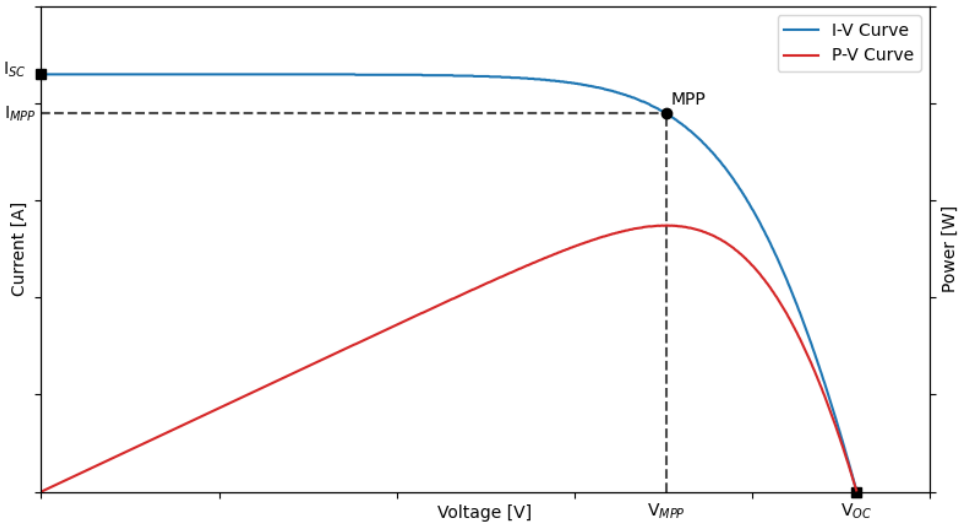

Figure 2. Typical illuminated current–voltage (I–V) and power–voltage (P–V) curves of a PV module.

As previously explained, measuring the I–V curve is essential for obtaining quantitative information about the electrical behaviour of a PV module. Comparing the measured I–V curve with previous measurements or with the manufacturer's specifications is a valuable tool for monitoring degradation and detecting faults [15,21].

The I–V curve has a dynamic nature, showing significant variations depending on the module's operating conditions [41]. The two main parameters that influence the shape of the I–V curve are irradiance and temperature. Figure 3 shows a set of I–V curves under different irradiance and temperature conditions.

Irradiance has a direct impact on I_{SC}, which is approximately proportional to the irradiance level. It also affects V_{OC}, although to a lesser extent; a slight decrease in V_{OC} is typically observed as irradiance decreases. Temperature also affects the shape of the I–V curve. While I_{SC} increases slightly with temperature, typically by about +0.05 %/°C in commercial silicon modules, the effect on V_{OC} is much more significant. V_{OC} decreases with increasing temperature at an average rate of approximately –0.3 %/°C to –0.4 %/°C in commercial silicon modules.

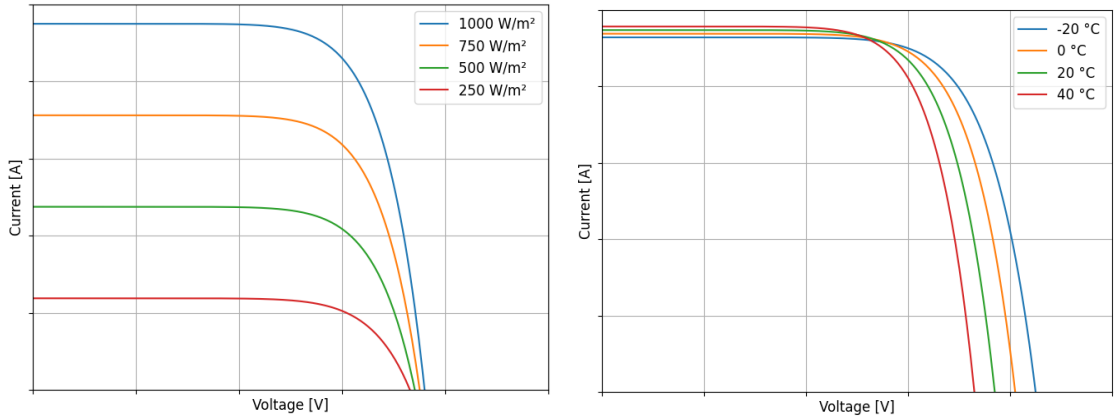

Figure 3. Set of I–V curves under different irradiance values at the same temperature (a) and set of I–V curves under different temperature values at the same irradiance (b).

2.2. Luminescence Signal Nature and Acquisition

Luminescence imaging for photovoltaic applications, which is based on the use of camera sensors, requires an appropriate excitation source, which leads to two different signal generation mechanisms and, consequently, two types of images [42,43]. The first mechanism, electroluminescence (EL), involves electrical excitation, where a forward-bias (FB) current is injected into the photovoltaic device. The second mechanism, photoluminescence (PL), relies on optical excitation, in which the device is illuminated with suitable light. Although both EL and PL imaging provide similar information, EL images primarily reveal the electrical behaviour of the solar cells, whereas PL images are more indicative of the quality of the cell structures [39,44].

As illustrated in Figure 4, the EL signal can be approximated as having a linear dependence on the forward-bias current, while the PL signal depends exponentially on the operating voltage of the PV device, reaching its maximum at V_{OC}. Moreover, the PL signal also exhibits a linear dependence on irradiance [45]. It should be noted that under dark conditions, any applied voltage to the photovoltaic device generates a forward-bias current and, consequently, EL signal. When a forward-bias current is injected, the device operates

in the fourth quadrant as a load, and EL and PL emissions are superimposed if the PV module is under illumination.

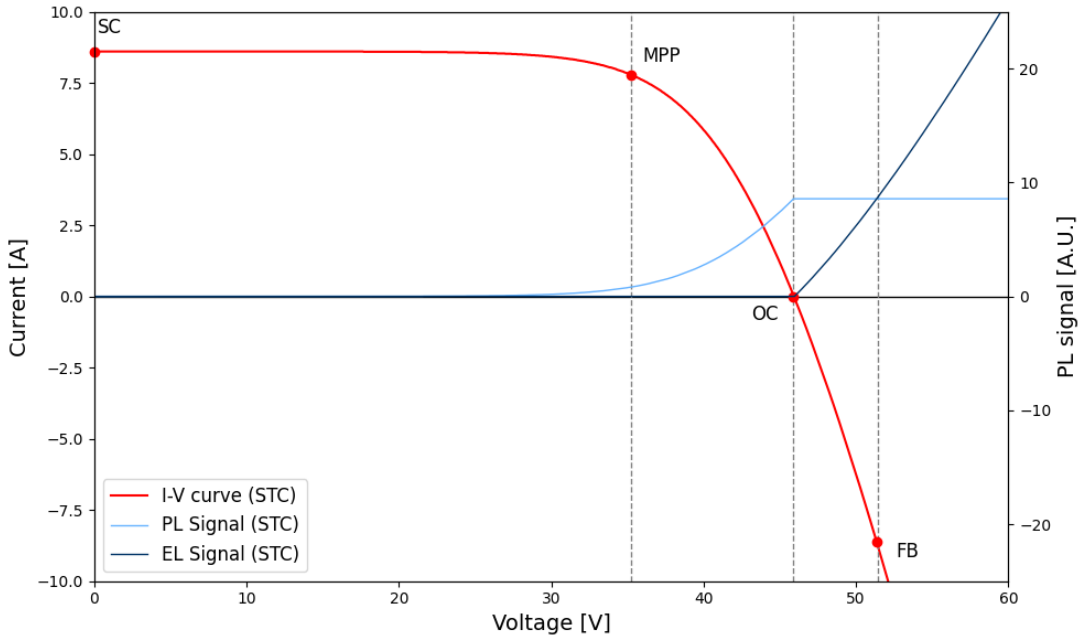

Figure 4. Typical illuminated I–V curve of a PV module under standard test conditions (STC), showing its behaviour in the first and fourth quadrants, along with PL and EL emissions as functions of the module operating voltage. Data obtained from LTspice simulations.

For proper luminescence signal capture, it is essential to know its emission spectrum, which can vary significantly depending on the semiconductor material that makes up the solar cells [37]. Figure 5 shows the normalized emission spectra of different materials used in PV solar cell applications. For the purposes of this thesis, the focus will be on luminescence emission in crystalline silicon (c-Si) cells, as this technology represents approximately 95% of the commercial module volume in the market [46], followed by Cadmium Telluride (CdTe) and amorphous silicon (a-Si). Crystalline silicon PV modules exhibit a luminescence emission peak around 1,150 nm, outside the visible range and within the near-infrared (NIR) region, also known as short-wave infrared (SWIR).

Figure 5 also includes a reference solar spectrum [47]. Between 1,100 nm and 1,200 nm, the solar irradiance drops due to one of the H_2O absorption bands, which coincides with the luminescence spectrum for crystalline silicon.

Considering that the luminescence signal peaks around 1,150 nm, two types of commercial sensors can be used for its acquisition [48]. First, both charge-coupled device (CCD) and complementary metal-oxide-semiconductor (CMOS) silicon-based sensors are commonly used for this purpose. As shown in Figure 5, silicon-based sensors have high efficiency within the visible range but exhibit very low quantum efficiency in the NIR region corresponding to the luminescence signal. This limitation necessitates a completely dark environment and long exposure times to capture the signal effectively.

On the other hand, InGaAs (Indium Gallium Arsenide) based sensors exhibit high quantum efficiency within the NIR region, making them ideal for capturing this signal. However, InGaAs sensors tend to have lower resolution and higher costs compared to silicon sensors. The main features of both silicon and InGaAs cameras are summarized in Table 1.

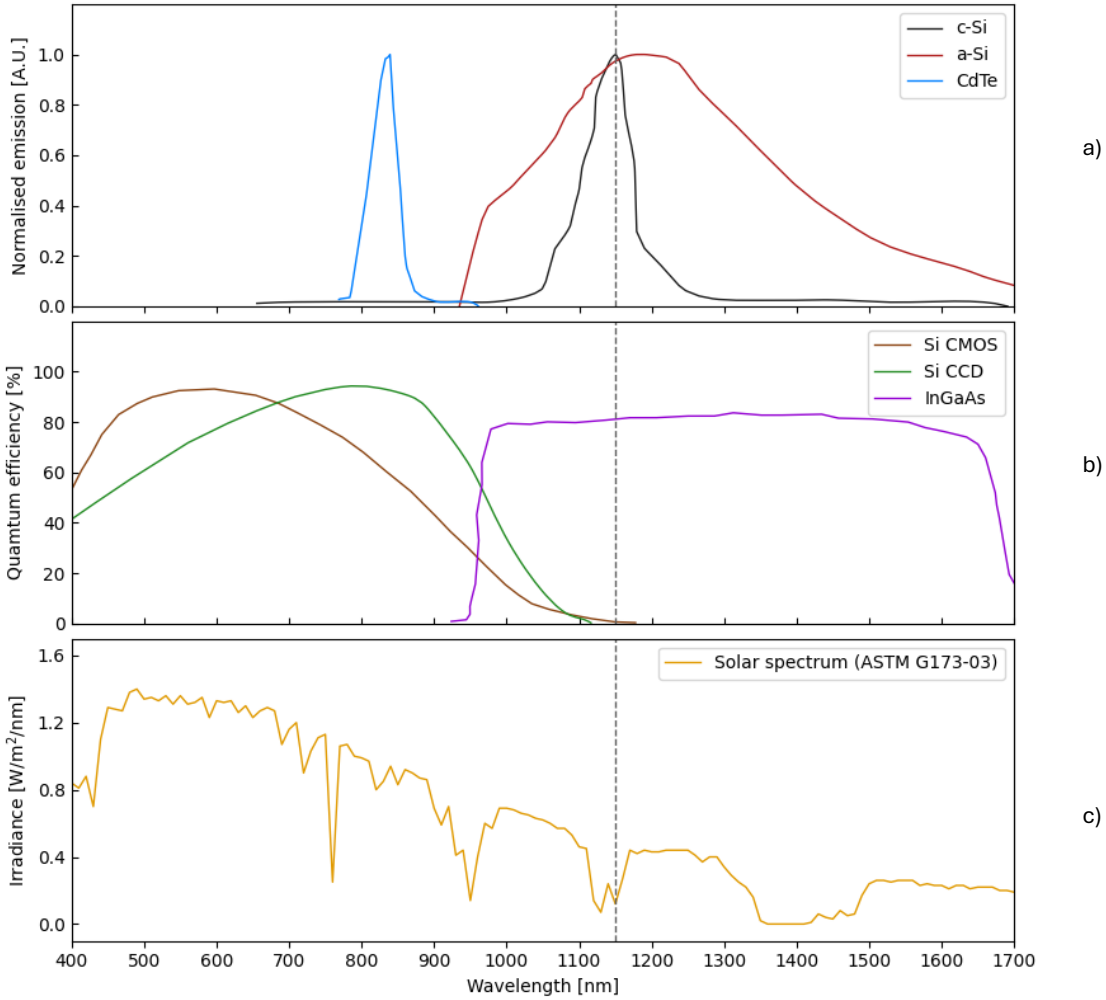

Figure 5. Normalized luminescence emission of different solar cells (a) [32], quantum efficiency of the sensor used (b) [32], and ASTM G173-03 reference solar spectrum (c) [47].

Note that recent developments in germanium-based SWIR imaging array sensors represent a promising technology [49]. Although no commercial cameras are currently available, their simpler fabrication process compared to InGaAs detectors could lead to cameras up to 20 times cheaper, which are likely to be introduced to the market soon [50].

Table 1. Main features of sensors used for luminescence applications: silicon and InGaAs sensors.

	Silicon sensors	**InGaAs sensors**
Quantum efficiency (1,150 nm)	≈ 1%	> 60%
Sunlight sensitivity	High sensitivity	Medium sensitivity
Exposure time	Long exposure time	High exposure time
Resolution	High resolution	Low resolution
Price	Low	High
Applications	Dark measurements	Dark/Daylight measurements

Another important aspect of luminescence emission is the signal intensity, which determines the conditions required for its acquisition, especially under daylight. Within crystalline silicon PV modules, various cell technologies exist. Although all crystalline silicon technologies share an emission peak at around 1,150 nm and similar normalized emission spectra, there are significant differences in signal intensity [51], as shown in Figure 6.

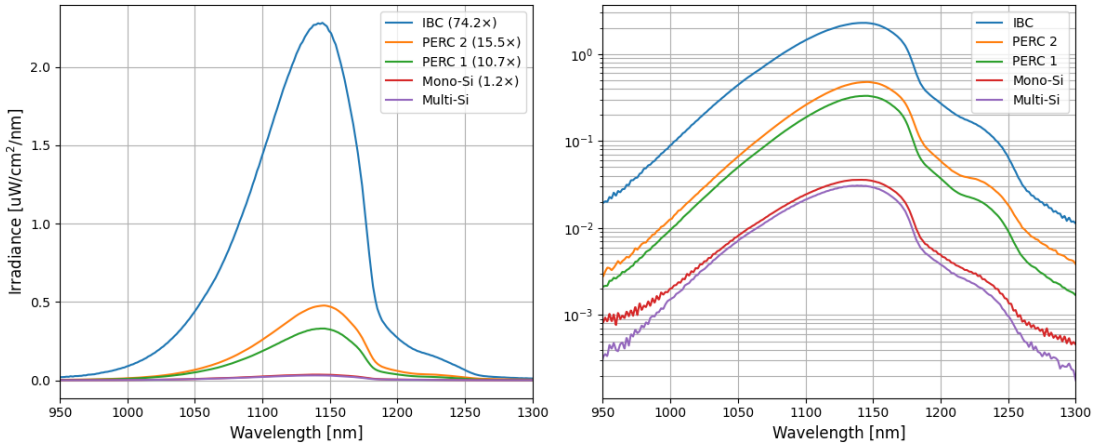

a) b)

Figure 6. Spectrum of different crystalline silicon PV modules technologies in linear scale (a) and logarithmic scale (b). Signal capture under I_{SC} forward-bias current. Data adapted from [51].

Traditionally, multicrystalline and monocrystalline silicon PV modules have dominated the market [52]. These base technologies exhibit very weak luminescence emission, with monocrystalline cells showing luminescence signal intensities approximately 20% higher than those of multicrystalline ones. In recent years, improved cell architectures such as passivated emitter and rear cell (PERC) designs have been introduced [53]. PERC cells incorporate a rear-side passivation layer that enhances carrier recombination properties and can be implemented on both monocrystalline and multicrystalline wafers. This modification results in luminescence signal intensities approximately one order of magnitude higher than those of conventional monocrystalline and multicrystalline cells, corresponding to increases ranging from 970% to 1,450% compared to standard multicrystalline and monocrystalline cells. Finally, interdigitated back contact (IBC) architectures, currently used mainly in high-end commercial PV modules, also rely on monocrystalline or multicrystalline silicon substrates [52]. Due to their advanced contact and passivation configuration, IBC cells exhibit even stronger luminescence emission, reaching signal intensities up to two orders of magnitude higher (around 7,320% greater) than those of conventional multicrystalline and monocrystalline technologies.

Figure 6 also illustrates how weak the luminescence signal is compared to sunlight, which can reach irradiance levels exceeding 1,000 W/m^2. The integration of the spectra presented in Figure 6 allows for the calculation of the total irradiance generated by each technology, which corresponds to 0.0315 W/m^2 for monocrystalline, 0.0375 W/m^2 for polycrystalline, 0.3025–0.4378 W/m^2 for PERC, and 2.2381 W/m^2 for IBC. This large difference represents one of the main challenges when performing EL and PL imaging under daylight conditions.

To improve the ratio between the luminescence signal and the sunlight background during daylight measurements, optical filters can be used to selectively reduce the amount of sunlight captured by the camera. Two types of filters can be implemented [54]:

- Long-pass filter: A filter that blocks light with wavelengths shorter than a certain cutoff value, allowing only longer wavelengths to pass through.
- Band-pass filter: A filter that allows light within a specific range of wavelengths to pass through, while blocking both shorter and longer wavelengths outside that range.

In the context of luminescence measurements under daylight conditions, the use of filters is essential to obtain a sufficiently high luminescence signal and to produce images with adequate quality, especially in monocrystalline and multicrystalline modules, where luminescence intensity is particularly low.

2.3. Lock-in Detection Technique in Luminescence Imaging

As previously explained, the luminescence signal is much weaker than the background signal generated by sunlight. As a result, the signal to be imaged is of the same order of magnitude as the noise present in the measurement. In this context, lock-in detection is a signal processing technique specifically designed to extract weak signals buried in noise. By applying periodic modulation to the signal, it becomes possible to isolate it from the background, effectively eliminating the influence of noise.

Lock-in approaches for EL and PL imaging under high irradiance conditions are based on capturing pairs of measurements in which the luminescence signal is alternately high and null or low. By subtracting these two measurements, it is possible to extract the luminescence signal. However, since the noise level is comparable to the signal itself, it is necessary to repeat this process multiple times in order to statistically minimize the effect of noise. Increasing the number of measurement pairs improves the signal-to-noise ratio (SNR) by reducing the impact of random noise.

To illustrate this technique, an example is shown in Figure 7. It includes a total of 20 measurements acquired by alternating between high and null luminescence values. Measurements with odd indices capture only the background signal, while those with even indices include both the background and the luminescence signal.

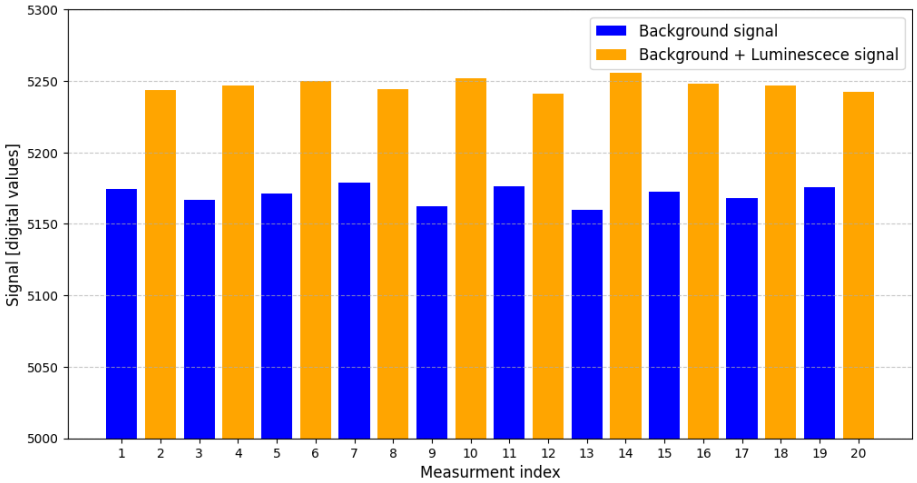

Figure 7. Example of signal evolution in a sequence of luminescence images using the lock-in technique.

The calculation of the luminescence signal after background subtraction ($Signal_{EL/PL}$) can be performed using Equation (1), where N is the total number of measurements, M_i represents the measurements at even indices (where the luminescence signal is present), and M_j represents the measurements at odd indices (where the luminescence signal is absent). Since the measurement is based on images, this process must be performed individually for each pixel across the entire image sequence.

$$Signal_{EL/PL} = \frac{2}{N}\sum_{i\in \text{even}} M_i - \frac{2}{N}\sum_{j\in \text{odd}} M_j \quad (1)$$

It is also important to note that the background signal generated by sunlight continuously changes, as irradiance varies over time. Therefore, it is desirable to acquire the image sequence as quickly as possible. Moreover, the fact that the measurements alternate between high and null luminescence signals helps minimize the effect of changing irradiance.

2.4. Maximum Power Point Tracking

It has been explained that a PV module can operate in any of the points that make up its I-V curve, with a single point, known as the MPP, where the power output is maximum. The working point of the PV module is determined by the load connected to it. Figure 8 includes a typical I-V curve of one solar module and several lines corresponding to different loads. These lines are defined as lines with a slope equivalent to the inverse of the load impedance; and its intersection with the I–V curve determines the working point.

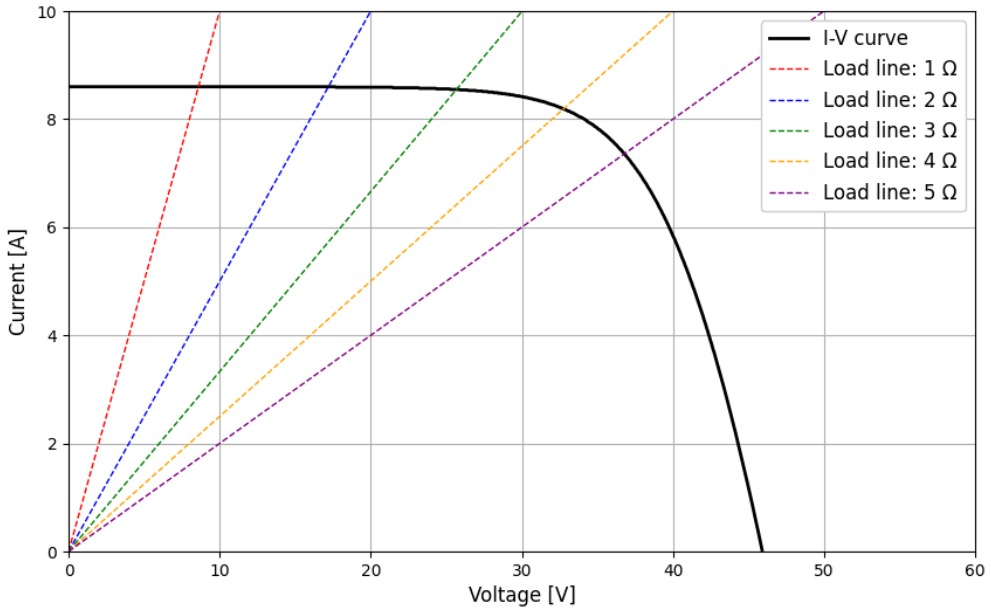

Figure 8. Typical I–V curve of a PV module and load lines defined by the inverse of the load impedance. The working point of the PV module is determined by the intersection of the load line and the I–V curve.

This, combined with the fact that the I–V curve varies with environmental parameters such as temperature and irradiance, has led to the need for power electronic converters capable of varying their input impedance with a constant load at the output, thus enabling the implementation of a maximum power point tracking (MPPT) algorithm. [55,56]. This task can be performed in different hierarchical levels:

- PV array-level MPPT: a single converter performs MPPT for an entire PV array composed of several strings connected in parallel, where each string consists of approximately 20–30 modules in series. This centralized strategy allows one converter to manage more than 2,000 modules, with a total nominal power exceeding 1 MW_p. The converter is typically integrated into a central PV inverter, making this approach the most used in utility-scale PV power plants.
- PV string-level MPPT: a single converter performs MPPT on a single PV string, which typically consists of 10–30 modules connected in series. These converters generally have nominal power ratings between 2 to 20 kW_p and are typically integrated into string inverters. Although this strategy is less common in utility-scale PV plants, it is widely adopted in small-scale residential and industrial PV systems.
- PV module-level MPPT: a single converter performs MPPT on an individual PV module, typically handling power between 300 and 800 W_p. This approach is increasingly being adopted in the residential sector and is usually implemented through two types of converters: module-level PV optimizers and PV microinverters [57].

From an economic perspective, centralized MPPT strategies based on central inverters offer a lower initial investment cost [58]. However, this approach can only optimize the aggregated I–V curve of the entire PV array. As a result, individual modules will operate at their respective MPP only if their I–V characteristics are identical. In practice, even when using modules of the same model, variations in I–V behaviour may arise due to factors such as manufacturing tolerances, partial shading, uneven soiling, non-uniform aging, or the presence of faults. These inconsistencies lead to mismatch losses, which ultimately reduce the total power output of the PV plant [59,60].

2.5. Buck Converter Topology

There are several power electronics topologies that can be used to develop converters capable of tracking MPP. Below, the buck converter topology is described, as it has been selected for the development of a module-level PV optimizer that integrates I–V tracing and luminescence functionalities.

Figure 9 shows the topology of a buck converter, which consists of a switching element (SW), a diode (D), and a low-pass filter composed of an inductor (L) and a capacitor (C). For further analysis, the converter is powered by a voltage source at the input and supplies a load at the output.

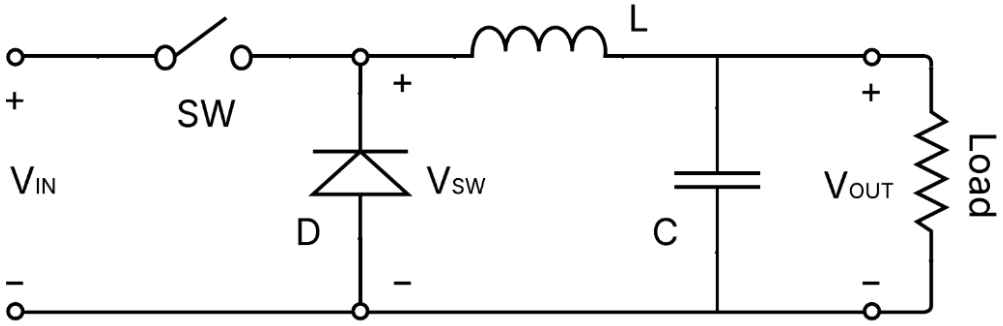

Figure 9. Power topology of a step-down (buck) converter.

The switching element, typically a MOSFET (Metal–Oxide–Semiconductor Field-Effect Transistor) or IGBT (Insulated Gate Bipolar Transistor), is controlled by a periodic logic signal known as a pulse-width modulation (PWM) signal. This periodic signal has a fixed frequency but can vary its duty cycle, which is the ratio between the time the switch is on (t_{ON}) and the total switching period ($t_{ON} + t_{OFF}$). Therefore, the duty cycle (d) is defined by Equation (2).

$$d = \frac{t_{ON}}{t_{OFF} + t_{ON}} \tag{2}$$

Figure 10 shows the main waveforms of a buck converter. On the one hand, when the switch is on, the voltage at the switching node (V_{SW}) equals the input voltage (V_{IN}). On the other hand, when the switch is off, V_{SW} drops to zero. Since the ratio between t_{ON} and total period can be adjusted through the duty cycle, it is possible to generate a controlled square-wave voltage at the switching node. Additionally, implementing a low-pass LC filter composed of an inductor and a capacitor allows the voltage and current seen by the load to be averaged.

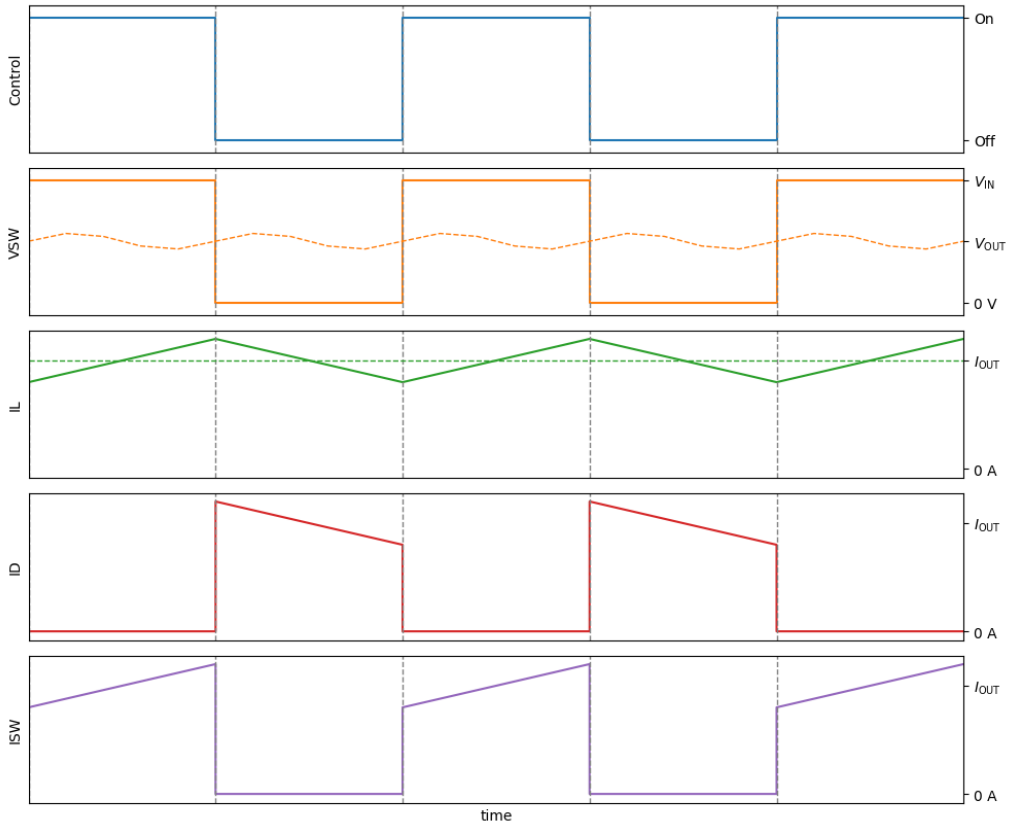

Figure 10. Typical waveforms of buck converter: control signal of the switch element, voltage at switching node (V_{SW}), inductor current (I_L), diode current (I_D), and switch current (I_{SW}).

An LC low-pass filter is characterized by its cutoff frequency (fc) defined as the frequency at which the filter begins to attenuate the input signal. In such a filter, the cutoff frequency marks the boundary between the frequency range that is transmitted with minimal attenuation and the range that is progressively suppressed. The cutoff frequency depends on the values of the inductor (L) and the capacitor (C); and is given by Equation (3). Therefore, the LC low-pass filter must have a cutoff frequency lower than the switching frequency of the control signal. This also implies that increasing the switching frequency allows for a reduction in the size of the filter components.

$$f_c = \frac{1}{2\pi\sqrt{LC}} \tag{3}$$

During the time the switch is on, current flows through the inductor, linearly increasing as the inductor stores energy. During the off time, current flows through the diode, and the inductor discharges. This inductor ripple (ΔI_L) is defined by Equation (4), where d is the duty cycle and f is the switching frequency. The output voltage ripple (ΔV_{OUT}) can also be calculated using Equation (5).

$$\Delta I_L = \frac{V_{OUT} \cdot (1 - d)}{L \cdot f} \tag{4}$$

$$\Delta V_{OUT} = \frac{\Delta I_L}{8 \cdot L \cdot C} \tag{5}$$

The buck converter only allows voltage reduction, with the output voltage defined by Equation (6). Since the duty cycle is limited to values between 0 and 1, it is not possible to increase V_{OUT} above V_{IN}.

$$V_{OUT} = V_{IN} \cdot d \tag{6}$$

In practical terms, the presented topology is completed with an input capacitor (C_{IN}) to filter the input current. Moreover, it is possible to replace the diode in the buck converter with another switching element, known as a synchronous switch, resulting in the synchronous buck topology. When current flows through the diode, a voltage drop occurs across it, leading to power losses. Replacing the diode with a controlled switch reduces this voltage drop to nearly zero, thereby increasing the overall efficiency. The main switch and the synchronous switch operate in a complementary manner, meaning that when one is on, the other is off. This complementary operation is crucial to prevent both switches from conducting simultaneously, which would cause a shoot-through condition. Such a condition can result in converter malfunction, reduced efficiency, and potential damage to the hardware.

The topology of the synchronous buck converter is shown in Figure 11. In this configuration, both switches form a half-bridge, and can therefore be referred to as the high-side switch (H-SW) and the low-side switch (L-SW).

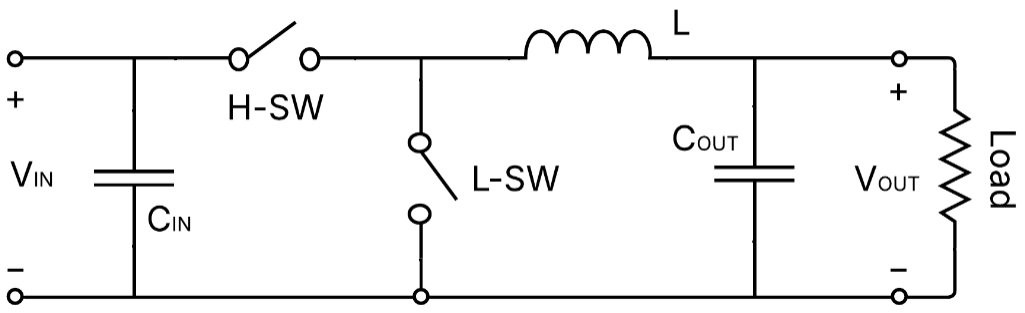

Figure 11. Synchronous buck converter power topology.

Chapter III

State of the Art

As the main objective of the present thesis is to design a non-invasive technique for EL and PL imaging based on a module-level electronic system, a detailed review of different methods for obtaining EL and PL measurements in field-deployed modules is presented. The techniques have been classified into two groups: those that require acquisition under dark conditions and those that are suitable for environments with daylight. A general overview of the identified techniques is shown in Figure 12.

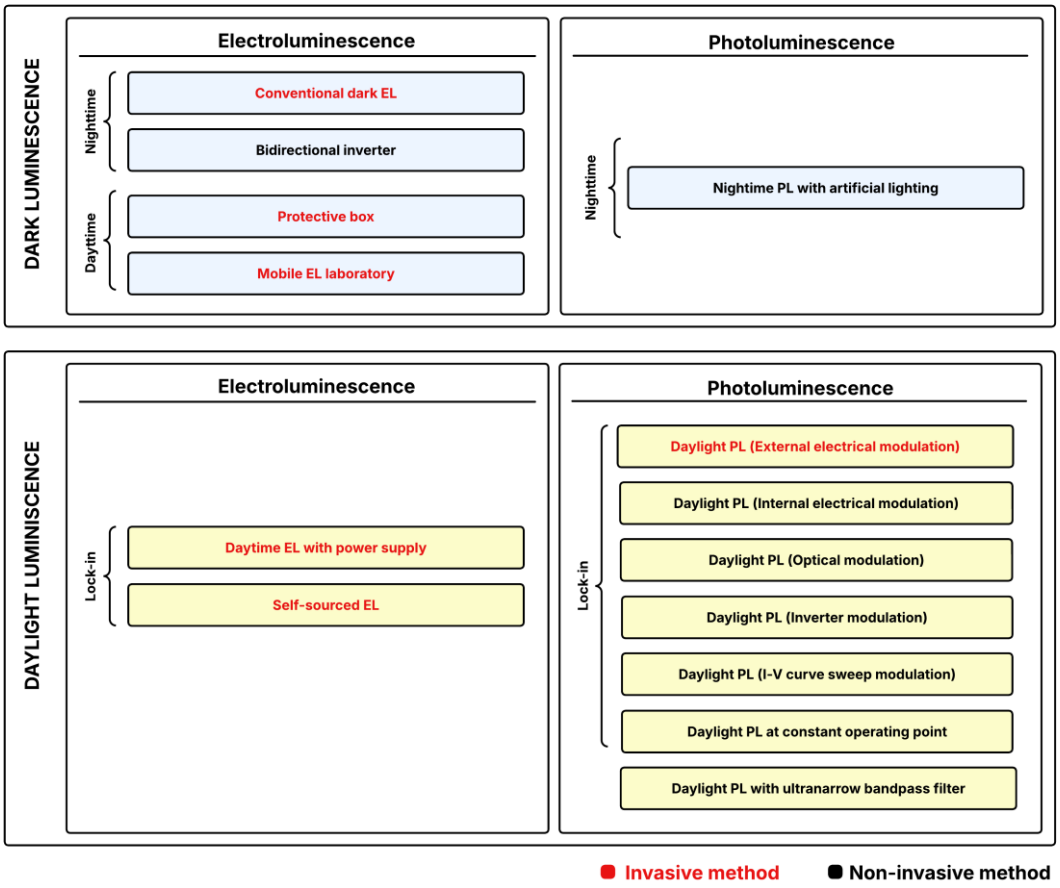

Figure 12. Overview of EL and PL imaging techniques for field-deployed PV module inspections.

Figure 12 also presents a distinction between EL and PL techniques. EL imaging is most performed under dark condition, PL approaches are more frequently used in daylight environments, as PL can utilize sunlight as an excitation source, an advantage in outdoor measurements. It is worth noting that some EL methods designed for dark conditions can also be implemented during daytime, by creating an artificial dark environment. In daylight luminescence imaging, both EL and PL approaches typically rely on image sequence acquisition combined with lock-in detection techniques, apart from one novel method that enables PL imaging with a single camera shot, which will be discussed later.

After presenting all EL and PL approaches, the integration of UAVs into luminescence imaging will be briefly addressed. Finally, a summary and general conclusion of luminescence techniques applied to field-deployed modules will be provided.

3.1. Luminescence Techniques under Dark Conditions

As explained in Chapter II, the luminescence signal intensity is significantly lower than the solar irradiance. Therefore, performing luminescence measurements under dark conditions is simpler and more effective. Such conditions allow the acquisition of EL or PL images with a single camera shot, enabling high-speed and straightforward image capture. Additionally, dark conditions allow the use of inexpensive silicon-based cameras. Below, luminescence techniques that require a dark environment are discussed. Four of them correspond to EL imaging, while one is based on PL imaging.

Conventional Dark Electroluminescence

Traditionally, EL images in PV power plants have been taken during nighttime using a power supply as the excitation source [21]. Nighttime EL imaging has been preferred since it is more practical to use a power supply than a uniform lighting device for PL emission. Moreover, this light can introduce noise in the final image.

IEC 60904-13 [61] includes requirements for acquisition, analyse and interpretation of EL images in PV modules. It is recommended to perform measurements under a forward-bias current corresponding to I_{SC}. Therefore, it is needed to use a power supply that can manage I_{SC} of the PV module, and a voltage a bit higher than V_{OC} of the module. Note that it is feasible to induce EL signal in one PV string or array if the power supply can handle with I_{SC} and V_{OC} of the total system.

In EL imaging, it is possible to use a metric to quantitatively analyse image quality in dark environments. This metric is known as signal to noise ratio (*SNR*) and its calculation is shown in Equation (7) [62].

$$SNR = \frac{\sum_k \left(0.5 \cdot \left(EL_1(k) + EL_2(k)\right) - BG(k)\right)}{\sum_k \left(|EL_1(k) - EL_2(k)| \cdot \sqrt{0.5} \cdot \left(\frac{2}{\pi}\right)^{-0.5}\right)} \tag{7}$$

Where *k* denotes the pixel index, EL_1 and EL_2 correspond to two images acquired under forward-bias current, and *BG* is an image captured with the panel unpowered. A higher value than SNR of 5 is considered as a good quality EL image [62]. It is recommended to calculate the SNR after cropping the module surface, since pixels corresponding to areas outside the module can contribute to lowering the overall SNR.

The limitations of this technique regarding its implementation as a mainstream method in utility-scale PV power plants can be summarized in three main aspects. First, nighttime acquisition is undesirable due to potential adverse weather conditions, safety concerns, and the need to transport lighting equipment. Second, the use of a power supply is inconvenient, as it requires a battery system or generator to operate. Finally, module disconnections are necessary to connect the PV module or string to the power supply. All these factors contribute to conventional nighttime EL imaging being a low-speed and low-throughput technique that does not meet the requirements for inspecting the thousands of modules in utility-scale PV power plants.

Bidirectional Inverter

Bidirectional inverters offer a potential solution for enabling EL signal generation in PV modules PV inverters are power electronic devices that convert the direct current (DC) generated by a PV system into alternating current (AC) with frequency, amplitude, and phase matched to the grid, thereby allowing grid-connected operation. Conventional PV inverters do not permit bidirectional current flow due to their internal topologies. However, it is possible to design and operate bidirectional inverters capable of injecting forward-bias current into the PV array, thus enabling EL imaging without requiring module disconnection [63]. So far, this concept has been experimentally validated only at night, but in theory, it could also enable EL imaging during daylight.

While EL acquisition without the need for a power supply or module disconnection represents a significant advantage over conventional dark EL imaging, the higher investment cost associated with bidirectional inverters, along with the requirement for multiple breakers in the PV array to selectively energize specific sections of the PV plant, are the main limitations of this approach.

It is important to highlight that PV power plants hybridized with battery storage systems require bidirectional power flow between the power plant and the grid [64], which may facilitate the integration of bidirectional inverters and, consequently, the implementation of the present technique. Additionally, although less critical, bidirectional inverters can also be used to intentionally heat the PV modules, enabling active thermographic inspections [31] and snow melting [65]. This contributes to increased energy output and reduced risk of mechanical damage caused by snow accumulation.

Protective Box

As nighttime measurements are not desirable, it is possible to create an artificial dark environment to enable EL acquisition during daytime. These approaches rely on opaque enclosures or tents made of light-blocking materials that allow dark conditions to be achieved [37], with the EL signal generated using a power supply.

Although this setup facilitates daytime EL imaging, module disconnection is still required, and transporting and deploying tents or shielding structures introduces logistical complexity that reduces measurement throughput.

Mobile Electroluminescence Laboratory

Another approach that enables EL measurements during daytime under artificial dark conditions is the use of a PV mobile laboratory. This laboratory typically consists of a truck or van in which PV modules are disconnected and disassembled to carry out various tests, including EL imaging, I–V curve tracing, electrical insulation testing, and infrared thermography [66,67].

This method allows comprehensive characterization of PV modules with high-quality standards without the need to transport the modules outside the PV plant, saving time and minimizing the risk of damage. However, it still requires both disconnection and disassembly of the modules, which can be time-consuming and labour-intensive.

Nighttime Photoluminescence with Artificial Lighting

Although less common than nighttime EL measurements, PL imaging can also be performed at night [68,69]. In this case, a power supply is not required as excitation source. Instead, a lighting device is used to induce the PL effect while the module operates under OC conditions. The use of an artificial lighting system allows the light spectrum to be tailored to match the quantum efficiency of the solar cell material, thereby enhancing PL signal generation. Moreover, it also enables the selection of wavelengths that are outside the sensor's detection range, which can introduce noise into the final PL image.

In comparison with nighttime EL imaging using a power supply, PL imaging offers the advantage of not requiring module disconnection, thereby increasing measurement speed. Nevertheless, the lighting system must be transported throughout the PV plant, along with its power supply and battery, which adds logistical complexity. Additionally, it is desirable to use a homogeneous lighting source that provides a constant light intensity over the plane of the PV module, whose design and implementation can be technically challenging.

3.2. Luminescence Techniques under Daylight Conditions

Luminescence imaging in PV power plants can also be performed under daylight conditions. Since the intensity of the luminescence signal is significantly lower than that of sunlight, a lock-in detection technique must be applied to suppress the background signal generated by solar irradiance (see Chapter II). The implementation of this technique requires modulation of the luminescence signal, along with the acquisition of a sequence of images for subsequent processing and background subtraction. It is important to note that luminescence imaging under high irradiance conditions requires the use of InGaAs cameras and optical filters to enhance the ratio between the luminescence signal and the background signal caused by sunlight.

It is worth noting that daylight acquisition enables the use of sunlight as the excitation source for PL emission, eliminating the need for an external power supply or artificial lighting system for luminescence imaging. All daylight techniques discussed below are based on the lock-in principle, differing primarily in how the EL or PL signal is modulated. An exception is the final technique presented, which does not require signal modulation and thus only requires a single image for analysis.

Daytime Electroluminescence with Power Supply

EL signal modulation can be achieved using controlled power supplies that alternate between forward-bias current and OC conditions in the PV module under test [70–72]. Depending on the maximum voltage, current, and power ratings of the power supply, it is possible to modulate an entire PV string or even a full array simultaneously. This approach can be advantageous, as a single disconnection and cable reconfiguration may be sufficient to measure multiple PV modules, thereby increasing measurement speed and efficiency.

It is worth noting that the DaySy system [73] has emerged as a commercial solution. This system is based on an electronic box that can be powered by one or several PV strings and enables EL modulation in another PV string. Additionally, the electronic box can short-circuit the PV string, making PL signal modulation possible as well. However, this approach remains an invasive method, as disconnections are still required.

Self-Sourced Electroluminescence

Another technique that enables EL signal modulation is based on an electronic device connected directly to the module [74]. It incorporates a boost converter stage and several switches that charge a capacitor to a voltage higher than the module's V_{OC}, which is then discharged into the module to induce a forward-bias current. This configuration allows the periodic modulation of the EL signal required for lock-in detection.

The method stands out for its ability to generate the EL signal without the need for a power supply, as it uses the energy generated by the module itself to induce the EL effect. In contrast, the technique is limited by its slow acquisition speed, which can reach up to 10 minutes per module. Furthermore, the electronic device cannot be integrated into the PV string, making it necessary to disconnect the module prior to EL testing.

Daylight Photoluminescence (External electrical modulation)

Similar to daytime EL with a power supply, it is possible to modulate the PL signal using an electronic system connected to the PV system that alternates between OC and SC conditions [70], where PL emission is high and low respectively, thus enabling PL modulation. In fact, the previously mentioned DaySy system [73] includes this functionality.

Although disconnection is still required, an electronic system that allows switching between OC and SC is much simpler, less bulky, and cheaper than a power supply. Additionally, it does not require a significant amount of energy from batteries or a generator, thereby reducing the complexity of the acquisition set-up.

Daylight Photoluminescence (Internal electrical modulation)

Electronic devices can be designed and installed within PV power plants. These devices, based on switches, can be strategically placed throughout the plant to alter the operating points of multiple PV modules for proper PL signal modulation [75]. The permanent installation of such devices allows measurements to be performed without requiring module disconnections.

For PV string inverter configurations, the electronic device must be installed in parallel with the appropriate number of modules. The device can bypass the group of modules. When the PV modules are bypassed, the inverter voltage does not drop immediately, causing the remaining modules in the string to increase their operating voltage. If the number of bypassed modules is adequate, the voltage in the remaining modules can reach OC conditions. Without bypassing, the full string operates at MPP. Alternating between these two states enables PL modulation.

For PV array inverter configurations, electronic devices are installed in series with each PV string. The device can individually isolate any string, setting it to OC conditions. Strings that are not isolated have all their modules operating at MPP. Alternating between these two states enables PL modulation.

Daylight Photoluminescence (Optical modulation)

It is possible to achieve luminescence signal modulation without disconnections by using a system that controls the lighting level on several strategic cells of the module [76,77]. One lighting module is installed to cover a single solar cell, blocking sunlight. When the lighting module is off, no current is generated by that solar cell, setting it and all cells in the same substring to OC conditions. Since PV modules typically have several substrings (commonly 3), multiple lighting modules are required to set OC conditions across the entire module. Conversely, if the lighting modules provide irradiance equivalent to the ambient level, all cells operate at MPP. Alternating between OC and MPP conditions enables PL signal modulation, which also allows lock-in integration.

The main advantage of this technique is that sunlight is used as the excitation source, and no disconnections are required. However, this method presents several challenges and limitations. First, multiple lighting modules are needed to image a single solar module. Second, two measurements are required to capture the PL signal from all the solar cells of the module. Finally, the system requires manual installation of the lighting modules, which reduces the overall throughput of the technique.

To overcome these limitations, it is possible to modulate the PL signal of an entire PV string by installing lighting modules on only a fraction of the modules in that string [78,79]. This system is only applicable in large PV plants where a single MPPT system controls a large PV array. The large inverter system sets a common voltage for all the strings in the array. When several modules within one string are induced to OC by the lighting modules, current in these modules flows through bypass diodes. As a result, the remaining modules increase their voltage to maintain the common strings voltage set by the inverter. This voltage increase toward V_{OC} allows the remaining modules to reach OC conditions if an adequate number of modules are bypassed. This method enables PL modulation across the entire string without disconnections and with higher throughput.

Daylight Photoluminescence (Inverter modulation)

PV inverters can also be used to change the operating point of the PV system, enabling PL signal modulation. During MPP conditions, the PL signal is nearly null, whereas it reaches its maximum under OC conditions. This method stands out for its non-invasive nature and the fact that it does not require any additional hardware to achieve PL modulation.

Depending on the inverter characteristics and control parameters, the transition between OC and MPP can be fast enough to enable proper periodic PL modulation, allowing the implementation of the lock-in technique [80].

Conversely, some inverters require several seconds (around 5–6 s) to switch from OC to MPP. In such cases, PL signal modulation is too slow [81,82], and the resulting long measurement times are negatively affected by changes in irradiance. As an alternative, a batch measurement approach can be implemented [83], involving a single switching event: first acquiring all images under null PL emission, followed by all images under high PL emission. Additionally, to improve image quality, irradiance can be measured for each frame within the sequence, allowing normalization to minimize the impact of irradiance fluctuations.

Daylight Photoluminescence (I-V curve sweep modulation)

This technique is based on the capability of some PV inverters to trace the I-V curves of PV strings [84,85]. During the I-V sweep, the modules operate at two reference points where the PL signal is null and high. Before the sweep begins, the inverter sets SC conditions, where the PL signal is negligible. The I-V curve is then swept from SC to OC, reaching the point where the PL signal is maximized. If a sequence of images is captured just before and after the I-V curve sweep, it is possible to extract the necessary frames for further processing using a batch approach.

Although this method enables non-invasive measurement, it is limited by a key factor: the time spent at SC and OC conditions is dictated by the nature of the I-V curve sweep. Consequently, the image acquisition speed must be adapted accordingly, typically requiring very high acquisition rates, as I-V tracing tends to be extremely fast. As a result, the use of high-speed InGaAs cameras becomes necessary.

Daylight Photoluminescence at Constant Operating Point

This method enables the application of a daylight lock-in technique by combining and subtracting images that differ in PL emission. Unlike conventional lock-in approaches, it does not require altering the operating point of the solar module under test [86]. Instead, all images are captured under the same operating condition (OC), using different optical filters. A standard filter is employed to record the peak PL emission, while two additional filters (one with a slightly higher and one with a slightly lower central wavelength) are selected. These auxiliary filters must be close enough in wavelength to the standard filter to ensure comparable signal noise but sufficiently offset to ensure minimal PL contribution. The resulting images can then be subtracted from the standard image to isolate the PL signal.

However, this technique has so far only been validated on high-efficiency IBC modules, which PL emission is almost two orders of magnitude higher than multicrystalline modules. Further studies are needed to evaluate its applicability to other PV technologies and to establish it as a viable inspection method for large-scale PV installations.

Daylight Photoluminescence with Ultranarrow Bandpass Filter

This technique leverages the natural absorption of sunlight by atmospheric water vapour, along with advances in ultranarrow bandpass optical filters [87]. Since water vapour concentration varies depending on geographic location, season, and weather, the atmospheric absorption spectrum also changes accordingly. Within this spectrum, there are several very narrow bands (1–2 nm) where sunlight is almost entirely attenuated. Notably, these absorption bands coincide with the spectral range of luminescence emission. As a result, it is possible to design a custom ultranarrow bandpass filter that matches one of these bands, allowing the use of an InGaAs camera to detect the PL signal. Under these conditions, the luminescence contribution can account for approximately 90% of the total captured signal.

The main benefit of this approach is its ability to capture the PL signal under daylight conditions with a single camera shot, eliminating the need for multiple images and lock-in techniques. Although longer exposures improve image quality, even one-second acquisitions are generally sufficient to detect most defects. This short acquisition time

enables high throughput. However, the method relies on a custom-designed ultranarrow bandpass optical filter, a specialised lens system, and a low-noise InGaAs camera, all of which introduce technical and operational challenges. In addition, the performance of the filter is sensitive to atmospheric water vapour concentration, which may vary with location and weather conditions.

3.3. Luminescence imaging with Unmanned Aerial Vehicles

The use of Unmanned Aerial Vehicles (UAVs) for luminescence imaging in PV power plants has gained significant interest in recent years [88]. Integrating UAVs enables the automation of inspections and increases measurement speed, essential factors when inspecting the thousands of modules that comprise utility-scale PV plants. In this context, ground-based inspections are not feasible for large PV systems, as they are considered time-consuming and inefficient [89]. Aerial inspections not only reduce the time required for EL and PL imaging but also enable the inspection of installations such as rooftop PV systems or floating PV systems, which are difficult or impossible to assess using ground-based methods [89]. Finally, automated EL or PL acquisition through aerial inspections, combined with artificial intelligence techniques, holds significant potential for utility-scale PV power plants by enabling the automatic detection and classification of faults [90–92].

Regarding conventional dark EL during nighttime, manual ground inspections can reach rates of approximately 30 kW_p (100–200 modules) per hour [32]. In contrast, aerial inspections can significantly increase measurement rates, achieving up to 1,200–1,500 modules per hour [88]. Although silicon-based cameras can be used for nighttime inspections [93], they require long exposure times, which slows down acquisition and necessitates stopping the drone during image capture. In contrast, InGaAs cameras enable luminescence video recording [94], allowing image acquisition while the drone is in motion thanks to shorter exposure times. It is worth noting that dark EL measurements using UAVs have been performed both with power supplies [93] and with bidirectional inverters [95].

As previously explained, daylight luminescence imaging requires acquiring several pairs of images in which the luminescence signal alternates between high and low. Capturing this image sequence using UAVs is possible [96], but it typically requires the drone to remain stationary while the sequence is acquired [97]. Additionally, image stabilization during post-processing is necessary. The use of high-speed InGaAs cameras makes it possible to capture the required sequence in approximately 1 second [96], enabling inspection rates of over 700 modules per hour.

In daylight inspections, it is also crucial that the modulation system does not limit the speed achieved by UAV-based inspections. Therefore, it is essential that PL or EL modulation can be performed rapidly in any section of the plant, preferably without requiring disconnection or the temporary installation of additional hardware in the PV system.

3.4. Summary and Conclusions

EL and PL imaging are powerful tools for fault detection in PV modules. As non-destructive techniques, they offer great potential for identifying and analysing module defects throughout the entire life cycle within a PV power plant. However, their implementation is not yet standard practice in PV maintenance plans, mainly due to the complexity of the acquisition process. While infrared thermography is widely used in commercial PV plants since it can be performed during normal operation, conventional dark EL imaging requires nighttime acquisition, the use of power supplies, and disconnection within the PV system, making it an invasive and logistically challenging method. This explains why EL imaging remains limited in practice.

For nighttime acquisition, non-invasive EL imaging is feasible if the PV power plant is equipped with a bidirectional inverter, which simplifies the measurement process. Non-invasive PL imaging using an artificial lighting system is also possible. However, both methods require additional hardware: permanent in the case of bidirectional inverters, and mobile in the case of lighting systems. Moreover, performing measurements at night is generally not desirable, as access to PV power plants during nighttime hours is often restricted due to safety concerns.

Daylight luminescence imaging has been experimentally demonstrated by several research groups worldwide. This approach involves capturing a sequence of images in which the luminescence signal alternates between high and low intensity states, enabling the integration of lock-in detection techniques to remove the background signal generated by sunlight. Various methods have been proposed by the scientific community, differing primarily in how the luminescence signal is modulated. PL imaging is more commonly used for daylight acquisition, as sunlight can serve as a natural excitation source and, with the right strategy, modulation can be achieved without requiring disconnections. In contrast, daylight EL imaging is less common, as modulating the EL signal without disconnections remains a greater technical challenge.

It is important to note that EL and PL imaging can be considered complementary techniques. While EL is more suitable under low-irradiance conditions, PL imaging performs better in high-irradiance environments. Furthermore, although both types of images provide similar information, they offer complementary insights that contribute to a more comprehensive understanding of solar cell performance.

All the techniques analysed in this state of the art are summarized in Table 2. The present thesis aims to design and validate an experimental technique that enables both non-invasive EL and PL imaging under daylight conditions, representing a novel contribution to the field. Specifically, the development of an electronic device that can be integrated into PV modules without requiring external power and capable of modulating both EL and PL signals while allowing the module to operate normally, has not been previously achieved.

Table 2. Summary of EL and PL techniques for the inspection of field-deployed PV modules.

Technique	Conditions	EL/PL	Invasive method	Lock-in	Excitation source	Equipment for signal modulation	Camera Equipment	Discussion
Conventional Nighttime EL	Dark	EL	Invasive	No	Power supply	No needed	Si or InGaAs sensor	Dark conditions allow imaging with a single camera shot. However, it requires module disconnection and the use of a power supply, typically provided by a generator. These disconnections and the need for nighttime acquisition introduce both safety and operational challenges.
Bidirectional Inverter	Dark	EL	Non-invasive	No	Bidirectional inverter	No needed	Si or InGaAs sensor	Dark conditions allow imaging with a single camera shot. The use of a bidirectional inverter, capable of injecting current into the PV array, enables measurements without the need for disconnections, thereby increasing speed and reducing safety risks. However, bidirectional inverters are not commonly used in PV plants due to their higher investment costs.
Protective Box	Dark	EL	Invasive	No	Power supply	No needed	Si or InGaAs sensor	Dark conditions allow imaging with a single camera shot, but they require disconnection of the module and the use of a power supply, typically provided by a generator. The use of a protective box can create dark conditions during daytime; however, disconnection is still required.
Mobile EL Laboratory	Dark	EL	Invasive	No	Power supply	No needed	Si or InGaAs sensor	Dark conditions created within a mobile laboratory enable high-quality results, complemented by I–V curves and additional measurements. However, this approach not only requires disconnection but also disassembly of the module, which increases acquisition time, safety risks, and the potential for physical damage in the PV module.
Nighttime PL with Artificial Lighting	Dark	PL	Non-invasive	No	Lighting system	No needed	InGaAs sensor	Dark conditions allow imaging with a single camera shot, and the use of an external lighting device to induce PL emission enables measurements without the need for disconnection. However, the main drawback is the need to transport the lighting device along with its power supply and battery, which adds complexity and logistical challenges to the measurement process.

Daytime EL with Power Supply	Daylight	EL	Invasive	Yes	Power supply	Power supply	InGaAs sensor and optical filter	The implementation of a lock-in technique using a power supply to modulate the EL signal allows measurements to be performed under daylight conditions. However, disconnection of the module is still required, and a sequence of multiple images must be acquired to effectively filter out the luminescence emission from ambient light.
Self-Sourced EL	Daylight	EL	Invasive	Yes	PV module energy	Electronic board	InGaAs sensor and optical filter	The implementation of a lock-in technique using an electronic board capable of injecting current into the module by harvesting energy from the module itself enhances EL signal modulation. This approach eliminates the need for an external power supply; however, disconnection is still required, as the board cannot operate under normal PV plant conditions. Additionally, acquisition speed remains low due to the need for image sequences and the limited performance of the electronic board.
Daylight PL (External electrical modulation)	Daylight	PL	Invasive	Yes	Sunlight	Electronic board	InGaAs sensor and optical filter	Sunlight is used as the excitation source, while an electronic board modulates the PL signal by alternating between open-circuit and short-circuit conditions. This approach enables measurements during daytime without the need for an external energy source; however, module disconnection is still required.
Daylight PL (Internal electrical modulation)	Daylight	PL	Non-invasive	Yes	Sunlight	Electronic device installed in the PV power plant	InGaAs sensor and optical filter	Sunlight is used as the excitation source, and electronic devices are permanently installed within the PV power plant, enabling PL modulation without disconnection. Although the measurements are non-invasive, additional hardware must be installed in the PV plant.
Daylight PL (Optical modulation)	Daylight	PL	Non-invasive	Yes	Sunlight	Optical modulators	InGaAs sensor and optical filter	Sunlight is used as the excitation source for PL modulation combined with a lock-in detection technique, which requires the acquisition of an image sequence. In this approach, modulation is achieved without the need for module disconnection; however, an optical modulator must be strategically installed on specific control cells within the module.
Daylight PL (Inverter modulation)	Daylight	PL	Non-invasive	Yes	Sunlight	Inverter (via MPPT)	InGaAs sensor and optical filter	Sunlight is used as the excitation source for PL modulation combined with a lock-in detection technique, which requires a sequence of images. In this approach, modulation is achieved through the PV inverter by alternating between maximum power point and open-circuit conditions. Neither module disconnection nor additional hardware is required.

Daylight PL (I-V curve sweep modulation)	Daylight	PL	Non-invasive	Yes	Sunlight	Inverter (via I-V tracing functionality)	High speed InGaAs sensor and optical filter	Sunlight is used as the excitation source for PL modulation combined with a lock-in detection technique, which requires the acquisition of a sequence of images. Modulation is achieved through the I-V curve tracing functionality available in some PV inverters. This method does not require module disconnection or additional hardware; however, it requires a specialized inverter as well as a high-speed InGaAs camera.
Daylight PL at Constant Operating Point	Daylight	PL	Non-invasive	Yes	Sunlight	Three different optical filters	InGaAs sensor and two optical filter	Sunlight is used as the excitation source for PL modulation combined with a lock-in detection technique, which requires the acquisition of a sequence of images. In this approach, measurements can be performed at the same operating point by modulating the signal using three different optical filters. However, the need to switch between filters can slow down the measurement process.
Daylight PL with Ultranarrow Bandpass Filter	Daylight	PL	Non-invasive	No	Sunlight	No needed	InGaAs sensor and ultranarrow bandpass filter	Sunlight is used as the excitation source. Only a single shot is required, thanks to an ultranarrow bandpass filter selected within a narrow and deep absorption band of H_2O. This approach allows rapid measurements without module disconnection or additional hardware. However, it requires a custom and expensive filter that only functions correctly under specific atmospheric H_2O concentrations.

Chapter IV

Design of Module-level Electronics for Non-Invasive Luminescence Signal Modulation

In this chapter, the design and validation of a module-level electronic device is presented. Its purpose is to enable non-invasive EL and PL signal modulation once installed within a PV module, meaning that after installation it operates without interfering with the normal behaviour of the PV system. First, the hardware requirements are defined. Then, the proposed topology is introduced, followed by an evaluation of its electrical performance in a real-world scenario. Next, instructions are provided on how to modify the board to switch from binary to arbitrary modulation, specifically for EL modulation. Finally, a discussion of the device's functionalities is presented.

4.1. Requirements of the Module-level Electronic Device

Since the electronic board is intended to be permanently installed within a PV string, specifically in each PV module where EL or PL signal modulation is required, the following requirements are desirable:

1. **Normal Operation Compatibility**: the electronic board must allow the PV module to operate normally, following MPP dictated by the inverter. Additionally, power losses introduced by the board during normal operation should be negligible. Operating near the MPP also provides a useful reference point where luminescence emission is minimal.

2. **EL Modulation Capability**: the electronic board should be capable of inducing a forward-bias current in the module by using the string current as the excitation source for EL signal modulation. The modulation should be fast enough to periodically vary the EL emission intensity multiple times per second, enabling the lock-in detection technique.

3. **PL Modulation via Bypass**: the electronic board should be able to bypass the PV module, allowing it to operate under OC conditions, which enhances PL modulation. As with EL, the modulation must be sufficiently fast to periodically vary the PL emission intensity several times per second, facilitating the lock-in detection technique.

4. **Self-Powered Operation**: the electronic board should function without a battery or external power source. Ideally, it should include a system to power the electronics using the energy generated by the PV module itself.

5. **Simplicity of Topology**: the circuit topology must be as simple as possible. Since module-level integration requires low-cost and compact solutions, minimizing circuit complexity is essential for practical implementation.

6. **External Control Interface**: the device must include a communication system that allows external control and configuration of the modulation parameters.

4.2. Power Topology and Circuitry

Concept

The proposed electronics are designed to modify the operating point of the PV module along the I-V curve. As shown in Figure 4, the intensity of both EL and PL signals depends on the specific operating point of the module under illumination.

- At the MPP: EL emission is negligible, and PL signal is nearly zero.
- Under OC conditions: EL emission is absent, while the PL signal reaches its maximum intensity.
- Under FB current: EL emission is high, and the PL signal also remains at its maximum.

Therefore, by shifting the operating point between MPP, OC, and FB current conditions, it is possible to modulate both EL and PL signals, which allow imaging under high irradiance conditions thanks to the integration of lock-in technique. The concept behind the developed module-level electronic device is based on a four-switch topology arranged in a half-bridge configuration. As shown in Figure 13, the half-bridge is connected to the PV module whose operating point is to be modified. At the same time, it is connected to the string, specifically to the positive terminal of the preceding module ($+_{STRING}$) and the negative terminal of the subsequent module ($-_{STRING}$).

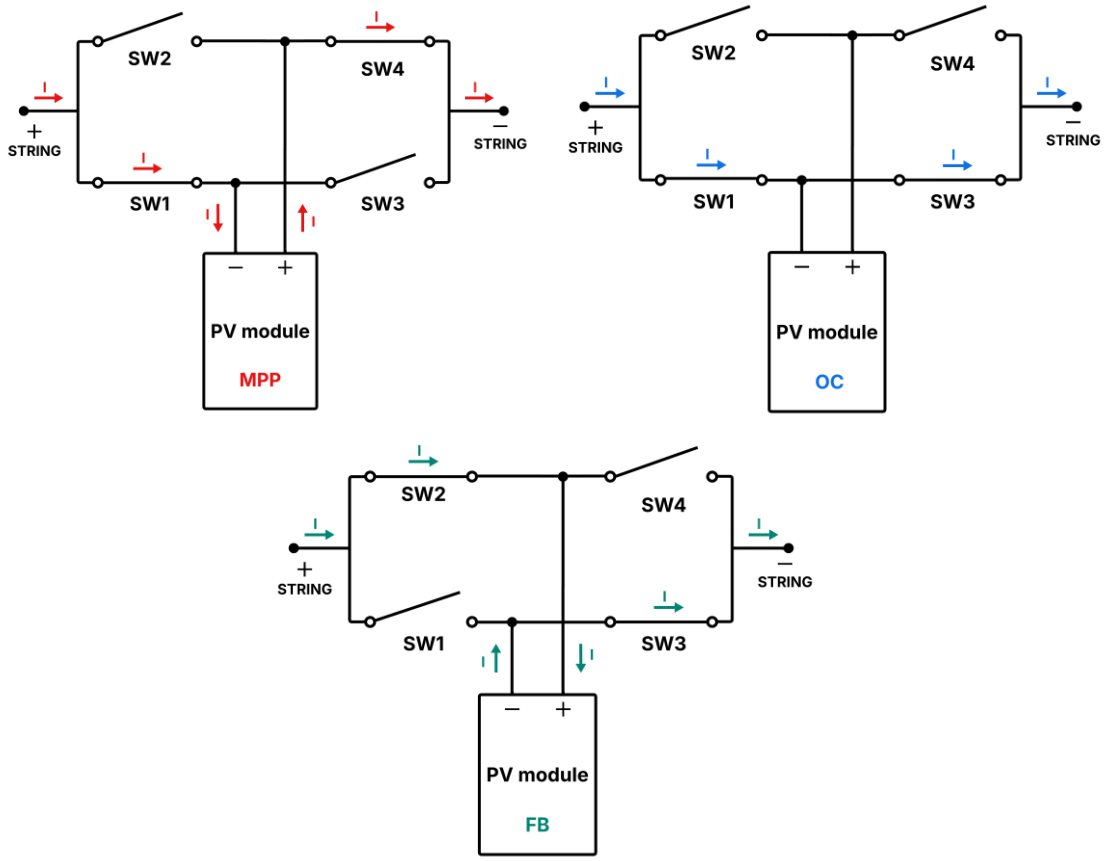

Figure 13. Concept of the module-level electronics for PL and EL modulation. Topology based on four switches (SW_1, SW_2, SW_3, and SW_4) forming a half-bridge configuration.

If SW_1 and SW_4 are closed while SW_2 and SW_3 are open, current flows from the positive terminal of the string to the negative terminal of the module, and from the positive terminal of the module to the negative terminal of the string. This configuration allows normal operation of the module, which will operate at MPP if the PV inverter is active.

If SW_1 and SW_3 are closed while SW_2 and SW_4 are open, no current flows through the module, effectively bypassing it. In this state, the module operates under OC conditions.

Finally, if SW_2 and SW_3 are closed while SW_1 and SW_4 are open, a forward-bias current is applied to the module. In this configuration, the positive terminal of the string is connected to the positive terminal of the module, and the negative terminal of the module is connected to the negative terminal of the string, allowing the module to operate in the fourth quadrant as a load.

Power Topology

The implemented power topology is shown in Figure 14. In this schematic, two of the four switches from the original concept have been replaced by MOSFETs, while the remaining two have been replaced by diodes. Additionally, Figure 14 includes a truth table indicating which MOSFETs must be conducting to achieve the different operating points required for EL and PL modulation.

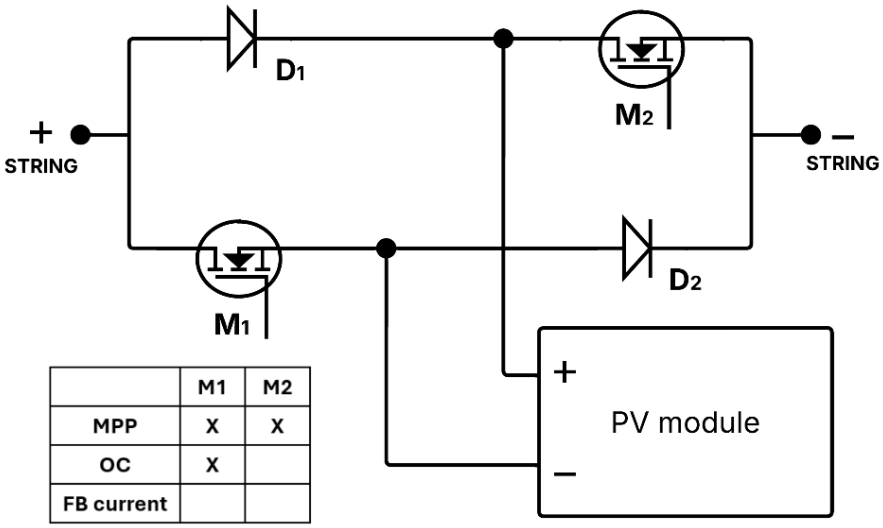

	M1	M2
MPP	X	X
OC	X	
FB current		

Figure 14. Implemented power topology in the module-level electronic device for EL and PL modulation, and truth table indicating with an "X" the MOSFETs that must be conducting to achieve different conditions.

Note that it would be possible to implement a power topology based on four MOSFETs; however, the chosen configuration offers several advantages. First, using only two transistors simplifies the control of the board and reduces the total number of components. Second, the inclusion of two diodes provides a continuous current path, which enhances the robustness of the board. Using four MOSFETs could create scenarios where, if all of them are off, the full string voltage is applied across the electronic device, potentially exceeding the voltage ratings of some components and risking damage.

While current flows through the diodes, power loss occurs due to the voltage drop across them. However, during normal operation of the module, both MOSFETs are on, and the entire current flows through them. Power MOSFETs exhibit a very low voltage drop because of their low on-resistance, resulting in negligible power loss.

Before the real implementation of this topology, it was validated through simulations in LTspice, using the one-diode model [98] to simulate the electrical behaviour of a PV module. The characteristics of the simulated PV module, as well as the PV string, are shown in Table 3. Note that the simulated PV string is connected to a static load that sets the MPP in the normal configuration of the string (Z_{MPP}).

Table 3. Characteristic of the simulated PV module and PV string.

PV Module characteristics	PV string characteristics
V_{OC}: 45.7 V	Size: 8 modules
I_{SC}: 8.6 A	Load: Z_{MPP}
V_{MPP}: 35.0 V	
I_{MPP} 7.8 A	

The main results of the simulations can be seen in Figure 15. Through proper control of both MOSFETs (M_1 and M_2), it is possible to set MPP, OC, and FB current in the PV module where the proposed electronic architecture is installed.

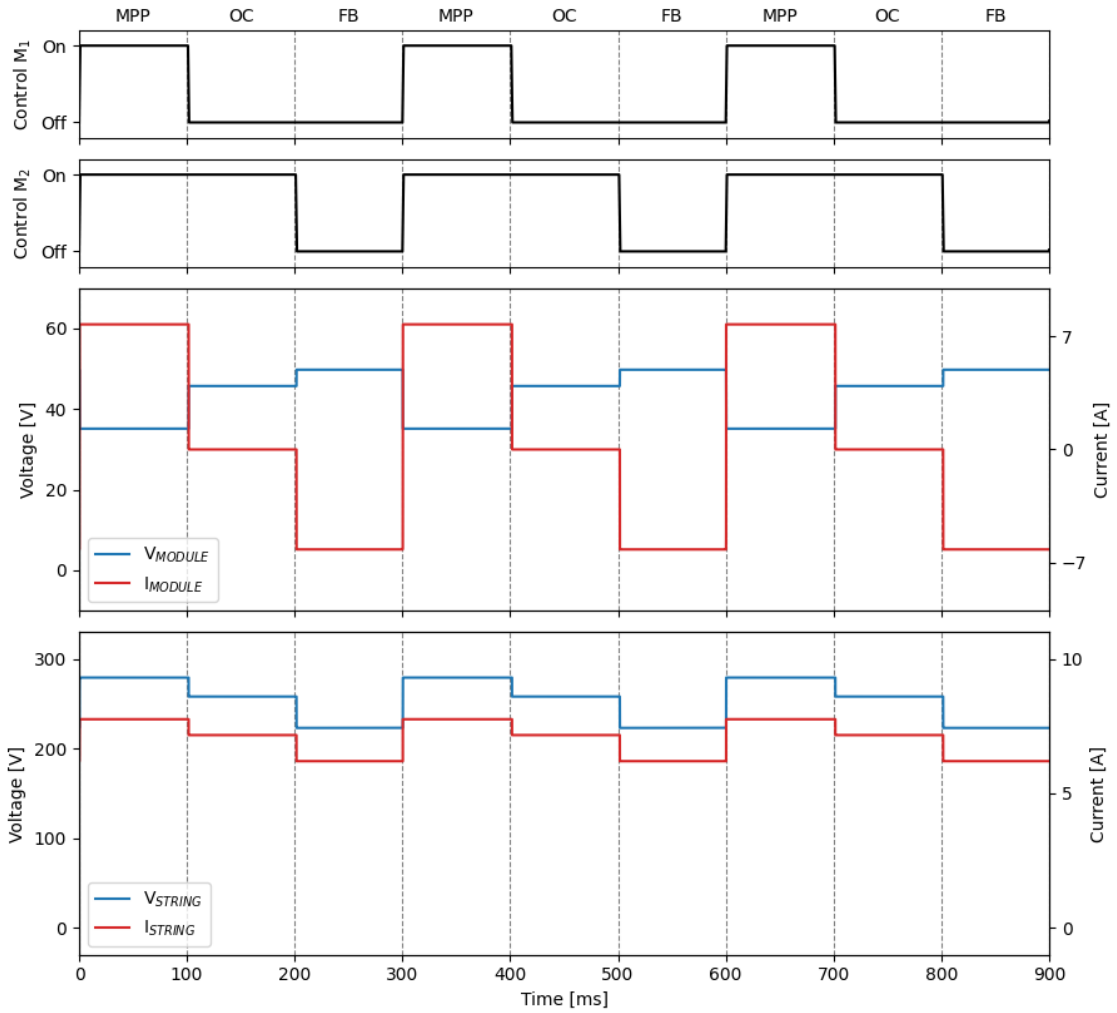

Figure 15. Simulation of current and voltage evolution using the power topology of the developed electronic board in a PV string composed of eight modules.

When M_1 and M_2 are on, the module current remains positive at I_{MPP}, indicating that the module is operating at MPP together with the PV string. When M_1 is off while M_2 is on, the module is bypassed, so no current flows through it. As the PV string is connected to a static load, a reduction in the total voltage corresponding to one module is observed. Moreover, the bypass of one PV module modifies the aggregated I-V curve of the string, which explains the current drop observed in the string current. Finally, when M_1 and M_2 are off, forward-bias current is set in the module. During this state, the string voltage is reduced, corresponding to slightly more than the voltage of two modules. This also changes the equivalent I-V curve of the string, which explains the reduction in string current compared with MPP conditions.

These results validate the functionalities of the presented power topology. However, it should be noted that the simulations were performed with the PV string connected to a static load, which may not represent the real behaviour of a PV inverter.

Implementation

This power topology has been implemented on a two-layer printed circuit board (PCB) based on the PIC16F1619 microcontroller, whose full schematic can be found in Annex I. The board has dimensions of 73 × 85 mm, and four MC4 connectors have been attached to facilitate its installation within a PV string, where two connectors are attached to the module to be tested, while the other two are connected to the positive terminal of the previous module in the string and the negative terminal of the following module. The bottom and top views, as well as the assembled board, are shown in Figure 16.

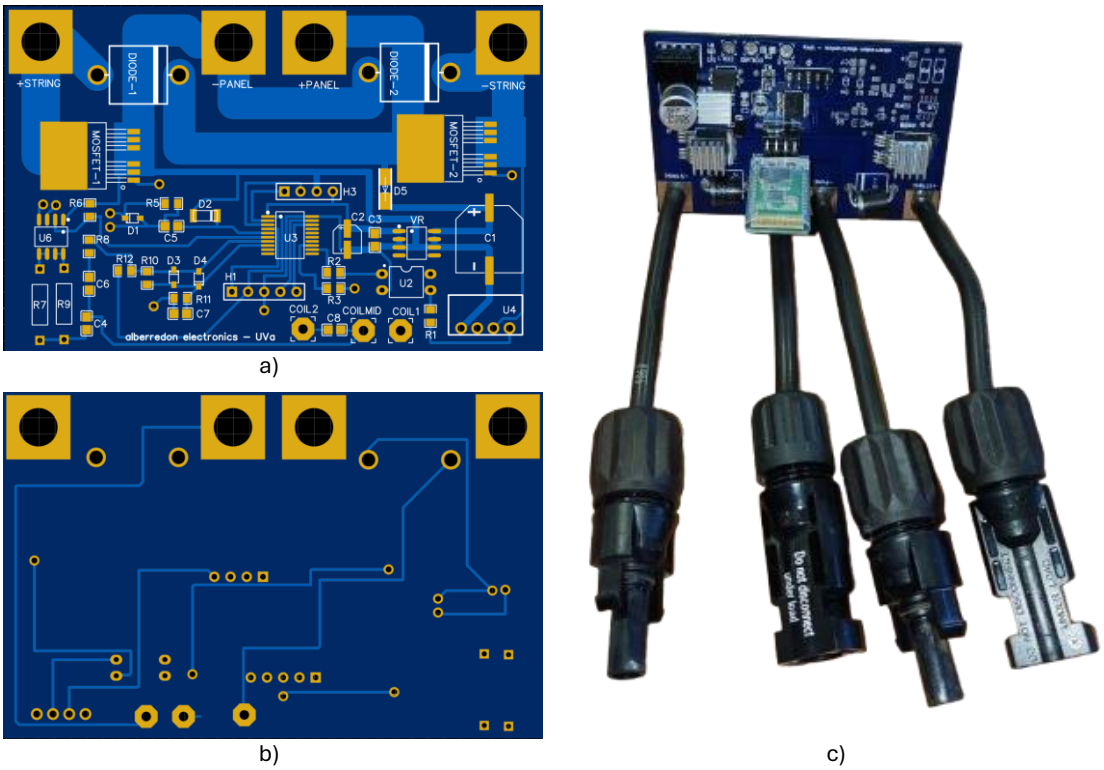

Figure 16. Views of the developed electronic board: top side (a), bottom side (b), and photograph of the assembled board (c).

Apart from the power circuit, the board includes other circuitry for supply, control, and communications. First, it features a simple supply system based on a linear voltage regulator (see Figure 17). Its input is connected to the positive terminal of the module through a diode, which blocks reverse current and thus protects the system. The negative terminal of the panel is set as the ground of the board, and the output provides a constant 5 V to power the microcontroller and other systems. This circuitry allows the module to power the electronic board without the need for an external supply or batteries.

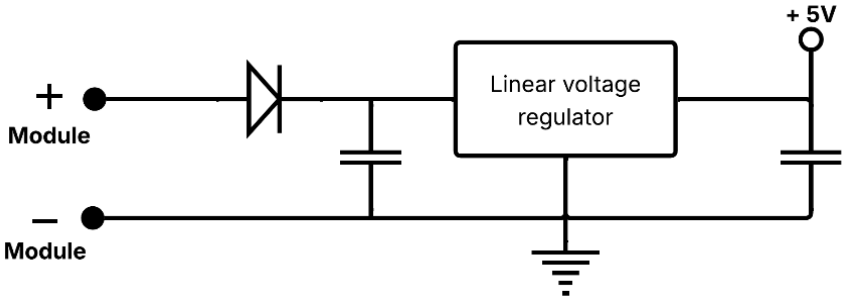

Figure 17. Supply system for the developed electronic device.

MOSFETs are controlled by applying a voltage between their source and gate terminals. Since the negative terminal of the module is the ground of the board, only M_1 has its source terminal connected to ground, while M_2's source is floating. Therefore, M_1 can be directly controlled by one of the microcontroller's digital outputs, whereas M_2 cannot.

The control system for M_2 is shown in Figure 18. It is based on an isolated DC-DC converter and an optocoupler. The isolated DC-DC converter creates an isolated 5 V source referenced to M_2's source, which corresponds to the negative terminal of the string. The optocoupler allows this 5 V to be applied or not to the gate of M_2, enabling its switching operation.

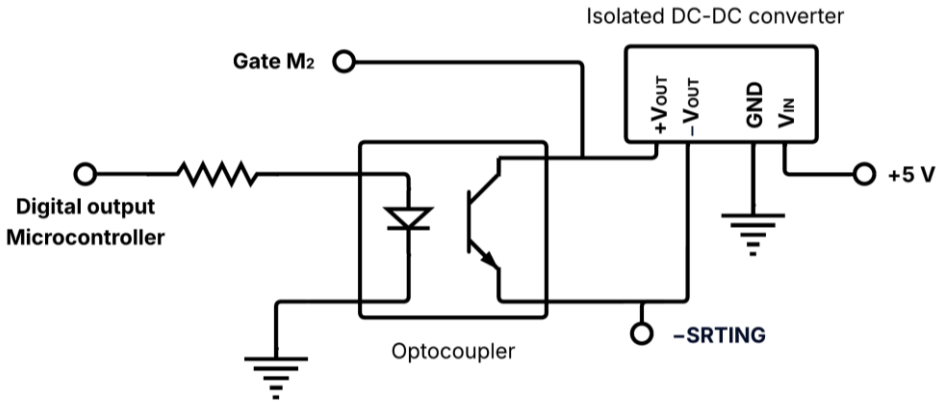

Figure 18. Control system for the developed electronic device.

Regarding communication, the developed electronic device offers two options:

- Bluetooth: the board includes a header that is connected to the UART (Universal Asynchronous Receiver/Transmitter) pins of the microcontroller, as well as to ground and 5 V. This enables connection of a Bluetooth module (HC-06), allowing wireless control of the board. This system provides a useful, simple, and quick way to test and control the board, while wireless communication also ensures isolation for safety purposes.

- Power Line Communication (PLC): The board also incorporates a PLC system designed for PV power plants [99,100]. This system allows communication between a device installed in the inverter and the board.

Finally, all the components used in the development of the electronic device are listed in Table 4. This allows calculation of the total cost of the board, which amounts to up to 13.26 € per unit. This cost only includes the components and does not cover design or manufacturing/soldering time. Note that this total cost is the result of the chosen components, which can be optimized to reduce expenses. Moreover, prices may vary over time depending on the supplier and the quantity purchased. Nevertheless, it provides a useful reference for the total price.

Table 4. List of components and prices used in the developed electronic board. Unit prices for 2025 correspond to purchases of at least 100 units.

System	Part	Reference	Units	Unitary price	Total price
Power	MOSFET	AUIRLS3036-7P	2	1.71 €	3.42 €
Power	Diode	15SQ045	2	0.59 €	1.18 €
Supply	Diode	1N4004	1	0.04 €	0.04 €
Supply	Voltage regulator	LM2936MX-3.3/NOPB	1	1.25 €	1.25 €
Supply	Capacitor 100 µF	EEV107M063A9PAA	1	0,36€	0,36€
Supply	Capacitor 10 µF	EDH106M016A9BAA	1	0.08 €	0.08 €
Control	Microcontroller	PIC16F1619-E/SS	1	1.20 €	1.20 €
Control	MLCC Capacitor	-	1	0.02 €	0.02 €
Control	DC-DC Converter	B0505S-1W	1	0.62 €	0.62 €
Control	Optocoupler	SFH610A-2	1	0,43 €	0,43 €
Control	SMD resistor	-	4	0.01 €	0.04 €
Communications	Diode	BAT60JFILM	3	0.10 €	0.30 €
Communications	Diode	PMLL4150	1	0.37 €	0.37 €
Communications	MOSFET	TSM8588	1	0.36 €	0.36 €
Communications	SMD resistor	-	6	0.01 €	0.06 €
Communications	TH resistor	-	2	0.04 €	0.08 €
Communications	MLCC Capacitor	-	5	0.02 €	0.10 €
Communications	Coil	-	1	0.80 €	0.80 €
Communications	Bluetooth module	HC-06	1	1.79 €	1.79 €
PCB	Board	-	1	0.81 €	0.81 €
Total price					**13,26 €**

4.3. Performance of the Electronic Device

The performance of the electronic module-level device was tested in a real PV facility composed of 10 multicrystalline PV modules (TSM-235-PC05A) with a nominal power of 235 W_p each. All modules form a string connected to a 1,500 W_p string PV inverter (Sunny Boy SB1.5-1VL-40). The electronic device is integrated within one of the modules in the string.

First, it is possible to analyse the current evolution in the module during EL and PL modulation to evaluate whether the luminescence signal is properly modulated. For proper EL or PL modulation, it is crucial to change the operating point of the module as illustrated in Figure 4. For EL modulation, the operating point must be switched between OC (PL + background signal) and forward-bias current (EL + PL + background signal). In contrast, PL modulation involves switching between MPP (background signal) and OC (PL + background signal).

Figure 19 displays the current evolution in the tested PV module while the EL and PL signals are being modulated at a frequency of 5 kHz. During EL modulation, it can be observed how the current changes from a null value (OC conditions) to a high negative current (forward-bias current), indicating that the module operating point is properly adjusted for EL signal modulation. During PL modulation, the module current evolves from a high current level close to MPP (null luminescence signal) to near-zero current levels (OC conditions), indicating that the module operating point is properly adjusted for PL signal modulation.

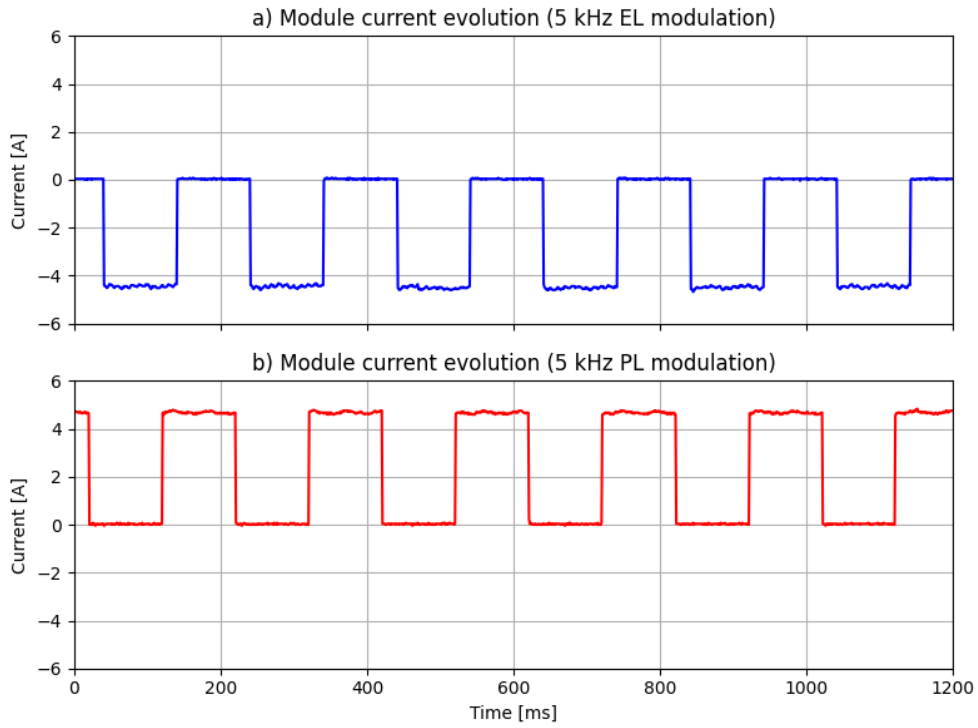

Figure 19. Module current evolution during EL (a) and PL (b) modulation at 5 kHz, measured in a PV string configuration with an oscilloscope (RS PRO Siglent SHS820X).

It may also be important to analyse how the string current evolves, ensuring the proper performance of the PV inverter, which must not stop operating during luminescence signal modulation. For both EL and PL modulation, the string current changes at the same frequency as the modulation. However, the current variation is significantly higher during EL modulation compared to PL modulation, which is fully consistent with the fact that while PL involves a voltage reduction corresponding to bypassing a single PV module, EL involves a voltage reduction corresponding not only to the loss of one PV module but also to the negative voltage drop in the string due to the higher voltage than V_{OC} required for forward-bias current induction. This behaviour can be observed in Figure 20.

Nevertheless, although the developed electronic device involves current variations in the string, it successfully changes the operating point of the tested module for proper EL and PL modulation, while keeping the PV string under normal operation.

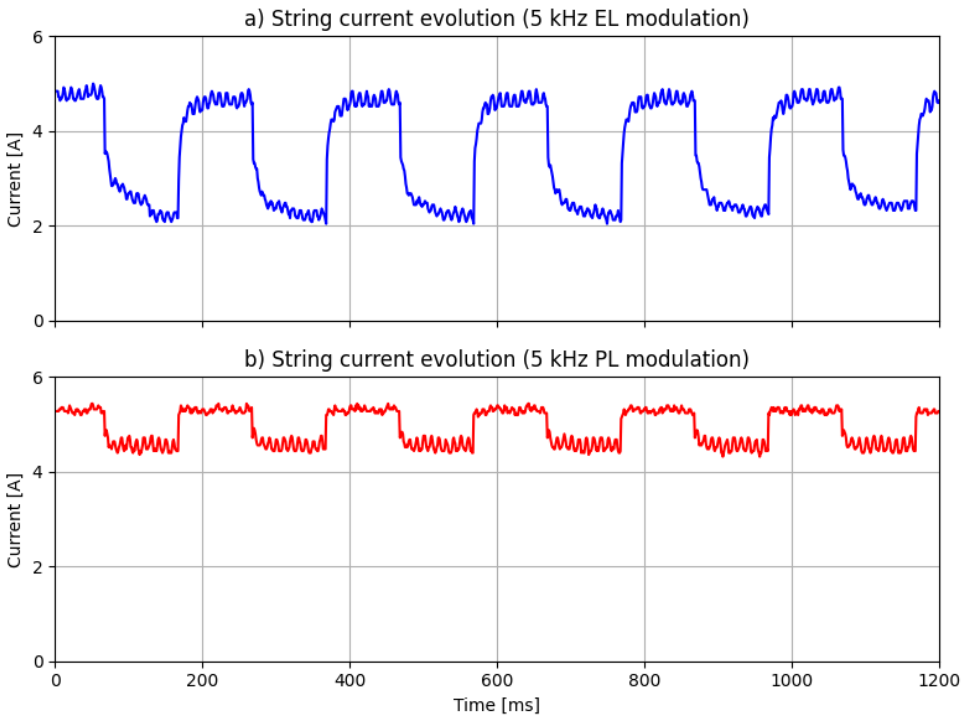

Figure 20. String current evolution during EL (a) and PL (b) modulation at 5 kHz, measured in a PV string configuration with an oscilloscope (RS PRO Siglent SHS820X).

4.4. Modification for Arbitrary Electroluminescence Signal Modulation

The presented power topology allows binary modulation of the EL and PL signals. However, it is possible to achieve arbitrary signal modulation through modifications to the electronic device, which may be of interest, as the following chapter shows. These modifications involve both hardware and software changes.

It should be noted that arbitrary modulation of the signal has only been implemented for the EL signal. As shown in Figure 4, the EL signal depends linearly on the forward-bias current. Therefore, arbitrary modulation of the EL signal is as simple as modulating the forward-bias current in the PV module, which can be easily implemented using an open-loop control. Nevertheless, the PL signal does not exhibit a linear relationship with the module current, which prevents direct implementation using the same approach.

Regarding software, it is necessary to control both MOSFETs through PWM. In the present implementation, a 5 kHz PWM signal controls both switches. Regarding hardware, an LC low-pass filter must be included between the power topology of the electronic device and the tested PV module, as shown in Figure 21. The LC low-pass filter must have a cut-off frequency lower than that of the PWM control signal, allowing the square current waveform generated by the half-controlled H-bridge to be filtered. In the present implementation, the LC low-pass filter consists of a 40 µH inductor and a 1,000 µF capacitor, resulting in a cut-off frequency of 0.8 kHz.

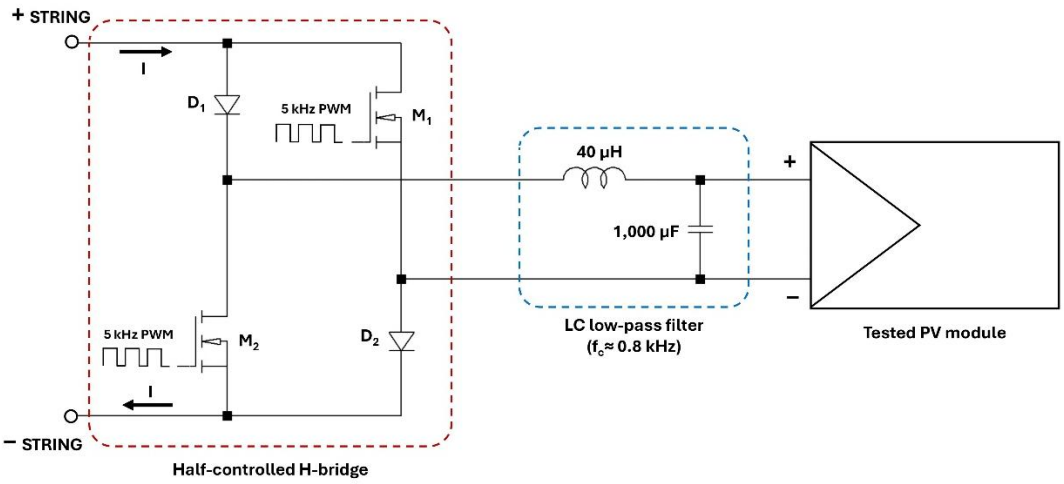

Figure 21. Modified power topology of the electronic device for arbitrary EL signal modulation. Reproduced from [101].

For forward-bias current modulation, one of the MOSFETs must remain off (duty cycle of 0%), while the other is controlled with a variable duty cycle. When the duty cycle of this MOSFET is 0%, the forward-bias current is at its maximum. When the duty cycle is 100%, the forward-bias current is null, achieving OC conditions. For example, if the duty cycle is 30%, the forward-bias current corresponds to 70% of the maximum forward-bias current obtained at a duty cycle of 0%.

The microcontroller of the board has in its memory a list of duty cycle values corresponding to the several waveforms that are to be modulated. The use of an internal timer in the microcontroller allows to periodically change the duty cycle according to the list, thus modulating the forward-bias current with a known frequency and waveform.

Figure 22 includes the modulation of three different waveforms: square, full sine and half sine. All 4 Hz waveforms have been captured using an oscilloscope in a real PV string made up by 10 modules connected in series to a PV string inverter. Some noise is noticeable, especially in the half-sine and full-sine modulations. Potential strategies to mitigate this noise include increasing the PWM frequency, using a low-pass filter with a lower cut-off frequency, or enhancing the code execution speed to allow more frequent updates of the MOSFETs' duty cycle. Nonetheless, this noise will be partially or even completely suppressed by the camera, as the signal is integrated over the exposure time of each capture.

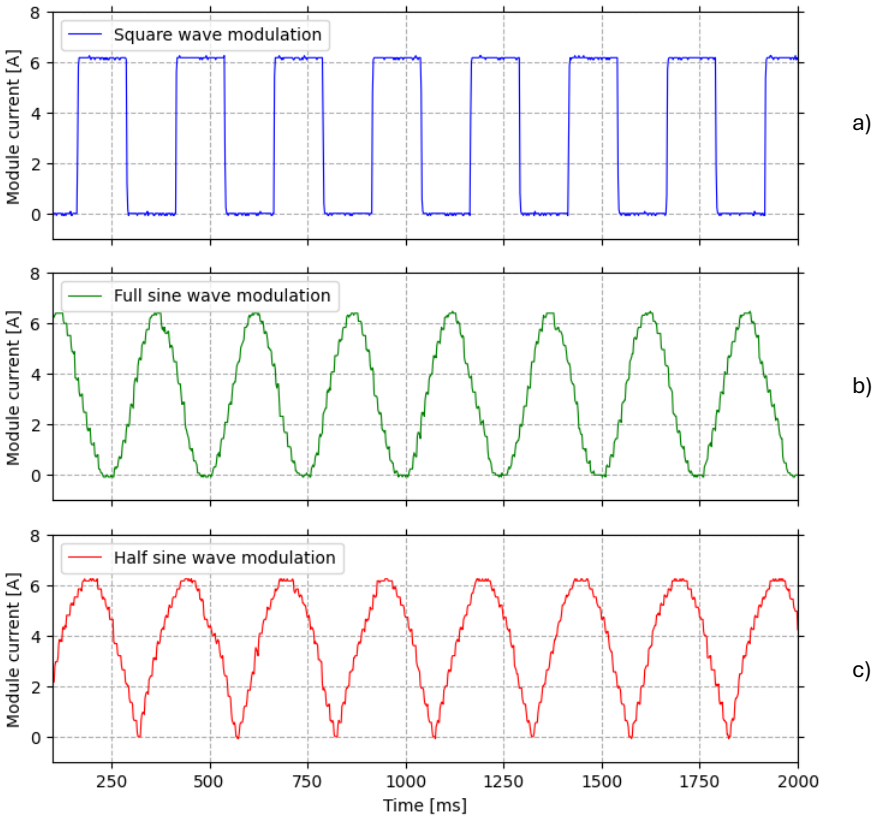

Figure 22. Module forward-bias current for square (a), full sine (b), and half sine (c) wave modulation. Measured with oscilloscope RS PRO Siglent SHS820X. Reproduced from [101].

Regarding prices, the modifications include one 1,000 µF capacitor and one 40 µH inductor, which increase the total price of the electronic device from 13.26 € per unit (see Table 4) to 15.49 € per unit. Note that it is possible to reduce the size of the inductor and capacitor by increasing the frequency of the PWM control signal, thereby reducing the additional cost.

4.5. Discussion

The present chapter has shown the design and successful validation of a module-level electronic device that can be installed within a PV string and enables EL and PL modulation under daylight conditions without the need for an external energy source, as it uses the string current to set the forward-bias current in the module for EL modulation and sunlight for PL modulation.

The electronic device is based on a half-controlled H-bridge configuration, whose proper control allows adjustment of the module operating point, thus enabling EL and PL signal modulation. It can impose OC conditions by bypassing the PV module (resulting in a high PL signal) or set a forward-bias current (resulting in a high EL signal). It also allows the module to operate under the current set by the inverter, achieving MPP conditions, which in turn provides a reference point where the EL and PL signals are null or low.

The electrical performance of the electronic module has also been successfully validated both through simulation and in a real scenario corresponding to PV string of 10 modules connected to a PV inverter. Overall, when compared with other techniques for EL and PL imaging, the present approach offers a series of advantages that are highly desirable for field inspections:

- It allows both EL and PL modulation during daylight conditions without the need for disconnections, provided that one electronic device is installed in each PV module where the luminescence signal is to be modulated. This transforms EL and PL imaging into truly non-invasive techniques. While other methods have achieved non-invasive PL modulation, non-invasive daylight EL has not previously been demonstrated.
- No external energy is required, since sunlight is used for PL signal generation and the string current is used for EL signal generation. This eliminates the need for a dedicated power supply or lighting device for luminescence signal generation, thereby reducing both the required equipment and the logistical complexity of the technique.
- Module-level integration allows selective modulation of the luminescence signal in the specific PV modules targeted for measurement. This ensures that other PV modules in the string continue to operate around their MPP, thus minimizing energy losses in the PV power plant during inspection.
- The fact that measurements can be performed during daylight is particularly advantageous, as nighttime inspections are often undesirable due to safety concerns or potentially adverse weather conditions.
- Both EL and PL imaging are desirable, as these two kinds of images can provide complementary information.
- The electronic system of the device can operate without the need for batteries, thanks to the inclusion of an internal supply stage that regulates the module voltage to the constant level required by the microcontroller and other board components.
- Finally, the electronic device features a simple topology, which enables a compact and low-cost solution, an essential aspect for practical integration of electronics into the thousands of PV modules that constitute utility-scale PV power plants.

In contrast, some limitations can also be attributed to the present modulation approach:

- Although the electronic device features a simple topology with a total component cost of only 13.26 € per unit, the requirement of installing one electronic device per module is not ideal, as it may increase the overall investment cost of a PV facility.
- Furthermore, the maximum EL and PL signals achievable are limited by weather conditions, mainly solar irradiance. The PL signal is directly proportional to irradiance, while the EL signal is directly proportional to the forward-bias current level, which in turn depends on irradiance, since string current is used for EL signal generation. Therefore, the proposed approach requires high irradiance levels to achieve optimal performance. However, this is not an issue compared to infrared thermography, as it also requires a threshold irradiance level for proper measurements.

Finally, it should be noted that the device currently enables square-wave modulation of the EL and PL signals. Nevertheless, arbitrary modulation of the luminescence signal can be achieved through small hardware and software modifications, specifically by incorporating an LC low-pass filter together with PWM control of the MOSFETs in the electronic device.

Chapter V

Luminescence Imaging Acquisition and Processing

The previous chapter presented an electronic device whose integration at the module level enables modulation of both EL and PL signals by changing the operating point of the module. This chapter discusses the acquisition process of the image sequence and its processing to extract the EL or PL signal from the background signal generated by sunlight. This is crucial since the device only operates during daytime, using the string current for EL modulation and sunlight for PL modulation.

First, the acquisition set-up where the technique was validated is described, including the characteristics of the PV system and the camera specifications. Regarding the processing of the image sequence, two approaches have been analysed. The first processes the images in the time-domain, with two different strategies proposed and evaluated (synchronous and asynchronous strategies). The second approach processes the image sequence in the frequency-domain using the Fast Fourier Transform (FFT), which allow extracting the EL signal when it is modulate with any periodic waveform.

5.1. Acquisition Set-up

All the measurements presented in this chapter were acquired using the setup shown in Figure 23. The electronic board is connected within the PV string and controlled wirelessly via the board's Bluetooth module. The control system is a laptop, which also operates an InGaAs camera (Hamamatsu C12741-03) via USB. The camera has a resolution of 640 × 512 pixels and a maximum frame rate of approximately 60 frames per second (fps). Specifically, the acquisition time is mainly determined by the sum of the selected exposure time and the camera's processing time, the latter being 16.7 ms. All camera parameters are collected in Table 5. The camera lens is equipped with a bandpass filter centred at 1,160 nm, with a bandwidth of 150 nm and a transmittance close to 90%.

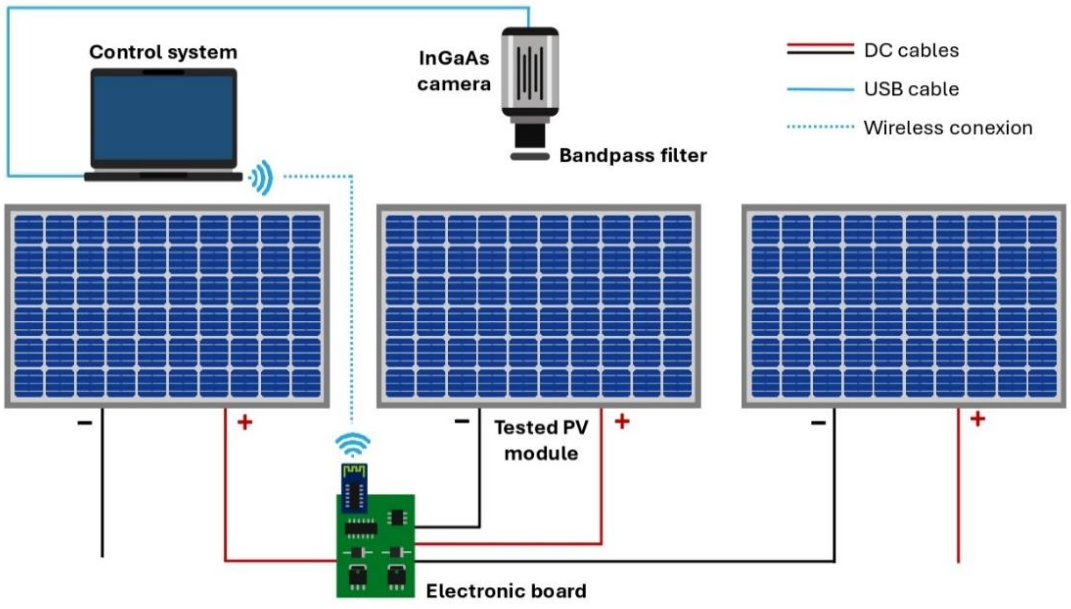

Figure 23. Acquisition setup of the developed EL and PL imaging technique. Reproduced from [101].

Table 5. Summary of SWIR camera specifications (Hamamatsu C12741-03).

Imaging device	InGaAs sensor
Effective number of pixels	540 (H) × 512 (V)
Pixel size	20 µm (H) × 20 µm (V)
Effective area	12.8 mm (H) × 10.24 mm (V)
Cooling method	Peltier cooling
Frame rate	59.774 frames/s
Digital output	14 bit
Maximum exposure time	1 s
Interface	USB 3.0
Less mount	C-mount
Power supply	DC +12 V
Power consumption	Approx. 18 W

Figure 24 displays the quantum efficiency of the InGaAs camera used, the normalized emission spectrum of crystalline silicon, the filter transmittance, and the reference solar spectrum. The optical filter blocks most wavelengths outside the luminescence spectrum. This, together with the reduced irradiance around 1,100 nm due to the absorption band of H_2O, leads to an increased ratio between the luminescence signal and the sunlight signal captured by the camera.

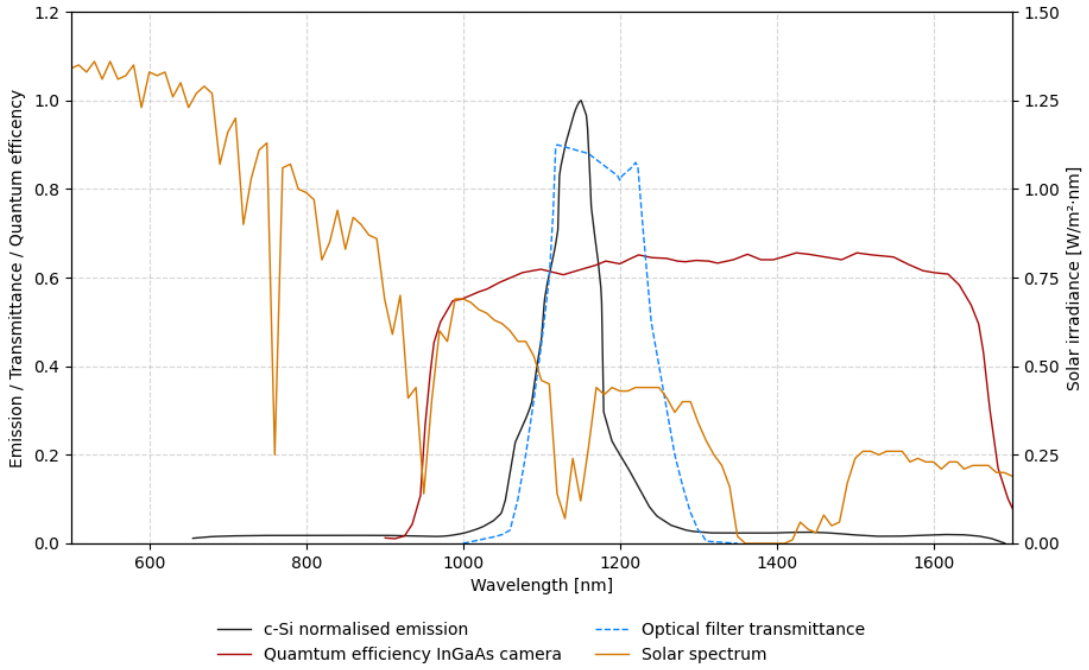

Figure 24. Quantum efficiency of InGaAs camera (Hamamatsu C12741-03), normalised spectrum of luminescence in crystalline silicon, optical filter transmittance and reference solar spectrum ASTM G173-03 [47].

Measurements were performed on a PV string composed of 10 multicrystalline silicon PV modules (Trina Solar TSM-235-PC05A), each with a maximum power of 235 W_p, a V_{OC} of 37.2 V, and an I_{SC} of 8.55 A under STC. All modules are connected to a string inverter (Sunny Boy SB1.5-1VL-40).

Note that these conditions represent the worst-case scenario due to two key factors. First, multicrystalline silicon modules have lower luminescence emission compared to other technologies such as monocrystalline silicon, PERC, or IBC modules (see Chapter II). The use of these other technologies should perform better because of the higher ratio between luminescence and background signal. Second, in a string configuration, changing the operating point of one module has a greater impact on the inverter's MPPT algorithm compared to a central inverter that tracks the MPP of hundreds of modules.

5.2. Time-domain Imaging Processing

Processing Method

Time-domain processing requires an image sequence in which the luminescence signal has been binary modulated, following a square waveform. Therefore, some images correspond to a high-emission state of the EL or PL signal, while others correspond to a low or null emission state of the EL or PL signal. To remove the background signal, for each pixel it is necessary to average all high-state values and all low-state values separately. The final value is then calculated by subtracting the average low-state value from the average high-state value. This calculation is shown in Equation (8), where:

- $R\,(x, y)$ is the value of pixel (x, y) in the resulting image
- $E_i\,(x, y)$ is the value of pixel (x, y) in the high-state image number i
- $B_j\,(x, y)$ is the value of pixel (x, y) in the low-state image number j
- N_E is the number of high-state images
- N_B is the number of low-state images

$$R(x,y) = \frac{1}{N_E}\sum_{i=1}^{N_E} E_i(x,y) - \frac{1}{N_B}\sum_{j=1}^{N_B} E_j(x,y) \tag{8}$$

Therefore, for time-domain processing, it is essential to know which images have been taken during high and low luminescence emission states of the PV module. This leads to the use of two different lock-in approaches, referred to as synchronous and asynchronous strategies.

The synchronous strategy involves continuous communication between the camera and the electronic device that modulates the luminescence signal through the control system. This allows the emission state of each image to be known and labelled during acquisition. The control system sends a command to the electronic board to set a new operating state. Once the board has set this operating point, it sends a confirmation back to the control system, which immediately triggers a shot on the InGaAs camera. After each picture is taken and labelled with its corresponding operating point, the control system sends another command to the electronic board to change its operating point. This process is repeated until the image sequence reaches the desired size. For synchronous acquisition, the camera must be configured in trigger mode. However, this configuration, along with the delays induced by communication between devices, may reduce the frame rate of the measurement.

The asynchronous strategy has been developed to avoid synchronization and continuous communication between the camera and the electronic device that modulates the luminescence signal. Before image acquisition begins, the electronic device receives a single command that causes it to modulate the EL or PL signal at a given frequency. The camera then captures images at its maximum speed until the sequence reaches the desired size, after which another command is sent to the electronic device to restore the module to normal operation.

As there is no synchronization between the camera and the electronic module, it is likely that some frames will be captured during the transition between operating points. To minimize this effect, it is recommended to reduce the modulation frequency so that more than two images are acquired per cycle. In the present setup, the modulation frequency was set to approximately six times the acquisition speed of the camera. This results in six images per cycle: three corresponding to the low state and three corresponding to the high state.

However, the asynchronous method results in an image sequence where the emission state of each picture is unknown. Therefore, it is necessary to implement an algorithm capable of classifying the images for further processing. A simple algorithm has been developed that classifies each picture based on its average intensity value, which is compared with those of the surrounding images. The performance of the algorithm is shown in Figure 25. It compares the average pixel value of the image to be classified with the average pixel value of the *n* nearest images in the sequence. The value of *n* should be adjusted for proper classification and is recommended to be close to the number of images captured per modulation cycle. In the present approach, *n* is set to 6.

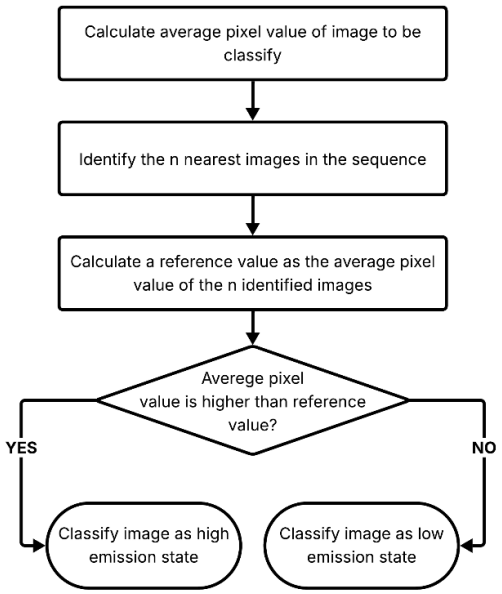

Figure 25. Developed algorithm to classify images under high or low luminance emission state in asynchronous lock-in strategy.

Note that all acquisition and processing were performed automatically by a Python script running on the laptop acting as the control system (Intel Core i7-11800H). The script sends commands to the electronic board via Bluetooth and controls the InGaAs camera through a dedicated control library. Moreover, the implemented algorithm, along with the calculations described in Equation (8), is executed by this Python script. The final image is also normalized for proper visualization, and the "magma" colour map is applied.

It is desirable to analyse image quality from a quantitative point of view, allowing comparisons of both synchronous and asynchronous lock-in strategies. The SNR metric adapted for daylight acquisition has been used [62]. The calculation of this metric must be performed following Equation (9). Where *k* denotes the pixel index. The total number of images in the stack is *2|N|* consisting of *N* images captured during high luminescence signal (denoted as L_i) and *N* images captured during low luminescence signal (denoted as BG_i). The set N_1 includes the odd-numbered images, while N_2 includes the even-numbered ones. An SNR value above 5 is generally considered indicative of good measurement quality. The implement python script is also able to calculate SNR during imaging processing.

$$\mathrm{SNR} = \frac{\sum_k \left(avg_{i \epsilon N} \left(L_i(k) - BG_i(k) \right) \right)}{\sum_k \left(\left| avg_{i \in N1}(L_i(k)) - avg_{j \in N2}\left(L_j(k)\right) \right| \cdot \sqrt{0.5} \cdot \left(\frac{2}{\pi}\right)^{-0.5} \right)} \tag{9}$$

Finally, it should be highlighted that for proper modulation of the EL and PL signal is necessary to change the operation point of the module.

- For EL modulation during daylight, it necessary to alternate between forward-bias current (EL + PL + background signal) and OC conditions (PL + Background signal). Thus, subtraction of images in both operating points enhance EL signal isolation. The use of OC instead of MPP is essential because, under forward-bias current and daylight conditions, the module emits both EL and PL signals simultaneously (see Figure 4), making it impossible to isolate the pure EL contribution. In contrast, OC operation allows capturing only the PL and background components, enabling a clean separation of the EL signal after image subtraction.
- For PL modulation during daylight, it necessary to alternate between OC conditions (PL + background signal) and MPP conditions (Background signal). Thus, subtraction of images in both operating points enhance PL signal isolation.

Results

Figure 26 shows two examples illustrating the evolution of average pixel intensity within a segment of 40 images. In the synchronous strategy, high and low luminescence signal images are acquired alternately, whereas in the asynchronous approach, approximately three images of the same emission state are captured consecutively, since the modulation frequency is about six times lower than the camera's acquisition speed.

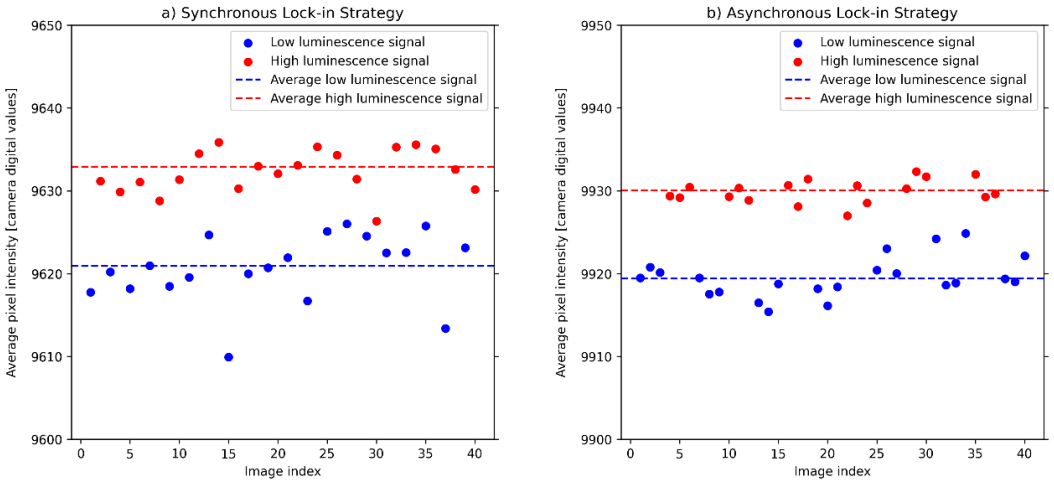

Figure 26. Comparison of the average pixel intensity within the synchronous (a) and asynchronous (b) image sequences in EL imaging acquisition.

In both approaches, the luminescence signal is low. The difference between the average high and low luminescence signals is around 10 digital values, compared to more than 9,500 values of background signal generated by sunlight. This corresponds to a luminescence-to-background ratio of about 0.1%. Such a low signal explains why minor changes in irradiance between the acquisition of consecutive images can affect the quality of the final signal. Moreover, this small signal may be of the same order of magnitude as the noise of the camera sensor. These factors together explain why a higher number of images is necessary to obtain a final picture of sufficient quality.

It is also possible to evaluate the performance of the proposed algorithm for automatic classification in the asynchronous strategy. For this purpose, an image sequence obtained with the synchronous approach is processed by the algorithm, enabling quantification of the number of classification errors. The algorithm correctly classifies more than 95% of the images. It should be noted that better performance is expected for higher ratios between luminescence and background signals, which can be achieved by using other silicon technologies such as PERC PV modules or by employing a filter with a narrower bandwidth.

During the measurement process, both EL and PL images were successfully obtained using synchronous and asynchronous strategies. The final EL or PL images, produced through appropriate calculations, normalization, and colour map application by the developed Python algorithm, are shown in Figure 27. All images were generated by processing an image stack of 1,000 frames acquired under high irradiance conditions (between 800 and 1,000 W/m^2) with an exposure time of 2 ms. Figure 27 also presents the calculated SNR, the camera acquisition speed, and the processing time.

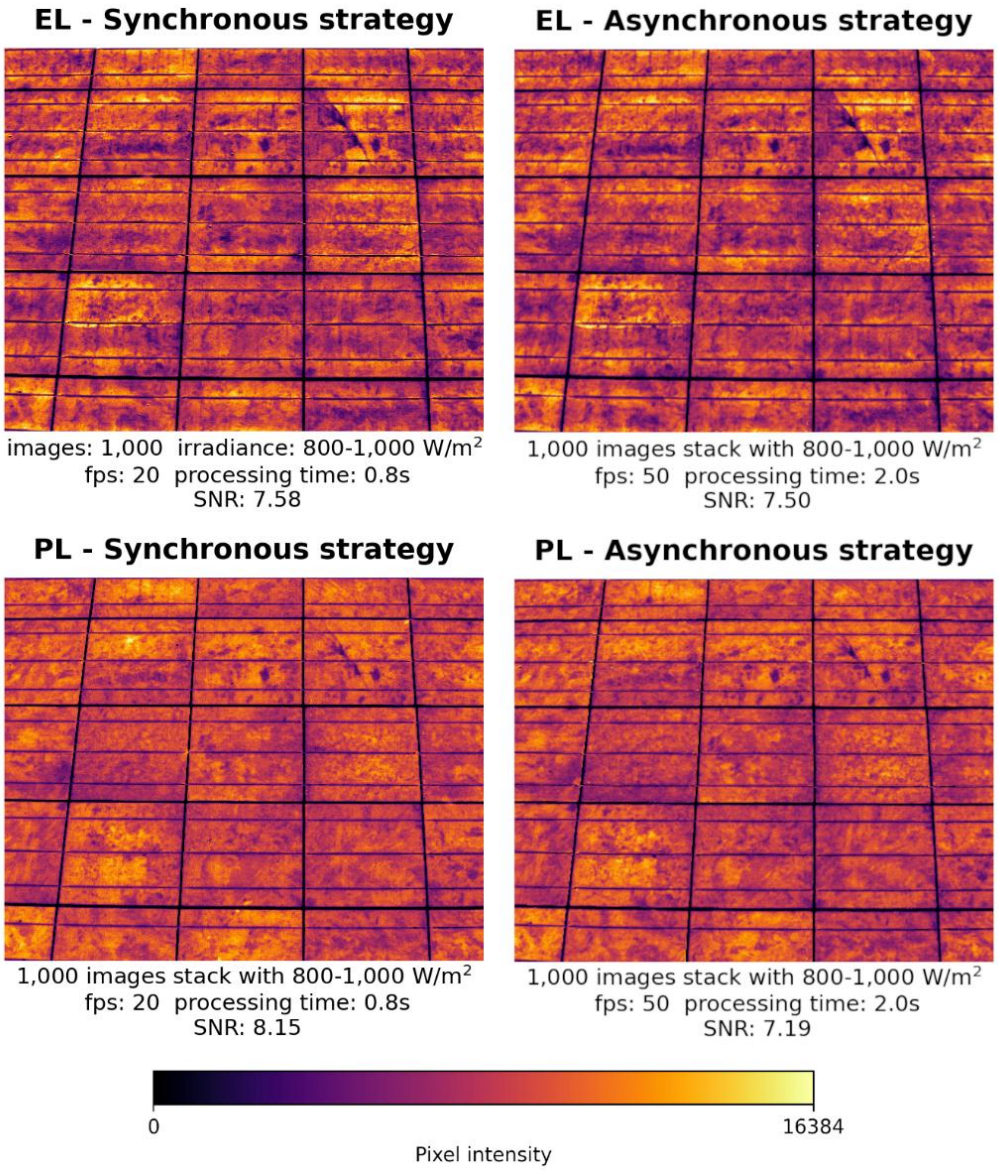

Figure 27. Comparison of EL and PL images obtained using synchronous and asynchronous strategies.

From a technical standpoint, the asynchronous strategy offers certain advantages over the synchronous approach. Since it does not require synchronization, separate control systems or software can be used for the device that modulates the signal and for the camera, eliminating the need to develop a single program capable of managing both simultaneously. Additionally, the camera can operate in continuous acquisition mode, allowing it to reach its maximum acquisition speed. In contrast, the synchronous method requires the use of trigger mode, which reduces the acquisition speed to 20 fps compared to 50 fps in continuous mode.

This reduction in acquisition speed is mainly due to the delay caused by continuous communication between the two devices, which depends on the hardware implementation. It should be noted that using alternative trigger strategies could increase the frame rate to values close to those of the asynchronous strategy. Since daylight EL and PL measurements typically require a large number of images, this difference in speed can be significant. For instance, capturing 1,000 images takes 50 seconds in synchronous mode but only 20 seconds in asynchronous mode.

Regarding the computational cost of both strategies, it should be noted that the synchronous approach requires less processing time. Processing 1,000 pictures with the synchronous method takes 0.8 s, whereas the asynchronous method requires up to 2.0 s due to the implementation of the classification algorithm. Note that this processing time depends linearly on the size of the image sequence.

Regarding the quality of the final picture, both EL and PL images exhibit similar SNR values. However, differences between EL and PL imaging can also be observed. In EL images, the signal is notably stronger near the metal contacts of the cell due to electrical excitation, whereas PL images exhibit a more uniform distribution of signal intensity, as the excitation source is sunlight, which is homogeneous across the entire cell surface.

It has also been observed that the synchronous strategy yields slightly better results in terms of SNR, although no visual differences can be detected between the synchronous and asynchronous methods. This slightly higher SNR may be explained by errors introduced by the algorithm, as well as by the fact that the high/low signal images are not directly acquired, which can increase the negative impact of changing irradiance.

Finally, it is possible to see in Figure 28 how SNR evolves with increasing number of images in the sequence. Although previous results have been by processing 1,000 of pictures, between 300 and 500 may be enough for achieving a SNR value higher than 5, which is considered a good value. It would allow to reduce the total acquisition time of the image sequence, which may be critical when inspections must be performed on thousands of modules. The increase in SNR with the size of the image stack is explained by the reduction of noise, as processing a larger number of images statistically reduces the random noise that appears in the image sequence.

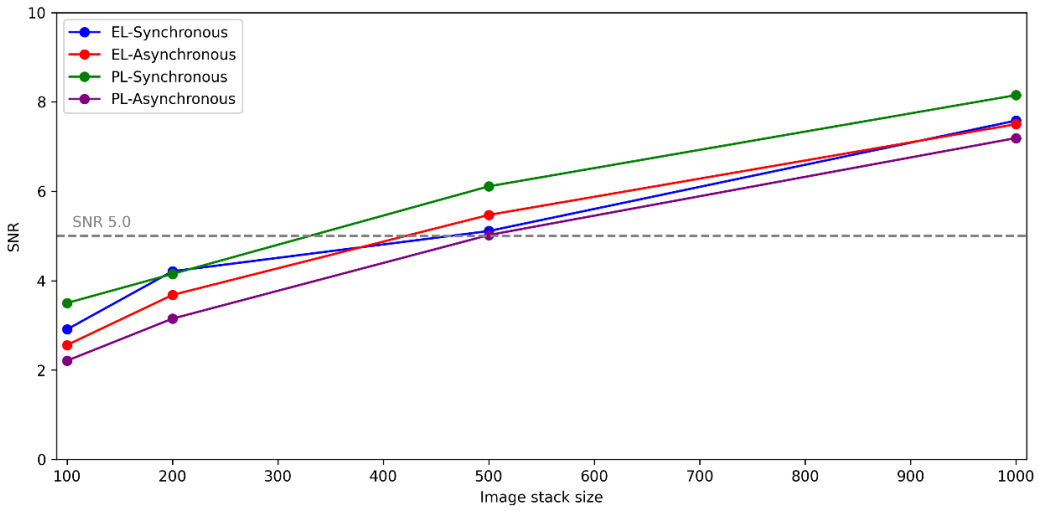

Figure 28. SNR dependence on image stack size for EL and PL using synchronous and asynchronous strategies.

5.3. Frequency-domain Imaging Processing

Processing Method

The obtained image sequence can also be processed in the frequency-domain. This means that an FFT is applied to the signal evolution of each pixel. The final pixel value in the resulting image corresponds to the amplitude of the FFT at the frequency index used to modulate the luminescence signal. To calculate this frequency index (*k*), it is necessary to know the frame rate of the image sequence (f_s), as well as the modulation frequency (f_k), which allow applying Equation (10). Where *N* is the size of the sequence.

$$k = \frac{N \cdot f_k}{f_s} \tag{10}$$

As previously explained, this method has only been validated for EL imaging, since the linear dependency between EL signal intensity and forward-bias current allows for a direct implementation. One advantage of frequency-domain processing is that the luminescence signal can be extracted by modulating it with any periodic waveform, whereas time-domain processing only works with square wave modulation.

In the present approach, the modified electronic board with a bandpass filter and PWM control was used to modulate the EL signal with three different waveforms (see Chapter IV): square, full sine, and half sine. This has allowed evaluating the potential differences between them. Furthermore, the EL signal has also been modulated using a power supply (EA ELEKTRO-AUTOMATIK EA-PSB 10200-25 2U 1500W), which has been properly programmed to reproduce the aforementioned waveforms.

It is also possible to use an SNR metric to perform quantitative analysis of resulting pictures. SNR for frequency-domain processing can be calculated by using Equation (11) [102].

$$\mathrm{SNR} = 10\log_{10}\left(\frac{\mathrm{Peak\ amplitude}^2}{\mathrm{Var(Noise)}}\right) \tag{11}$$

The peak amplitude is defined as the difference between the amplitude at the modulation frequency (f) and the average amplitude within the frequency range [f/2, 2f], excluding the modulation frequency itself. Noise is estimated as the variance of the amplitude within the same frequency range, also excluding the modulation frequency. To calculate the SNR for the entire image, the SNR values of the pixels corresponding to the photovoltaic module area are averaged, ensuring that signal variations in irrelevant pixels are not considered. In this SNR method, a value above 10 dB is considered indicative of sufficiently high image quality.

For this method, another Python script was developed to perform an FFT on each pixel after acquiring the image sequence. The script was executed on the laptop serving as the control system (Intel Core i7-11800H). The script also normalizes the final image, applies cropping and perspective correction based on corner detection of the module, applies the “magma” colour map, and calculates the SNR for the pixels corresponding to the module area. The general flow diagram of the frequency-domain approach is shown in Figure 29.

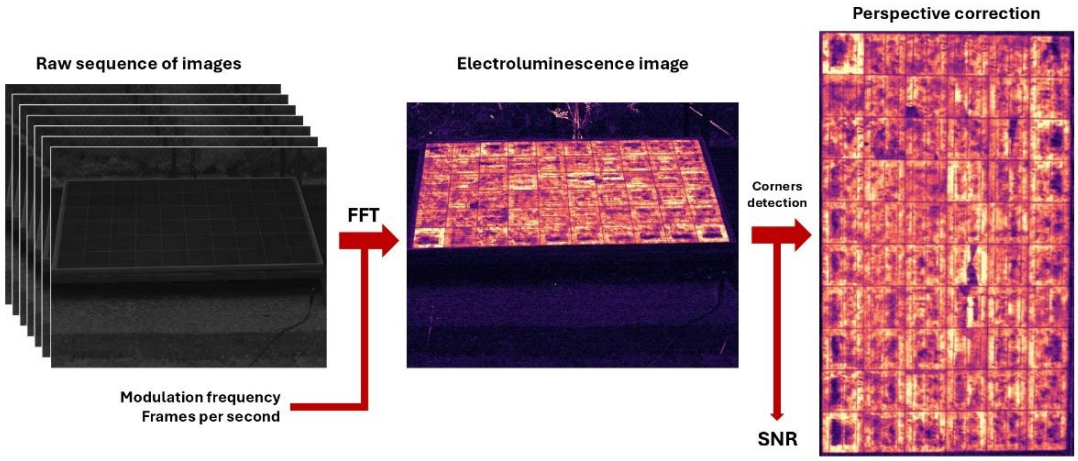

Figure 29. Frequency-domain processing approach flow diagram. Reproduced from [101].

In this approach, all image sequences consist of 1,000 pictures, captured with an exposure time of 2 ms, an acquisition speed of 53 fps, and a modulation frequency of 4 Hz. The chosen modulation frequency of 4 Hz, combined with the acquisition speed of 53 fps, results in approximately 13 measurements per modulation cycle, allowing for an accurate representation of the modulated waveforms.

Results

Figure 30 represents the signal evolution of three different 1,000 image sequences where the EL signal has been modulated following square, full sine and half sine wave modulation as Figure 22 shows. Here it is possible to check that signal captured by the camera reproduced the waveform of the forward-bias current in the PV module. Again, luminescence signal is low, which accounts with around 20 digital values against 12,000 digital values of the background signal generated by sunlight, which means a ratio between luminescence and background signal around 0.17%. It is also possible to see in Figure 30 that background signal changes during image sequence acquisition due to changing irradiance. Even on clear-sky days with apparent constant irradiance, minor irradiance changes during the acquisition of the images could have a greater impact on signal captured by the camera than the luminescence signal itself.

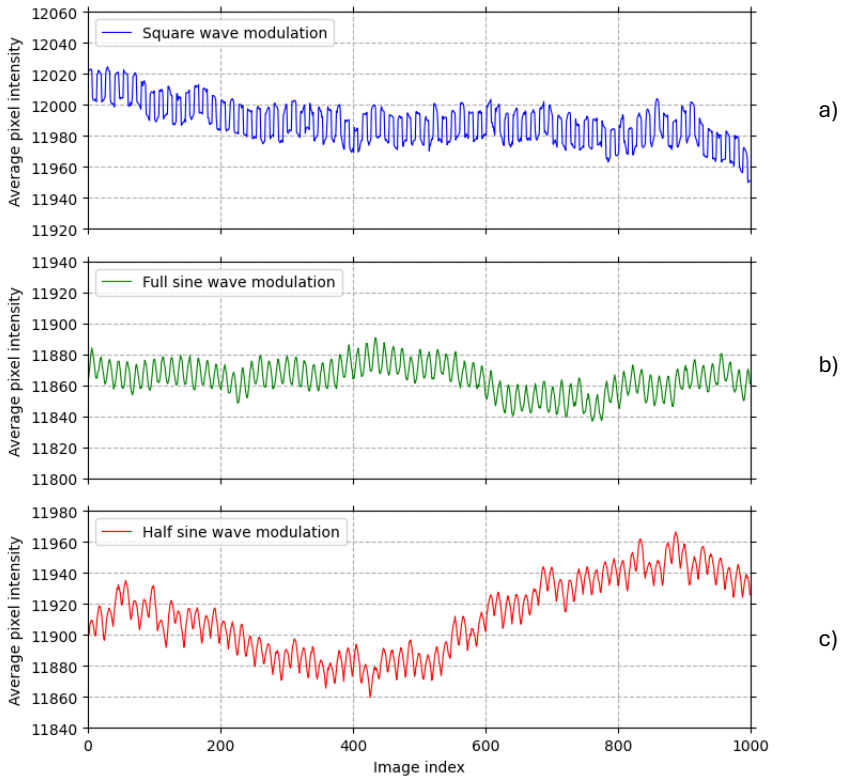

Figure 30. Average pixel value evolution in image sequences obtained during EL modulation with square (top), full sine (middle) and half sine (bottom) modulation Reproduced from [101].

As an example, Figure 31 shows the FFT of the average pixel value across a sequence of 1,000 images, where the EL signal was modulated using a 4 Hz square waveform and captured at an acquisition speed of 53 fps. As expected, there is an amplitude peak at the frequency index corresponding to 4 Hz, indicating signal transmission at this frequency and thus the presence of the EL signal. The FFT must be applied to each pixel of the image, with the amplitude at this frequency index providing the pixel value for the final EL image.

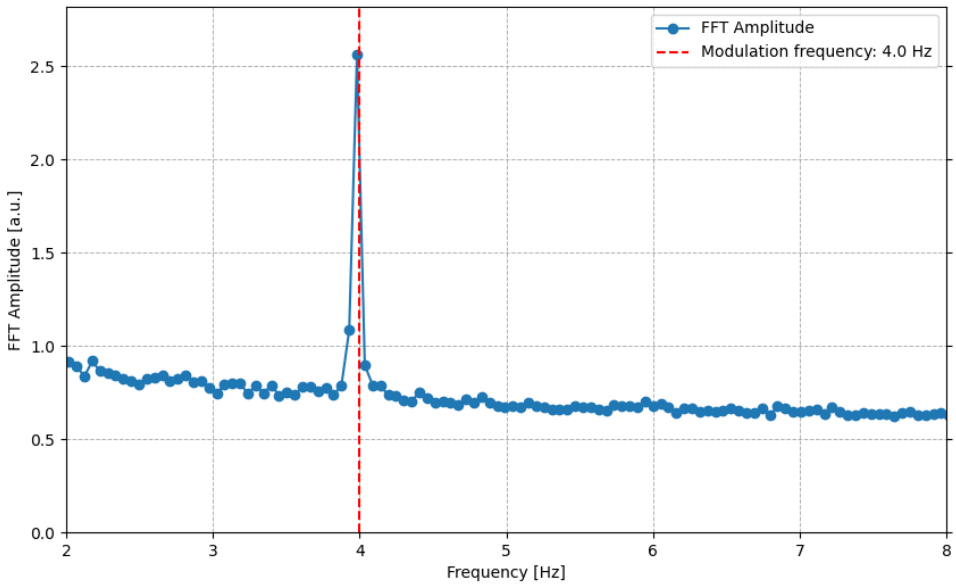

Figure 31. Average FFT transformation for a sequence of 1000 images captured at 53 fps with a 4 Hz modulation frequency using a square wave. Reproduced from [101].

Measurements were first taken using the programmable power supply, each delivering a peak amplitude of 8 A for the different waveforms. Figure 32 shows images processed in the frequency-domain for the three mentioned waveforms. The figure also includes the average irradiance during image capture, along with the corresponding SNR values. All cases yielded good SNR values (>10 dB), and no visual differences could be detected between them. However, square-wave modulation exhibited a slightly higher SNR, followed by full-sine-wave modulation.

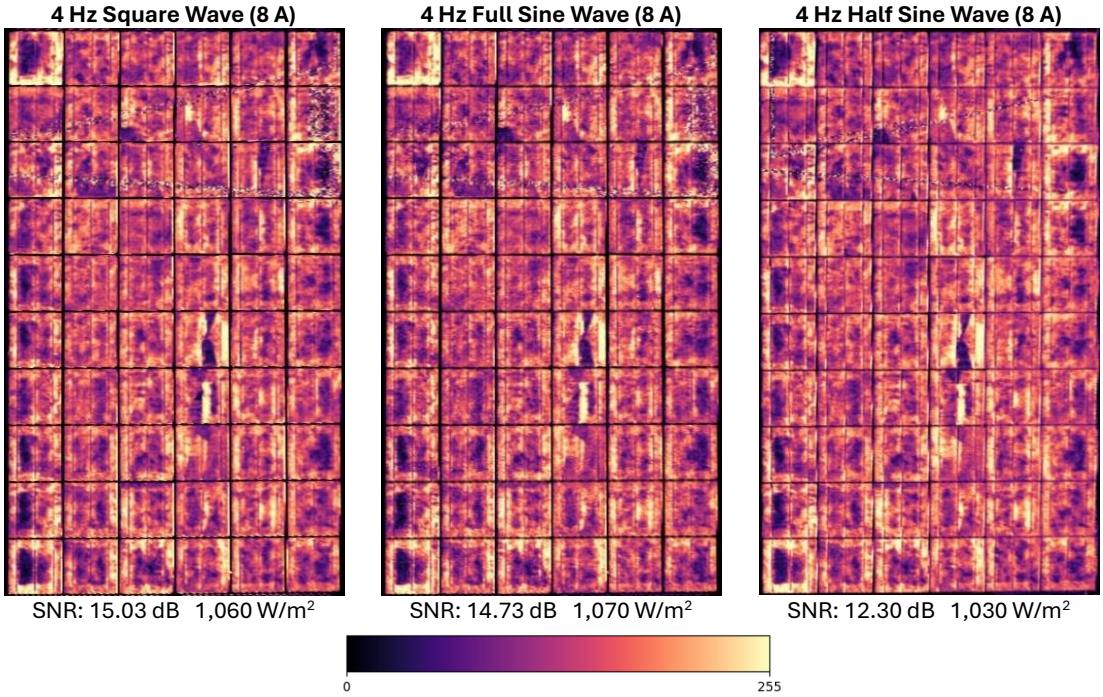

Figure 32. EL images obtained via power supply modulation using different waveforms. Exposure time of 2 ms, captured at 53 fps, with 1,000 images per sequence. Reproduced from [101].

Measurements were also performed using the modified electronic board for EL signal modulation. Figure 33 shows the final EL images for the different waveforms modulated via the modified electronic device, together with the average irradiance level during acquisition and the calculated SNR. Similar images, without appreciable differences, were obtained compared to the power supply approach. Moreover, the SNR values are comparable to those obtained with the power supply. Once again, it is worth noting that square-wave modulation yielded the highest SNR, although no visual differences were observed among the different waveforms.

Moreover, detailed images of specific solar cells in the module are shown in Figure 34, where anomalies such as cracks or inactive areas can be easily detected. The first row includes some cracks within the solar cells that led to isolated areas; the second row shows a solar cell with an inactive area in one corner, and the third row presents solar cells with clearly inhomogeneous signal distribution across their areas. The SNR analysis again identifies square-wave modulation as the waveform with the best performance, although all waveforms produced images without apparent visual differences.

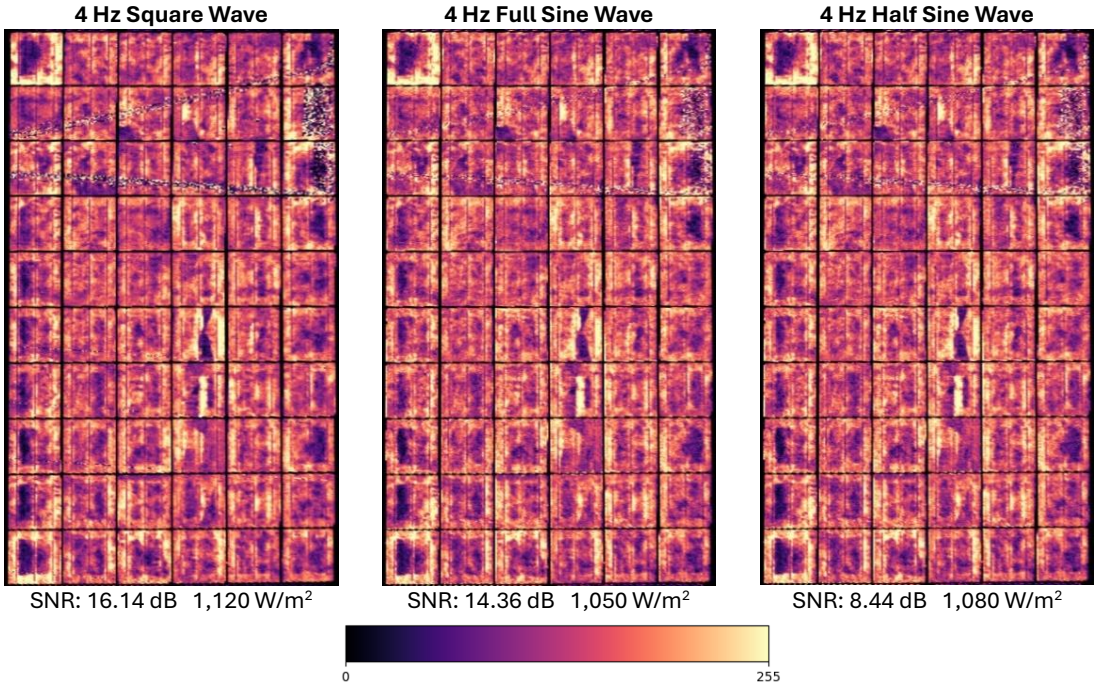

Figure 33. EL images obtained via electronic device modulation using different waveforms. Exposure time of 2 ms, captured at 53 fps, with 1,000 images per sequence. Reproduced from [101].

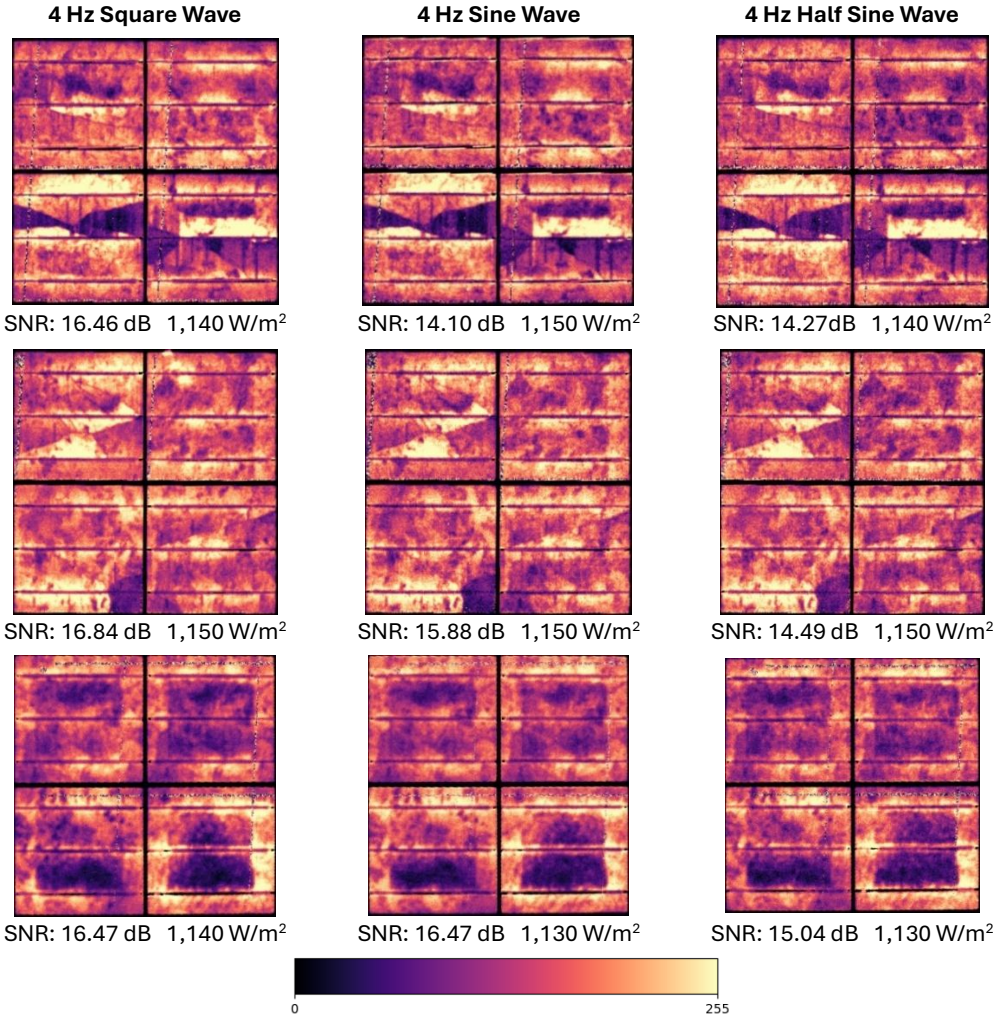

Figure 34. Detailed EL images obtained via electronic device modulation using different waveforms. Exposure time of 2 ms, captured at 53 fps, with 1,000 images per sequence. Reproduced from [101].

Regarding the computational cost of the frequency-domain processing method, a total of 6.5 s has been reported for performing processing on 1,000 image sequence of 640 × 512 pixels on an Intel Core i7-11800H processor. It should be noted that most of the processing time corresponds to applied FFT to all pixels within the sequence, which allows to estimate the computational cost as Equation (12) shows.

$$\mathrm{t(N,p)} = c \cdot p \cdot N log_2 N \tag{12}$$

Here, *t (N, p)* denotes the processing time as a function of the number of images to be processed (*N*) and the number of pixels per image (*p*), while *c* is a constant determined by the specific FFT implementation and the hardware specifications. In the present experiments, using the mentioned processor and a Python script with the NumPy library for FFT computation, the constant *c* was found to be $2 \cdot 10^{-9}$ s·pixel^{-1}.

Since the computational cost of the FFT does not scale linearly with the number of samples, applying this method to half of the images would reduce the processing time by more than 50%, resulting in approximately 2.9 s. Similarly, performing the algorithm on sequences of 200 and 100 images would further decrease the processing time to 0.99 s and 0.43 s, respectively.

5.4. Discussion

This chapter has explored different lock-in imaging processing approaches for extracting the luminescence signal from an image sequence in which the signal has been modulated. Two main approaches have been successfully validated.

The simplest approach is based on processing in the time-domain. This method requires square-wave modulation of the EL or PL signal, which results in some images in the sequence capture both luminescence and background signals, while others capture only the background signal generated by sunlight. By averaging these two groups of images separately and performing a subsequent subtraction, it is possible to isolate the luminescence signal, producing images that can be used for fault detection and PV module performance analysis. Moreover, this time-domain processing technique has been validated using two different strategies: synchronous and asynchronous.

The synchronous strategy is based on synchronization and continuous communication between the electronic device modulating the EL or PL signal and the InGaAs camera capturing the images. This allows the images to be labelled according to their luminescence emission state (high or low), facilitating the direct calculation of the final image. In contrast, the asynchronous approach lacks coordination between the camera and the electronic device, so an algorithm has been developed to automatically classify the images in the sequence, enabling subsequent calculations with the pictures.

Both approaches have successfully produced EL and PL images with acceptable SNR values. Although no visual differences were observed between the two strategies, the synchronous approach provides slightly higher SNR, likely due to errors in the automatic classification algorithm, which have been quantified at around 5%. However, the asynchronous approach offers several practical advantages. First, its implementation is much simpler, as there is no need to develop dedicated software to control both the camera and the electronic device. Moreover, synchronization may be difficult to achieve in certain setups, for example, when drones equipped with InGaAs cameras are used for EL or PL

imaging. Finally, the asynchronous approach allows the camera's acquisition speed to be maximized, whereas the synchronous strategy may introduce delays due to continuous communication and the need to configure the camera in trigger mode. Since multiple images are required to achieve good SNR, acquisition speed can be critical when imaging thousands of modules.

A more complex approach based on frequency-domain processing has also been validated. It allows the isolation of the luminescence signal when it has been modulated using any periodic waveform. The method is based on applying an FFT to each pixel across the image sequence, with the luminescence signal obtained from the amplitude of the FFT at the frequency index corresponding to the modulation frequency. This method has been validated only for EL imaging, as arbitrary EL signal modulation is simpler and more straightforward to implement compared to PL modulation.

Modulation using the developed electronic device, with some modifications, combined with frequency-domain processing, has produced EL images similar to those obtained using the same processing method but with a power supply as the excitation source. No visual differences are observed, and comparable SNR values are achieved. Three different EL modulation waveforms were tested, all of them providing sufficiently high SNR in most scenarios. Nevertheless, square-wave modulation exhibited slightly better SNR, although minor visual differences can be detected between the final images obtained with different modulation waveforms.

The potential adverse effects of the FFT, such as spectral leakage or the "picket fence" effect, were not specifically evaluated, as satisfactory results were obtained without applying mitigation techniques. However, a slight improvement in SNR could be expected if such corrective measures were implemented.

The comparison between time-domain and frequency-domain processing methods is not straightforward. It can only be stated that both methods are capable of achieving acceptable SNR values with the same number of images in the sequence under similar conditions. In terms of qualitative image quality, similar results are obtained, although quantitative analysis is more complex since SNR must be calculated differently for each method. It should be noted that time-domain processing is easier to implement, especially in the asynchronous strategy. Furthermore, processing time is significantly lower with time-domain processing, particularly when the number of images in the sequence is high. One advantage of the frequency-domain approach is that the luminescence signal can be modulated using any waveform, which can be useful for modulation methods with slower responses, such as when an inverter is used for PL modulation.

Finally, it should be noted that the measurements were performed on polycrystalline PV modules, which exhibit lower luminescence emission compared to other technologies, such as monocrystalline or PERC modules. Therefore, applying this technique to other technologies such as PERC or IBC is expected to yield better results, as a lower number of images would be required to achieve good SNR values due to the higher luminescence-to-background signal ratio. Another way to reduce the number of images needed could be the implementation of an optical bandpass filter with a narrower bandwidth.

Chapter VI

Integration of Non-Invasive PL and I-V tracing Functionalities into a Module-Level PV Optimizer

The developed EL and PL imaging technique, based on module-level electronics, presents a main limitation: it requires the permanent installation of module-level electronics on all PV modules in the power plant, which can significantly increase the investment cost. Considering that, in recent years, the use of module-level power electronics (MLPE), such as solar optimizers or microinverters, has become widespread with several commercial solutions available on the market [57], the integration of non-invasive PV module inspection techniques into the architecture of these devices shows great potential. Previous work based on module-level electronics has demonstrated that I-V curves can be traced without disconnections [103–105], making I-V tracing a non-invasive method.

The present chapter demonstrates how non-invasive luminescence signal modulation and I-V tracing have been integrated into the power architecture of a PV solar optimizer. This represents a significant novelty that has not been reported previously in the literature. This integration results in a powerful module-level electronic device with multiple functionalities, making it more attractive from an economic perspective. These functionalities include MPPT, non-invasive I-V tracing, non-invasive luminescence signal modulation, active or passive bypass of the module, and electrical monitoring of the PV module output. The first section of the chapter presents the desirable requirements for the PV optimizer, followed by the chosen power topology and the minor software and hardware modifications required to integrate non-invasive I-V tracing and luminescence signal modulation. Finally, luminescence images captured under high irradiance conditions and I-V curves obtained using this device are presented.

6.1. Requirements of the Module-level PV Optimizer

Since module-level PV optimizers are installed permanently within a PV string, the following requirements are desirable.

1. **Simple topology**: the circuit topology must be as simple as possible. Since module-level integration requires low-cost and compact solutions, minimizing circuit complexity is essential for practical implementation.
2. **Direct integration of non-invasive measurements**: it is desirable that the integration of non-invasive I-V tracing and luminescence signal modulation does not require major changes in the device, especially in its hardware. It was observed that PL modulation allows for direct integration, whereas EL modulation requires an additional power stage, increasing the number of components, cost, and complexity of the device. Therefore, only PL signal modulation will be integrated into the electronic device, prioritizing simplicity and ease of integration over EL modulation.

3. **High efficiency**: as module-level PV optimizers perform MPPT, it is crucial that the integrated converter has a high efficiency. Current peak efficiency in module level-PV optimizers market is around 98-99% [57].
4. **Self-Powered Operation**: the electronic PV optimizer should function without a battery or external power source. Ideally, it should include a system to power the electronics using the energy generated by the PV module itself.
5. **External Control Interface**: the device must include a communication system that allows external control and configuration of PV optimizer.

6.2. Module-level PV Optimizer Design

Topology Selection

Several power topologies can be used to implement MPPT in a module-level PV optimizer [57]. Most commonly, non-isolated DC-DC converters, such as buck [106,107] and boost [108,109] converters, especially in their synchronous configurations to improve efficiency, are employed. Nevertheless, other power architectures, including SEPIC [110], Ćuk [111], and Flyback [112], among others, can also be used depending on the application.

In order to select a suitable topology, synchronous buck and boost converters were analysed due to their simplicity and high efficiency, two critical parameters in the design of MLPE for PV applications. Although the boost converter could offer advantages, as boosting the voltage reduces output current and consequently Joule losses, integrating I-V curve tracing and PL modulation is more challenging and requires additional hardware. First, it is not possible to establish open-circuit conditions without incorporating extra switches in the boost topology. Second, the potential I-V curve sweeps achievable using the boost converter's input inductor is significantly faster than the sweep obtained with the input capacitor of a buck converter. Therefore, the buck converter allows for the use of a simpler microcontroller with a lower sampling rate in its analog-to-digital converter (ADC).

The implemented power architecture, based on a synchronous buck converter, is shown in Figure 35. For a detailed explanation of its performance, see Chapter II. The input of the buck converter is connected to the PV module to be optimized, while the output terminals are connected to the positive and negative terminals of the adjacent modules in the string. The PV optimizer also includes voltage and current sensing at its input, as well as a half-bridge gate driver that enables fast switching of both MOSFETs (M_1 and M_2).

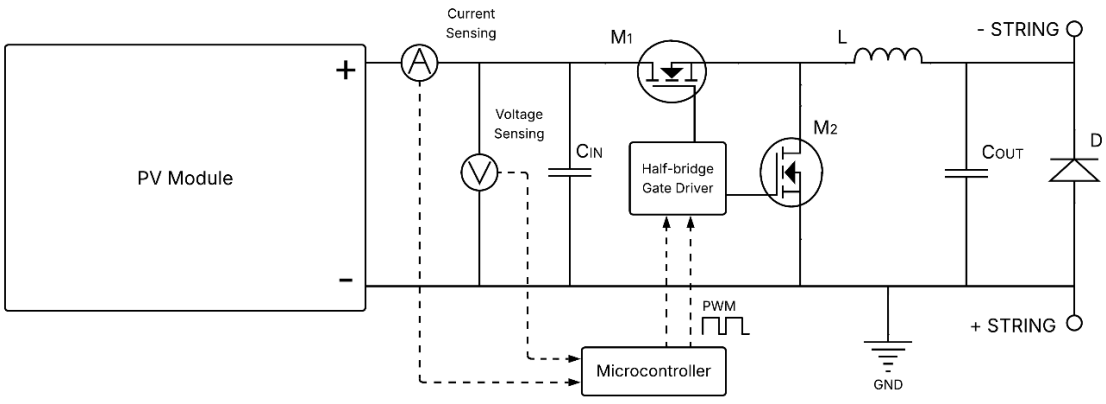

Figure 35. Implemented synchronous buck topology for the module-level PV optimizer.

MMPT Concept

To understand how the PV optimizer performs MPPT, a typical illuminated I-V curve is shown in Figure 36. In a synchronous buck converter, the low-side (M_2) and high-side (M_1) MOSFETs operate synchronously, meaning that when one is on, the other is off, and vice versa, preventing a short circuit in the half-bridge. The converter is controlled by a parameter known as the duty cycle (*d*), which is defined as the ratio of the time the high-side MOSFET (M_1) is on during one cycle to the total period of the cycle.

If the duty cycle (*d*) is 0%, the high-side MOSFET (M_1) is permanently off, and the low-side MOSFET (M_2) is permanently on. Analysing Figure 35, it can be deduced that, in this stationary state, the module operates under OC conditions, as no current is extracted from the module. In contrast, if the duty cycle (*d*) is 100%, the high-side MOSFET (M_1) is permanently on, while the low-side MOSFET (M_2) is permanently off. In this case, under stationary conditions, the PV module is directly connected to the converter's load output. If the load is a static impedance (Z_{OUT}), the module's operating point will be set at the intersection of the I-V curve and the load line defined by the inverse of the output impedance. If the load is the PV string, the module will operate at the point corresponding to the common current in the string.

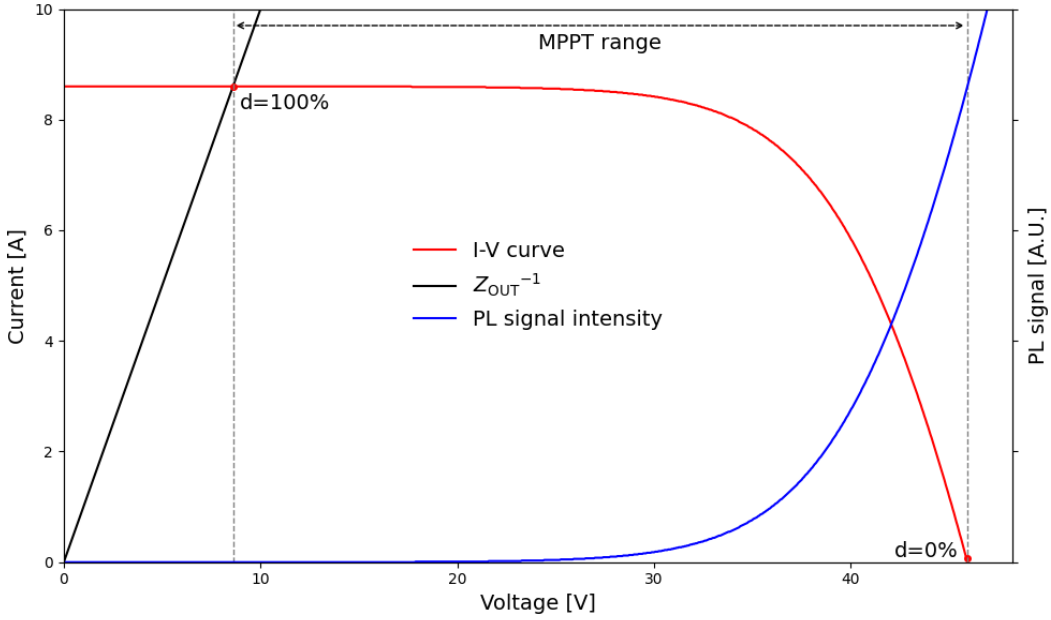

Figure 36. Typical illuminated I–V curve of a PV module, PL signal intensity as a function of operating voltage, and MPPT range of the optimizer.

Since the duty cycle can be dynamically adjusted by the microcontroller of the PV optimizer, it is possible to operate at any point from OC conditions to the point corresponding to the current demanded by the load, generating an MPPT range within which the module operating point can be adjusted. This also enables the implementation of an MPPT algorithm that dynamically changes the duty cycle and performs power measurements based on input current and voltage sensing, allowing operation at the MPP even as the I-V curve varies due to changes in irradiance, temperature, shading, and other factors.

There are many MPPT algorithms that can be implemented [55,56]. In the present device, the perturb and observe (P&O) algorithm has been implemented, which is a common classical MPPT algorithm. It is based on tracking the maximum power point by periodically perturbing the operating voltage or current and observing the resulting change in power, adjusting the operating point toward higher power. The block diagram of this algorithm can be seen in Figure 37.

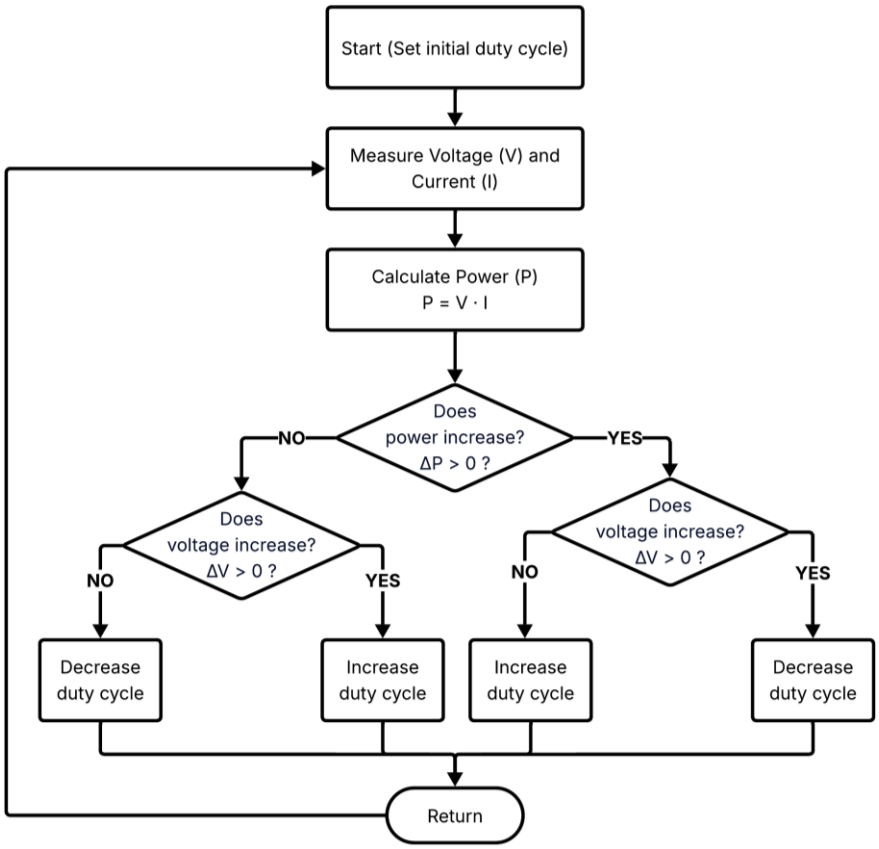

Figure 37.Flowchart of the implemented P&O algorithm for MPPT in a synchronous buck converter.

Photoluminescence Modulation Concept

The modulation of the PL signal does not require additional hardware compared to the standard topology of a module-level PV optimizer. PL modulation is achieved through the firmware of the PV optimizer's microcontroller by periodically changing the duty cycle. Figure 36 also shows the PL signal intensity as a function of the operating voltage. When the duty cycle is 0% and the module operates under OC conditions, the PL signal intensity is at its maximum. Conversely, a high duty cycle causes the module to operate at a high current level, where the PL signal intensity is low. Therefore, it is possible to modulate the PL signal simply by adjusting the converter's duty cycle.

I-V Tracing Concept

There are several methods available for performing I-V tracing in a PV device [40]. In the present approach, a technique known as capacitive sweep has been implemented. This technique is based on charging a capacitor from SC to OC conditions. During this transient, multiple current and voltage samples are taken, allowing the reproduction of the module's I-V curve. Figure 38 displays current and voltage evolution while a PV module is charging a capacitor from SC to OC, as well as the reconstructed I-V curve.

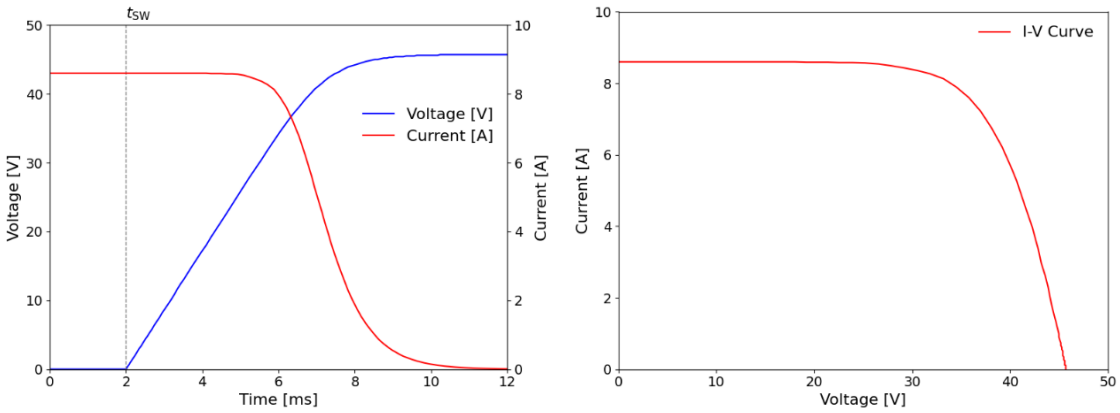

Figure 38. Voltage and current evolution during the charging of a 1,000 µF capacitor with a single PV module (a) and reconstructed I–V curve (b). Module characteristics in Table 3 and irradiance of 1,000 W/m². Data simulated with LTspice.

To implement this technique, several hardware components are required. However, all the necessary elements are already present in the architecture of a PV optimizer based on a synchronous buck converter:

- Capacitor: A capacitor connected in parallel with the PV module is required. In this case, the converter's input capacitor (C_{IN}) fulfils this function.
- Switching element: a device is needed to set the PV module to OC and SC conditions. Here, both the low-side and high-side MOSFETs perform this role. When both MOSFETs (M_1 and M_2) conduct simultaneously, the half-bridge is short-circuited, as is the PV module. Moreover, when the high-side MOSFET is off, module work in OC.
- Voltage and current sensing: Measurement of voltage and current in the module is required. The PV optimizer already includes voltage and current sensing at its input.

No modifications to the power topology are required to perform I-V tracing using the topology of a synchronous buck converter. However, some considerations must be taken into account regarding the supply and control system of the board.

During the tracing of the I-V curve, the module operates under SC conditions. As no voltage is provided by the module during this short period of time, if a voltage regulator is used directly to supply the microcontroller, sensors, communications module, or half-bridge driver, it may fail to provide an adequate voltage level for the operation of all the systems, potentially causing malfunctions or a microcontroller reset. To avoid this problem, the supply system shown in Figure 39 has been implemented.

The key components of the system are the diodes (D_{SC}) and the capacitor (C_{SC}). C_{SC} is charged to the module voltage during normal operation. During the portion of the I-V sweep when the module voltage is insufficient to power the supply system, C_{SC} provides an appropriate voltage level, as it does not discharge thanks to the presence of the D_{SC}. The supply system is directly connected to the positive and negative terminals of the module, and two voltage regulators are used: one to generate a higher fixed voltage (e.g., 10 V) to supply the half-bridge driver, and another to generate a lower fixed voltage (e.g., 5 V) to power the microcontroller, sensors, and communications module.

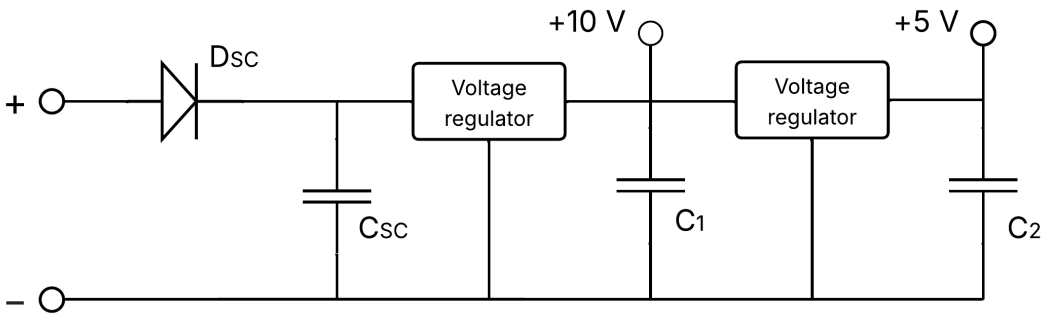

Figure 39. Schematic of the voltage supply system in the PV optimizer.

Another important aspect to consider is the control system of the half-bridge. The use of a half-bridge gate driver provides two main benefits. First, it enables the generation of an appropriate voltage level for switching the high-side MOSFET, whose source is floating. Second, it can source and sink large gate currents to both MOSFETs, allowing fast switching. Fast switching is crucial for achieving high efficiency, especially when the converter operates at high switching frequencies.

If the half-bridge gate driver is directly used to switch on both MOSFETs to achieve a short circuit in the half-bridge, fast switching can cause an abrupt discharge of the converter's input capacitor, generating a high current peak that may damage the MOSFETs. Therefore, a modification of the conventional half-bridge driver circuit has been implemented, as shown in Figure 40. The control schematic includes the conventional components along with an additional MOSFET, resistor, and capacitor (M_{AUX}, R_{AUX}, and C_{AUX}). The auxiliary MOSFET is driven by one of the microcontroller's output pins, preferably an analog output pin.

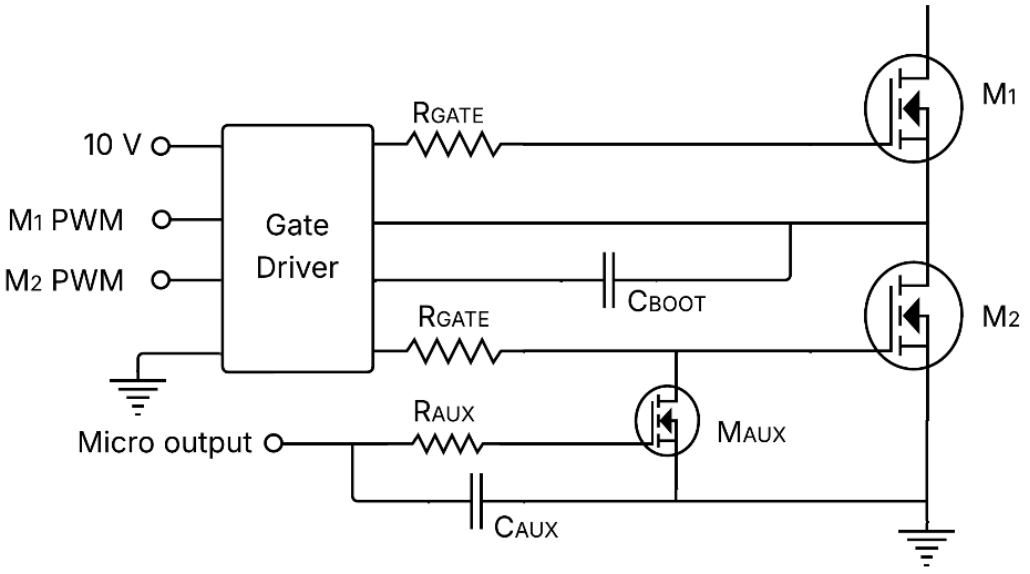

Figure 40. Conventional half-bridge driving circuit modified to allow both fast and slow switching of the low-side MOSFET.

When the PV optimizer is operating as a converter performing MPPT, M_{AUX} is turned off, allowing fast switching of both MOSFETs. However, when it is necessary to perform a soft short circuit of the half-bridge for I-V tracing, the following sequence is executed:

1. The duty cycle is set to 0%, so the module operates in OC and does not produce power.
2. Both PWM inputs of the driver are set to a low logic level, causing both MOSFETs to be off. In this state, the module is bypassed and the current flows through the bypass diode (D) of the PV optimizer.
3. The analog output controlling M_{AUX} is set to a high voltage level for proper switching of M_{AUX} (e.g., 5 V). As M_{AUX} turns on, the gate of the low-side MOSFET is referenced to ground.
4. Both PWM inputs of the driver are set to a high logic level, causing the high-side MOSFET to turn on. However, the low-side MOSFET cannot be switched on because its gate is still referenced to ground.
5. A decreasing voltage ramp is programmed on the analog output controlling the gate of M_{AUX}. This voltage ramp, together with R_{AUX} and C_{AUX}, results in the slow switching of M_{AUX}. Therefore, the gate voltage of the low-side MOSFET gradually rises from 0 V to the driver output voltage, enabling slow charging of the low-side gate and slow switching. This soft switching allows the input capacitor to discharge over a longer period, reducing the current peak to values the MOSFETs can safely handle.
6. Once the voltage ramp in the analog output controlling M_{AUX} is completed, the voltage sensor starts taking consecutive measurements until the voltage reaches 0 V, indicating that the input capacitor is fully discharged and the module is under SC conditions.
7. After reaching SC, both PWM inputs of the driver are set to a low logic level, causing both MOSFETs to turn off. At this point, the module transitions from SC to OC as the input capacitor charges, while voltage and current measurements are taken alternately.

Implementation

The presented circuitry has been implemented on a double-layer PCB based on the PIC18F26K83 microcontroller, whose full schematic can be seen in Annex I. Regarding the sensing system, analog Hall-effect current sensors are used at both the input and output of the board, while voltage sensing at the input and output is achieved through voltage dividers. The analog outputs of the current and voltage sensors are converted to digital values by the microcontroller's internal ADC, which can reach a maximum sampling rate of 90 kHz.

The half-bridge is composed of BUK9Y4R8-60E,115 MOSFETs driven by an NGD4300 gate driver operating at 100 kHz. For the input capacitance, a combination of ceramic and electrolytic capacitors is used to achieve a good balance between low series resistance and high capacitance. The total input capacitance is approximately 306 µF, resulting in a transient period from SC to open circuit OC of 1–5 ms, depending on the irradiance level and the electrical characteristics of the module. This transient time, together with the 90 kHz sampling rate of the ADC, allows the I–V curve to be captured with sufficient point density for accurate reconstruction.

The LC filter consists of a 40 µH power inductor and 456 µF of capacitance, also implemented with a mix of ceramic and electrolytic capacitors. This configuration provides a low-pass filter with a cutoff frequency of 1.18 kHz, effectively attenuating the 100 kHz switching ripple generated by the half-bridge.

The supply system is based on two voltage regulators. The first is a switching voltage regulator used to supply both the gate driver and the second voltage regulator. Given the significant voltage drop from the input level (30–40 V) to the driver supply voltage (10 V), a switching regulator is preferred, as it typically achieves efficiencies above 85%. In contrast, a linear regulator's efficiency can be approximated by the ratio of output to input voltage, which in this case would be around 25–35%.

The second voltage regulator is linear. Since the voltage drop between its input and output is smaller, its efficiency is higher. Furthermore, the linear regulator delivers a stable output voltage with minimal ripple, which is desirable for the proper operation of the microcontroller, particularly for ensuring precise ADC measurements. This supply configuration achieves a balance between high efficiency, which minimizes standby power consumption, and a stable voltage source that can serve as a reference for accurate ADC measurements.

The board has a compact size of 100 × 76 mm, making it suitable for module-level integration. Top and bottom views of the board, along with the assembled version, are shown in Figure 41. The board also includes two headers: one for in-circuit programming and another for connecting a Bluetooth module (HC-06) for external control and communications.

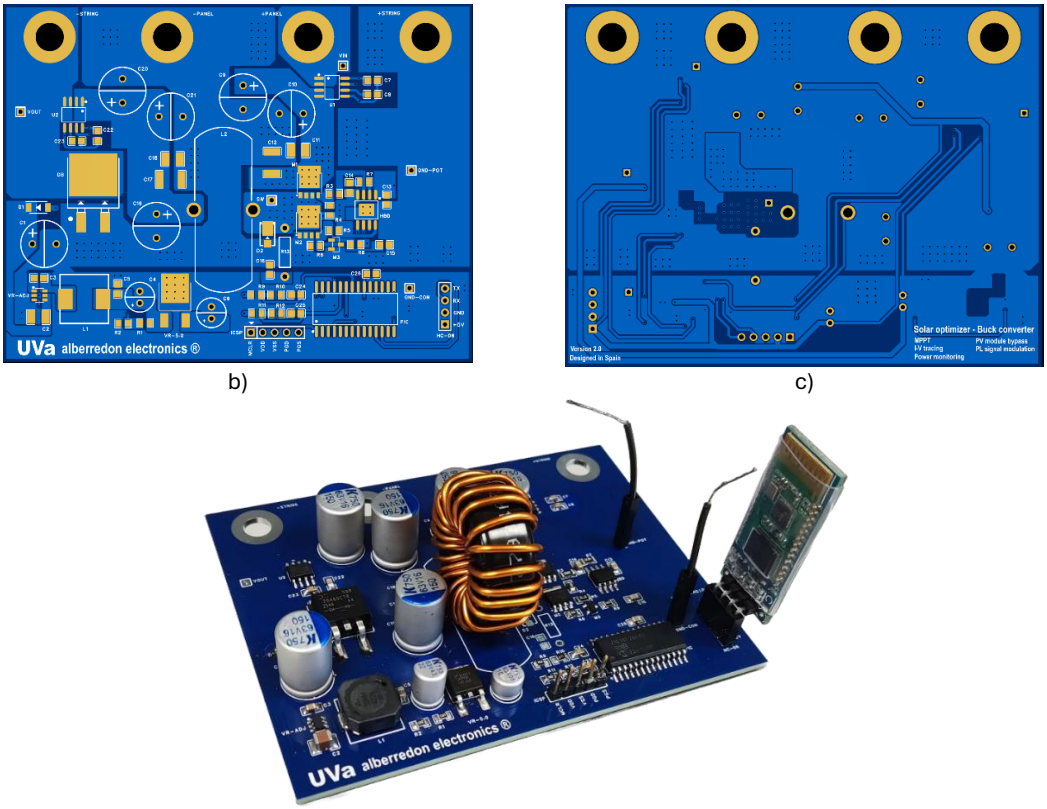

b) c)

c)

Figure 41. Views of the developed module-level PV optimizer. Top side (a), bottom side (b), and photograph of the assembled board (c).

Finally, all the components used in the development of the module-level PV optimizer are listed in Table 6. This allows calculation of the total cost of the board, which amounts to 26.81 € per unit. This cost only includes the components and does not cover design or manufacturing/soldering time. Note that this total cost is the result of the chosen components, which can be optimized to reduce expenses. Moreover, prices may vary over time depending on the supplier and the quantity purchased. Nevertheless, it provides a useful reference for the total price.

Table 6. List of components and prices used in the developed module-level PV optimizer. Unit prices for 2025 correspond to purchases of at least 100 units.

System	Part	Reference	Units	Unitary price	Total price
Power	MOSFET	BUK9Y4R8-60E,115	2	0.90 €	1.80 €
Power	150 µF Capacitor	A759MW157M1JAAE048	5	1.16 €	5.80 €
Power	4.7 µF MLCC Capacitor	KAM32LR72A475KU	2	0.35 €	0.70 €
Power	1 µF MLCC Capacitor	C1812Y105K1RACAUTO	2	0.49 €	0.98 €
Power	Toroidal core	0077894A7	1	1.07 €	1.07 €
Power	Copper wire (0.9 m)	-	1	0.22 €	0.22 €
Power	Diode	SBR20A60CTB	1	0.61 €	0.61 €
Supply	Diode	RB168LAM100TR	1	0.16 €	0.16 €
Supply	150 µF Capacitor	A759MW157M1JAAE048	1	1.16 €	1.16 €
Supply	4.7 µF MLCC Capacitor	KAM32LR72A475KU	1	0.35 €	0.35 €
Supply	22 µF Capacitor	A759EK226M1JAAE054	1	0.20 €	0.20 €
Supply	10 µF Capacitor	A759EA106M1JAAE060	1	0.17 €	0.17 €
Supply	MLCC Capacitor	-	2	0.02 €	0.04 €
Supply	330 µH Coil	B82464G4334M	1	0.84 €	0.34 €
Supply	SMD resistor	-	2	0.01 €	0.02 €
Supply	Voltage regulator	LMR51606YDBVR	1	0.68 €	0.68 €
Supply	Voltage regulator	LP2950CDTX-5.0/NOPB	1	0.69 €	0.69 €
Control	Microcontroller	PIC18F26K83-E/SO	1	2.02 €	2.02 €
Control	MLCC Capacitor	-	4	0.02 €	0.08 €
Control	Half-bridge driver	NGD4300DDJ	1	0.90 €	0.90 €
Control	MOSFET	SQ2362CES-T1_GE3	1	0.24 €	0.24 €
Control	SMD resistor	-	6	0.01 €	0.06 €
Sensing	Current sensor	ACS715ELCTR-20A-T	2	2.63 €	5.26 €
Sensing	MLCC Capacitor	-	6	0.02 €	0.12 €
Sensing	SMD resistor	-	4	0.01 €	0.04 €
Communication	Bluetooth module	HC-06	1	1.79 €	1.79 €
PCB	Board	-	1	0.81 €	0.81 €
Total price					**26.81 €**

6.3. Efficiency and MPPT

The electrical performance of the converter has been analysed under different conditions. The switching frequency of the converter is 100 kHz. Figure 42 shows two different scenarios regarding the converter's input voltage. An input voltage of 30 V represents the typical V_{MPP} of modules composed of 60 solar cells connected in series. Other modules on the market consist of 72 solar cells in series, resulting in a V_{MPP} of approximately 40 V.

The efficiency of the converter has been measured using a power supply at the input and a variable electronic load at the output, which were used to calculate efficiency. The efficiency curves exhibit the expected shape. At low input power, the constant standby power consumption of the control and communication system (measured at around 350-400 mW) has a significant impact, explaining the lower efficiency when the converter operates at low power. As the input power increases, this constant power consumption has a smaller effect on overall efficiency, resulting in an increase in efficiency until it reaches a peak. Beyond this peak, efficiency begins to decrease due to Joule losses. While the standby power consumption remains constant and switching losses are proportional to the handled power, Joule losses depend on the cube of the current. Increasing the power leads to higher currents at both the input and output of the converter, which explains the efficiency drop in this region.

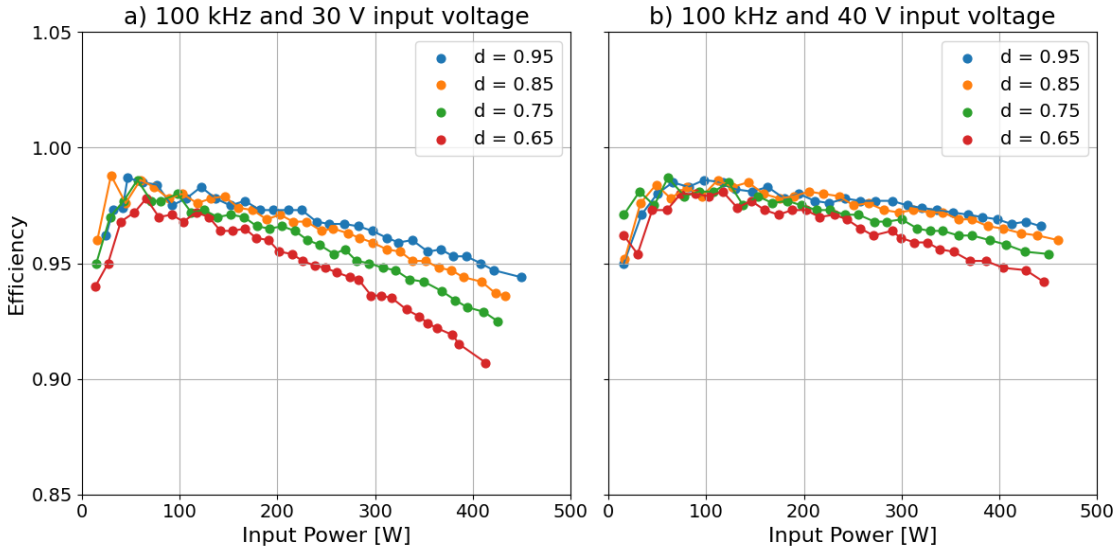

Figure 42.. Efficiency curves of the developed module-level PV optimizer at a switching frequency of 100 kHz, with input voltages of 30 V (a) and 40 V (b), and different duty cycles.

The converter has demonstrated a peak efficiency of around 98%, which is comparable to commercial solutions. Moreover, it maintains an efficiency higher than 95% in most operating conditions. It should be noted that, for the same duty cycle and input power, higher efficiency is expected at higher voltages, as higher voltages involve lower currents for the same power, thereby minimizing Joule losses. Conversely, a reduction in efficiency is expected at lower duty cycles for the same power, since lower duty cycles result in lower output voltage and consequently higher current, which increases Joule losses.

In real scenarios where module-level PV optimizers are installed within a PV string, all optimizers should operate at a high duty cycle close to 100% if all modules have similar I-V characteristics, since the PV inverter will set a current near the modules' I_{MPP} . However, if one module is, for example, partially shaded and its I_{MPP} drops, the duty cycle of its optimizer should decrease, increasing the ratio between the module's input current and the common string current at the output.

It is also possible to analyse the performance of the programmed P&O MPPT algorithm in the module-level PV optimizer. To this end, the module current was measured with an oscilloscope, starting from open-circuit conditions (optimizer off) until a constant current was reached. Subsequently, an I–V curve was traced, confirming that the current set by the optimizer corresponds to I_{MPP}, as shown in Figure 43. It is also possible to check that around 4 s are required to find MPP.

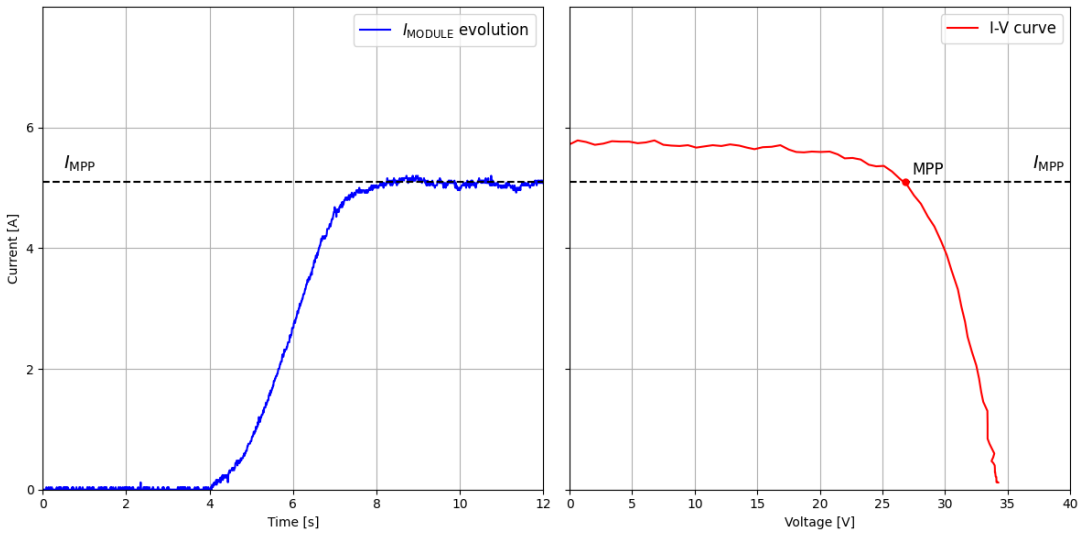

a) b)

Figure 43. Current evolution during MPPT of the module-level optimizer (a) and the corresponding I–V curve of the PV module being optimized (b).

6.4. Non-invasive I-V tracing and PL imaging

According to the presented technique, the I-V curve has been measured using the developed module-level PV optimizer. Figure 44 (a) shows the current and voltage measurements recorded by the PV optimizer during the I-V curve sweep, based on the charging of the input capacitance. Under irradiance conditions of 1,030 W/m^2 and the module characteristics, the charging period was 1.8 ms. Given the microcontroller's sampling rate of 90 kHz, 142 current and voltage measurements were captured, allowing the reconstruction of the module's I-V curve with a resolution of 71 points, as can be seen in Figure 44 (b).

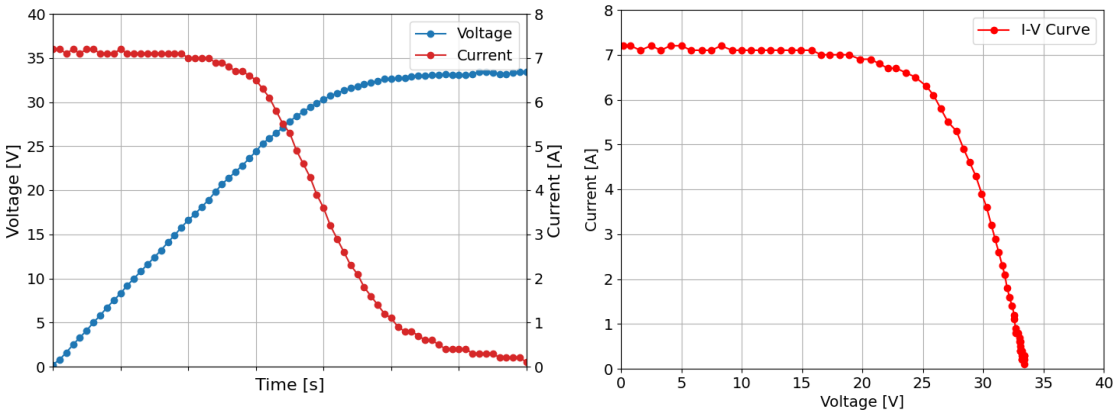

Figure 44. Measured current and voltage during I-V sweep (a) and reconstructed I-V curve of a PV module (TSM-235-PC05A) under 1,030 W/m² (b). Data captured during 1.8 ms with I-V curve sampled at 71 points.

The performance of the I-V curve tracing using the developed optimizer has also been validated through comparison with measurements taken by a commercial I-V tracer (HT instruments Solar I-Ve 1500 I-V curve tracer). To do this, measurements were first taken with the developed I-V tracer, followed by a rapid disconnection and connection to the commercial I-V tracer, allowing consecutive measurements of the same module within a few seconds and ensuring nearly identical environmental conditions. As shown in Figure 45, both sets of measurements are very similar, providing a strong indication of the proper performance of the developed I-V tracing technique.

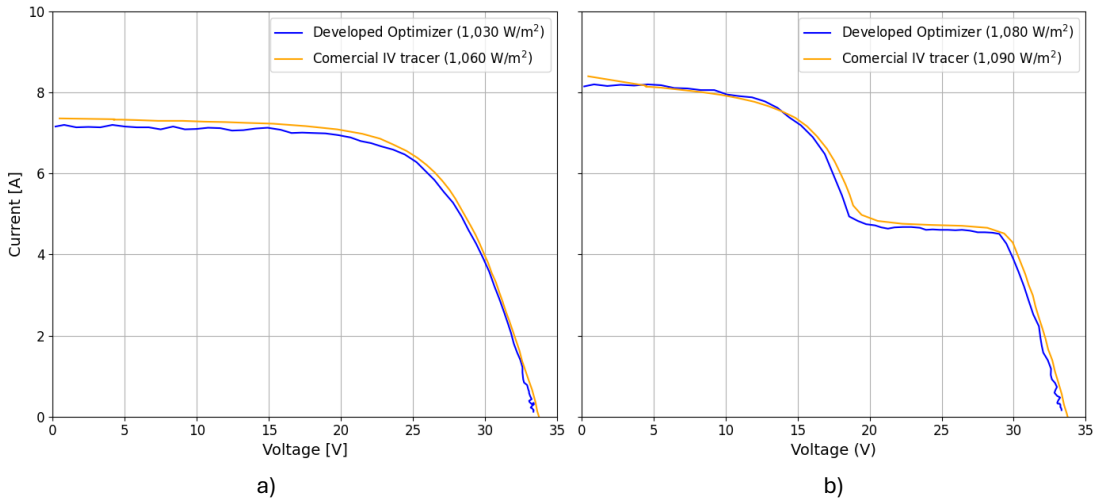

Figure 45. Comparison of I–V curves measured by the developed module-level PV optimizer and a commercial I–V tracer (HT Instruments Solar I-Ve 1500) for one unshaded module (left) and one shaded module (right).

Non-invasive PL imaging was performed by modulating the PL signal using the developed optimizer within a PV string composed of polycrystalline silicon modules (TSM-235-PC05A). The PL signal was modulated at 7 Hz following a square waveform, while the InGaAs camera and filter described in Chapter V captured a sequence of 1,000 images with 2 ms exposure time at an acquisition rate of 53 fps.

The image sequence was processed in the time-domain using an asynchronous strategy. Figure 46 shows the resulting daylight PL image, with modulation performed by the PV optimizer, alongside a conventional EL image obtained in a dark environment. The SNR, calculated according to Equation (9) for the daylight PL image, was 7.55, which is higher than the minimum recommended value of 5.

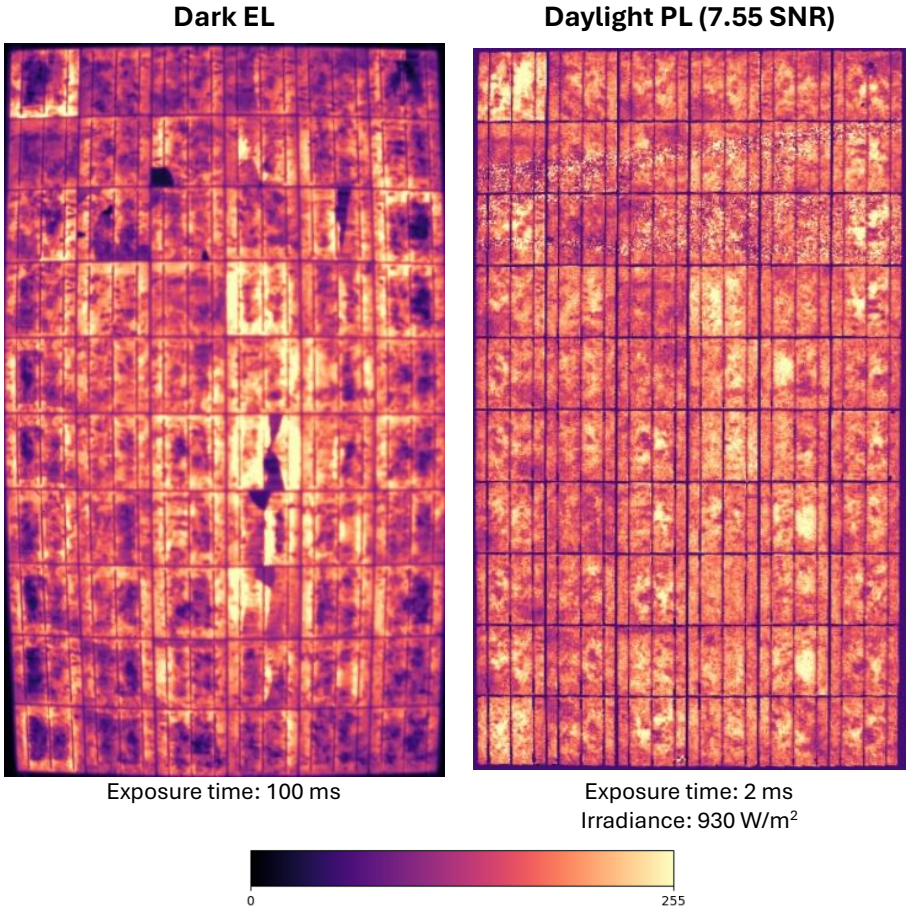

Figure 46. Daylight PL image based on the developed PV optimizer and dark EL images of the same PV module (TSM-235-PC05A).

Figure 47 includes detailed pictures of specific solar cells, including dark EL and daylight PL imaging done by the optimizer. It should be noted that in PL imaging some faults such as inactive areas may be difficult to identify due to the excitation mechanism of PL. For example, the central solar cell in the first row has some cracks that create an isolated area in the cell. This area is easily identified in EL imaging as this region is electrically isolated, so any forward-bias current goes through it and its EL signal contribution is null, resulting in a dark area. However, this specific defect in PL is more difficult to identify, as sunlight can generate PL signal in this isolated area. On another example, left-middle solar cell of the second row exhibits a clear inactive area in EL imaging, a pattern that is not detected in PL imaging.

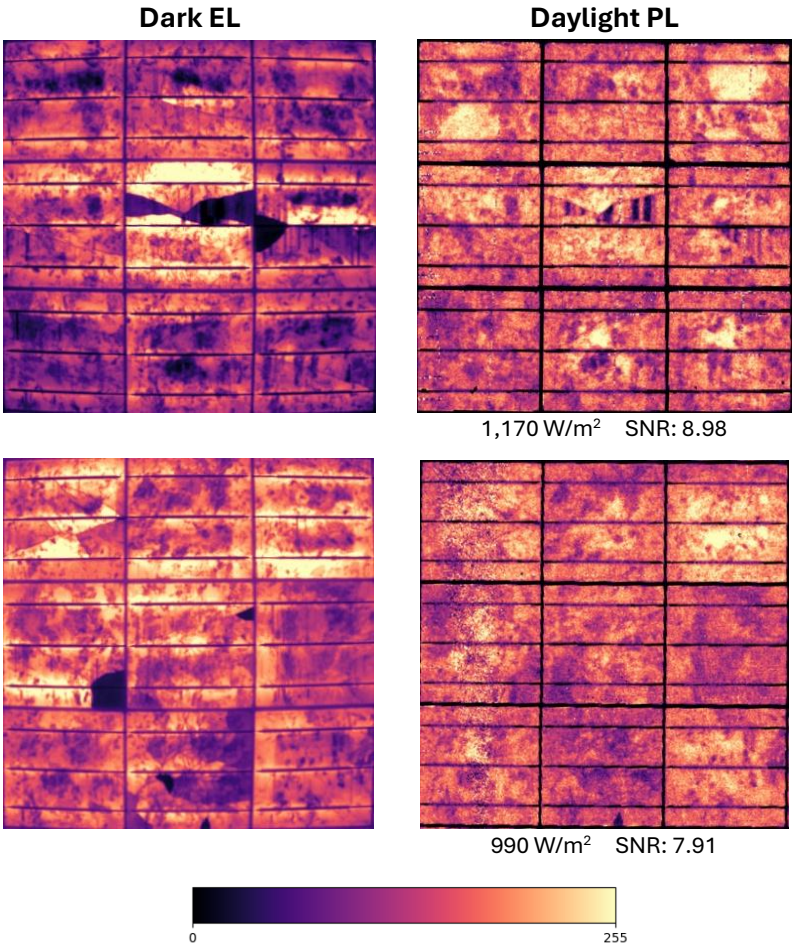

Figure 47. Detailed dark EL and daylight PL pictures of specific cells of the PV module (TSM-235-PC05A).

6.5. Discussion

The growing interest in and adoption of MLPE electronics in recent years presents a significant opportunity to integrate non-invasive inspection techniques into PV modules. This chapter has presented the design and validation of a module-level PV optimizer that successfully incorporates both PL modulation and I-V tracing, enabling these two inspection methods to be performed non-invasively.

A P&O algorithm has been successfully implemented in the optimizer to perform MPPT on individual modules. Moreover, a peak efficiency of approximately 98% has been achieved, which is comparable to available commercial solutions.

PL signal modulation has been integrated via software, without the need for additional hardware in the optimizer, as the PL signal is modulated by periodically varying the duty cycle. In this context, the choice of a buck topology has allowed the optimizer to set OC and high-current conditions, alternating between high and low PL signal intensity states. This approach has enabled the successful acquisition of daylight PL images with acceptable SNR values. EL modulation has not been integrated, as it would require major hardware modifications and additional power stages. In this regard, simplicity and low cost have been prioritized over EL modulation functionality.

The integration of I-V tracing does not require any changes to the converter's power topology, as a capacitance sweep has been implemented. All the elements necessary for

these techniques are already provided by the topology of the buck converter and the sensing required for MPPT. The board can bypass the module and create a short circuit thanks to the half-bridge present in the synchronous buck topology. Moreover, when the module transitions from SC to OC, the charging of the converter's input capacitor facilitates the capacitance sweep of the I-V curve, which is measured using the current and voltage sensors already required for the implementation of the MPPT algorithm.

Nevertheless, it is necessary to include a dedicated power supply capable of supporting the control, sensing, and communication systems while the module operates under short-circuit conditions for a brief period. Additionally, it is desirable to implement a soft short circuit of the half-bridge to prevent abrupt discharges of the input capacitor and high current peaks that could damage the MOSFETs. Although the integrated I-V tracing achieves an accuracy comparable to commercial I-V tracers, the nature of the technique means that the number of points in the resulting I-V curve depends on the charging time of the input capacitor (which is influenced by the capacitor size, irradiance, and I-V characteristics of the module) as well as the sampling rate of the voltage and current sensors.

The PV optimizer is also capable of actively or passively bypassing the module thanks to the inclusion of a bypass diode. This feature not only enables module bypass during I-V tracing but also ensures normal operation of the string if a PV optimizer fails. Furthermore, the module-level PV optimizer enhances individual monitoring of voltage, current, and power.

In terms of cost, all components required for the design amount to a total of 26.81 €, of which only 1.59 € corresponds to the additional hardware that enables non-invasive I-V tracing and PL signal modulation. Overall, the proposed solution, which integrates non-invasive I-V tracing and PL signal modulation, represents a significant novelty in the state of the art, providing a feasible approach for advanced module inspection within MLPE systems.

Chapter VII

Conclusions

7.1. Conclusions

EL and PL imaging applied to PV modules has proven to be highly useful, enhancing fault detection and enabling performance analysis of PV devices. However, acquiring both EL and PL images in field-deployed modules presents several challenges and drawbacks that limit their practical use, despite the high potential they offer. In this context, exploring novel techniques aimed at overcoming the main limitations of conventional luminescence imaging is of great interest, as it could allow the technique to become a mainstream diagnostic method in PV power plants.

Conventional EL imaging requires nighttime measurements, external power supplies, and system disconnection, making it an invasive and logistically complex inspection method. In contrast, novel approaches explored by research groups worldwide aim to render luminescence imaging non-invasive, eliminating the need for disconnection and allowing measurements during normal operation. Moreover, it is desirable to develop techniques that operate without external power supplies or illumination devices, which are typically necessary in conventional measurements and add to system complexity. Finally, enabling imaging under daylight conditions is particularly advantageous, as nighttime inspections pose additional safety concerns.

This thesis has investigated daylight EL and PL imaging through module-level electronics that enable non-invasive luminescence measurements without the need for external energy sources, thereby addressing the main limitations of conventional approaches. The findings can be grouped into three main areas: the development of an embedded module-level electronic architecture for non-invasive EL and PL modulation, the exploration of different measurement processing strategies to filter background signals generated by sunlight, and the integration of non-invasive PL modulation together with I–V curve tracing within the topology of a module-level PV optimizer.

Firstly, a module-level electronic architecture has been designed and experimentally validated to achieve non-invasive modulation of EL and PL under daylight conditions. The system allows the PV module to operate normally while enabling the induction of a strong EL signal by driving a forward-bias current, using the energy generated by the other modules in the PV string. Similarly, a strong PL signal is obtained by bypassing the module and setting OC conditions, where sunlight induces high PL emission. This approach introduces several advantages and novelties with respect to the state of the art. While non-invasive PL imaging has been reported using different modulation strategies, non-invasive EL imaging under daylight conditions has not been explored before. Furthermore, the acquisition of both EL and PL images is highly desirable, since these techniques provide similar but complementary information. It should also be emphasized that daylight measurements can be performed without the need for external energy sources to generate the luminescence signal, thereby overcoming one of the main limitations of conventional luminescence techniques.

Secondly, this device enables the modulation of EL and PL signals, allowing the acquisition of image sequences in which lock-in detection can be applied to remove background generated by sunlight, thus providing final images suitable for fault detection and PV module analysis. Several strategies have been successfully implemented to accomplish this task. Time-domain processing requires binary modulation of the luminescence signal, following a square waveform. Since it is necessary to identify which images within the sequence correspond to high or low luminescence states, two strategies can be adopted. A synchronous strategy involves continuous coordination and communication between the device that modulates the signal and the camera, enabling direct labelling of images according to their emission state. In contrast, an asynchronous strategy does not require coordination between the camera and the modulation device but instead relies on an algorithm to automatically classify images within the sequence. Although the synchronous strategy yields slightly better results due to the absence of algorithmic misclassification errors, the asynchronous approach offers several advantages, such as potentially higher measurement speed, simpler implementation, and the ability to perform measurements without synchronization, a particularly relevant feature in scenarios where synchronization is challenging, for example when UAVs are employed.

Frequency-domain processing is based on FFT and allows the removal of background signals when the EL or PL signal is modulated with any periodic waveform. With minor hardware and software modifications to the developed electronic device, arbitrary modulation following different waveforms can be achieved. Thanks to its simpler and more direct integration, arbitrary EL signal modulation has been successfully implemented using various waveforms. Comparable images, both qualitatively and quantitatively, have been obtained in comparison with those generated using a programmable power supply for this task. Moreover, although all modulation waveforms provide similar qualitative results, the square waveform offers superior quantitative performance in terms of SNR. A direct comparison with time-domain processing is not straightforward, as quantitative quality assessment through SNR cannot be performed. However, frequency-domain processing entails a higher computational cost. Overall, frequency-domain processing may be particularly useful in modulation techniques where current variations in the module are slow and square waveforms cannot be generated, such as when an inverter is used for luminescence signal modulation.

Thirdly and finally, the proposed electronic architecture presents a main limitation: integrating a module-level electronic device into the thousands of PV modules that constitute a utility-scale power plant is not desirable, as it would lead to a substantial increase in initial investment. For this reason, signal modulation functionality has been integrated into the topology of a PV module-level optimizer that performs MPPT on individual modules. Additionally, non-invasive I–V tracing has also been incorporated into the proposed architecture, converting luminescence imaging and I–V tracing into non-invasive techniques.

Although EL modulation has not been integrated due to its higher complexity and the need for major hardware modifications compared to the conventional topology of a PV optimizer, PL modulation and I–V tracing have been incorporated with only minor changes, corresponding to a component cost increase of 6.3% relative to the hardware required solely for MPPT. The total cost of the PV optimizer is approximately double that of the standalone electronic device developed for EL and PL modulation. Nevertheless, the optimizer offers broader functionality, making it a more attractive solution for integration into real PV power plants.

It should be noted that the proposed PV optimizer uses the buck converter topology, one of the most common and widely adopted solutions for non-isolated DC–DC converters. Thanks to appropriate component selection and careful PCB design, the developed module-level PV optimizer has achieved a peak efficiency of around 98%, which is comparable to commercial solutions available on the market. Furthermore, the integration of the P&O algorithm has enabled successful MPPT operation. Regarding inspection techniques, daylight PL imaging has been demonstrated, yielding final images of sufficient quality. In addition, I–V curves have been obtained, and their accuracy has been validated through comparison with commercial I–V tracers. Finally, the developed module-level PV optimizer incorporates additional functionalities such as active or passive bypass of the module, as well as module-level current, voltage, and power monitoring.

Taking all aspects into account, a series of points is presented summarizing the main conclusions and achievements of the present thesis.

- This thesis proposes a module-level embedded electronic architecture enabling non-invasive EL and PL modulation under daylight, eliminating external energy sources while allowing normal module operation during inspections.
- Processing within the time domain based on binary modulation has been explored, where synchronous and asynchronous strategies have been successfully implemented and validated. These approaches differ in whether communication between the signal-modulating device and the camera is required. While the asynchronous method is more practical and faster, the synchronous strategy yields slightly better results.
- The embedded electronic architecture has been modified to allow arbitrary modulation of the EL signal, enabling the implementation and validation of frequency-domain image processing based on FFT, thereby enhancing processing when the luminescence signal follows any periodic waveform.
- Using the electronic topology of a photovoltaic optimizer, a module-level electronic device has been designed and validated for achieving MPPT of individual modules, as well as non-invasive PL modulation and I-V tracing.

7.2. Future Works

The integration of non-invasive inspection techniques within MLPE presents a high potential that has barely been explored in the current scientific literature. The final part of this thesis has investigated the integration of non-invasive daylight PL imaging as well as I–V tracing using the electronic architecture of a PV module-level optimizer. However, future work will focus on exploring the integration of non-invasive inspection methods through PV microinverters.

PV microinverters have the potential to be designed to allow bidirectional power flow between PV modules and the grid, enabling the injection of a forward-bias current. This feature makes it possible to implement functionalities of high interest in the context of PV module inspections. First, non-invasive EL modulation becomes feasible, allowing daylight measurements. Second, I–V curves in the fourth quadrant can be measured, which is of interest for research purposes. Finally, microinverters could also enable the integration of advanced active thermography inspection methods, such as dark steady-state thermography, pulsed thermography and lock-in thermography.

Achievements and Contribution

This section provides an overview of the scientific achievements accomplished throughout the thesis, including the publications produced and the research stay undertaken.

Journal Publications

Redondo-Plaza, A.; Zorita-Lamadrid, Á.L.; Alonso-Gómez, V.; Hernández-Callejo, L. Inspection techniques in photovoltaic power plants: A review of electroluminescence and photoluminescence imaging. Renewables Energies 2024, 2(2), 1-23. https://doi.org/10.1177/27533735241282603.	
State	Published
Objective	This paper is aligned with specific objective Nº 1, which is addressed in Chapter III.
Summary	A proof of concept demonstrating the design of a module-level electronic device that enables non-invasive modulation of EL and PL signals without the need for external power sources, thereby allowing the acquisition of both PL and EL images of a module under daytime conditions.

Redondo-Plaza, A.; Morales-Aragonés, J.I.; Gallardo-Saavedra, S.; Mateo-Romero, H.F.; Araujo-Rendón, S.; Zorita-Lamadrid, Á.L.; Alonso-Gómez, V.; Hernández-Callejo, L. Passive Electroluminescence and Photoluminescence Imaging Acquisition of Photovoltaic Modules. Sensors 2024, 24, 1539. https://doi.org/10.3390/s24051539.	
State	Published
Objective	This paper is aligned with specific objective Nº 2, which is addressed in Chapter IV.
Summary	A review article focused on analysing the techniques used for obtaining EL and PL images in photovoltaic plants.

Redondo-Plaza, A.; Morales Aragonés, J.I.; Mateo-Romero, H.F.; Zorita-Lamadrid, Á.L.; Alonso-Gómez, V.; Hernández-Callejo, L. Passive Electroluminescence and Photoluminescence in Outdoor Photovoltaic Modules: Synchronous and Asynchronous Lock-In Strategies.	
State	Under review
Objective	This paper is aligned with specific objective Nº 3, which is addressed in Chapter V.
Summary	An article that compares two strategies (synchronous and asynchronous) for time-domain image processing required in EL and PL daylight measurements. The strategies differ in whether continuous communication between the camera and the developed module-level electronics is required.

Redondo-Plaza, A.; Velasco-Bonilla, A.Z.; Morales-Aragones, J.I.; Zorita-Lamadrid, Á.L.; Alonso-Gómez, V.; Hernández-Callejo, L. Electroluminescence Imaging Based on FFT Analysis for Outdoor Photovoltaic Module Inspection: A Self-Powered Signal Modulation Approach. *Appl. Sci.* 2025, *15*, 4606. https://doi.org/10.3390/app15094606.	
State	Published
Objective	This paper is aligned with specific objective Nº 3, which is addressed in Chapter V.
Summary	An article that presents the required modifications in the developed module-level electronics to enable arbitrary EL signal modulation, thereby enhancing frequency-domain processing through the use of FFT.

Redondo-Plaza, A.; Cardinale-Villalobos L.; Velasco-Bonilla A.Z.; Morales-Aragonés, J.I.; Alonso-Gómez, V.; Hernández-Callejo, L. Module-Level Photovoltaic Optimizer Based on a Synchronous Buck Converter for Non-Invasive I-V Curve Tracing and Daylight Photoluminescence.	
State	Under review
Objective	This paper is aligned with specific objective Nº 4, which is addressed in Chapter VI.
Summary	An article presenting the design and validation of a module-level PV optimizer that not only enables MPPT in individual modules but also allows non-invasive PL signal modulation and I–V tracing, with only minor hardware modifications compared to a conventional PV optimizer.

Conference Publications

Title	Electronic device for passive luminescence imaging acquisition: Proof of concept
Conference	ICSC-CITIES 2023
Identifier	ISBN: 978-607-99960-1-7
Objective	This conference paper is aligned with specific objective Nº 2, which is addressed in Chapter IV.
Summary	The idea of modulating EL and PL signal using an electronic device is validated though simulations.

Title	Passive Electroluminescence and Photoluminescence in Photovoltaic Modules: Synchronous and Asynchronous Lock-In Approaches
Conference	ICSC-CITIES 2024
Identifier	DOI: 10.1007/978-981-96-4301-1_1
Objective	This conference paper is aligned with specific objective Nº 3, which is addressed in Chapter V.
Summary	A comparison between synchronous and asynchronous strategies for time-domain processing of luminescence pictures in outdoor photovoltaic modules is presented.

Research Stays

University	University of Pretoria		
Department	Electrical, Electronic and Computer Engineering		
Duration	1 month		
Start date:	17/02/2024	End date:	15/03/2024
Funding	Programa ERASMUS+ Practicas		
Objective	This research stay is aligned with specific objective Nº 2, which is addressed in Chapter IV.		
Summary	Design of the printed circuit board for the module-level electronic device that enhances EL and PL modulation in a PV module.		

University	Costa Rica Institute of Technology		
Department	School of Electronic Engineering		
Duration	3 months		
Start date:	01/04/2025	End date:	01/07/2025
Funding	Ayudas complementarias de movilidad destinadas a beneficiarios del programa de formación del profesorado universitario (FPU) 2025.		
Objective	This research stay is aligned with specific objective Nº 4, which is addressed in Chapter VI.		
Summary	Design and validation of a PV module-level optimizer with I–V curve tracing and PL modulation functionalities.		

Funding

- Formación de Profesorado Universitario (FPU) 2021. Ministerio de Universidades. Plan Estatal de Investigación Científica, Técnica y de Innovación 2021-2023.

- Ayudas para La Asistencia a Cursos, Congresos y Jornadas Relevantes en el Desarrollo de Tesis Doctorales. Convocatoria 2024. Universidad De Valladolid.

- Programa Erasmus+ Prácticas. Universidad de Valladolid. Curso 2023/2024.

- Convocatoria de Ayudas a La Investigación a Desarrollar en el Curso 2024-2025. Cátedra Conocimiento e Innovación Caja Rural de Soria.

- Ayudas Complementarias de Movilidad Destinadas a Beneficiarios del Programa de Formación del Profesorado Universitario (FPU) 2025.

- Ministerio de Ciencia e Innovación, Agencia Estatal de Investigación, 10.13039/501100011033. Convocatoria 2020 de Proyectos de I+D+i, Orientada a los Retos de la Sociedad, del Plan Estatal de Investigación Científica, Técnica y de Innovación 2017-2020 (Agencia Estatal de Investigación). Caracterización Avanzada de Células Solares y Módulos de Alta Productividad y Bajo Impacto Ambiental hacia una Energía Fotovoltaica Verde, Circular y Sostenible (PID2020-113533rb-C33).

- U.T.E. Duques de Soria.-Arcor, S.L.U. Y Hermanos Rubio Grupo Constructor Herce, S.L.U. Convocatoria 2024 de Ayudas para la Realización de Proyectos De I+D+i sobre Medidas de Eficiencia Energética y de Aplicación de Energías Renovables en la Explotación de los Edificios Universitarios (Universidad De Valladolid (UVa)). Detección del Estado de La Fotovoltaica Instalada en la Universidad de Valladolid.

- Agencia Estatal De Investigación, Ministerio De Ciencia, Innovación y Universidades, Unión Europea, 10.13039/501100011033, Fondos FEDER. Convocatoria 2023 de Ayudas a «Proyectos de Generación de Conocimiento»-Investigación Orientada y a Actuaciones para la Formación de Personal Investigador Predoctoral Asociadas a Dichos Proyectos (Agencia Estatal De Investigación). Desarrollo De Técnicas Avanzadas de Caracterización: Hacia una Tecnología Fotovoltaica Tipo N (PID2023-148369OB-C43).

References

1. NASA: Global Temperature Available online: https://climate.nasa.gov/vital-signs/global-temperature/?intent=121 (accessed on 25 July 2025).
2. IPCC *Global Warming of 1.5 °C, Framing and Context*; 2022.
3. Horowitz, C.A. Paris Agreement. *International Legal Materials* 2016, *55*, doi:10.1017/s0020782900004253.
4. Deng, Z.; Zhu, B.; Davis, S.J.; Ciais, P.; Guan, D.; Gong, P.; Liu, Z. Global Carbon Emissions and Decarbonization in 2024. *Nat Rev Earth Environ* 2025, *6*, 231–233, doi:10.1038/s43017-025-00658-x.
5. Graham, E.; Fulghum, N.; Altieri, K. *Global Electricity Review 2025*; 2025.
6. SolarPower Europe *Global Market Outlook for Solar Power 2025-2029*; 2025.
7. International Energy Agency *Electricity 2024: Analysis and Forecast to 2030*; 2023.
8. International Energy Agency Evolution of Solar PV Module Cost by Data Source, 1970-2020. Available online: https://www.iea.org/data-and-statistics/charts/evolution-of-solar-pv-module-cost-by-data-source-1970-2020 (accessed on 21 June 2024).
9. IRENA *Renewable Power Generation Costs in 2024*; Abu Dhabi, 2025.
10. Chen, Y.; Chen, D.; Altermatt, P.P.; Zhang, S.; Wang, L.; Zhang, X.; Xu, J.; Feng, Z.; Shen, H.; Verlinden, P.J. Technology Evolution of the Photovoltaic Industry: Learning from History and Recent Progress. *Progress in Photovoltaics: Research and Applications* 2023, *31*, 1194–1204, doi:10.1002/pip.3626.
11. Bódis, K.; Kougias, I.; Jäger-Waldau, A.; Taylor, N.; Szabó, S. A High-Resolution Geospatial Assessment of the Rooftop Solar Photovoltaic Potential in the European Union. *Renewable and Sustainable Energy Reviews* 2019, *114*, 109309, doi:10.1016/j.rser.2019.109309.
12. Fakhraian, E.; Forment, M.A.; Dalmau, F.V.; Nameni, A.; Guerrero, M.J.C. Determination of the Urban Rooftop Photovoltaic Potential: A State of the Art. *Energy Reports* 2021, *7*, 176–185, doi:10.1016/j.egyr.2021.06.031.
13. Miravet-Sánchez, B.L.; García-Rivero, A.E.; Yuli-Posadas, R.A.; Inostroza-Ruiz, L.A.; Fernández-Guzmán, V.; Chávez-Juanito, Y.A.; Rutti-Marin, J.M.; Apesteguia-Infantes, J.A. Solar Photovoltaic Technology in Isolated Rural Communities in Latin America and the Caribbean. *Energy Reports* 2022, *8*, 1238–1248, doi:10.1016/J.EGYR.2021.12.052.
14. NREL *Life Cycle Greenhouse Gas Emissions from Electricity Generation: Update Life Cycle Assessment of Energy Systems*; 2021.
15. Hernández-Callejo, L.; Gallardo-Saavedra, S.; Alonso-Gómez, V. A Review of Photovoltaic Systems: Design, Operation and Maintenance. *Solar Energy* 2019, *188*, 426–440, doi:10.1016/j.solener.2019.06.017.

16. Peinado Gonzalo, A.; Pliego Marugán, A.; García Márquez, F.P. Survey of Maintenance Management for Photovoltaic Power Systems. *Renewable and Sustainable Energy Reviews* 2020, *134*, 110347, doi:10.1016/j.rser.2020.110347.

17. Spertino, F.; Corona, F. Monitoring and Checking of Performance in Photovoltaic Plants: A Tool for Design, Installation and Maintenance of Grid-Connected Systems. *Renew Energy* 2013, *60*, 722–732, doi:10.1016/j.renene.2013.06.011.

18. Waqar Akram, M.; Li, G.; Jin, Y.; Chen, X. Failures of Photovoltaic Modules and Their Detection: A Review. *Appl Energy* 2022, *313*, 118822, doi:10.1016/j.apenergy.2022.118822.

19. Jordan, D.C.; Barnes, T.M. Degradation Science from Nanometers to Kilometers: A Pathway to Rapid Detection for Reliable Photovoltaics. *Solar RRL* 2023, *7*, doi:10.1002/solr.202300170.

20. Jordan, D.C.; Kurtz, S.R. Photovoltaic Degradation Rates—an Analytical Review. *Progress in Photovoltaics: Research and Applications* 2013, *21*, 12–29, doi:10.1002/pip.1182.

21. Marc Köntges; Sarah Kurtz, C.P.; Ulrike Jahn; Karl A. Berger; Kazuhiko Kato; Thomas Friesen; Haitao Liu; Mike Van Iseghem *Review of Failures of Photovoltaic Modules*; 2014;

22. Hong, Y.-Y.; Pula, R.A. Methods of Photovoltaic Fault Detection and Classification: A Review. *Energy Reports* 2022, *8*, 5898–5929, doi:10.1016/j.egyr.2022.04.043.

23. Høiaas, I.; Grujic, K.; Imenes, A.G.; Burud, I.; Olsen, E.; Belbachir, N. Inspection and Condition Monitoring of Large-Scale Photovoltaic Power Plants: A Review of Imaging Technologies. *Renewable and Sustainable Energy Reviews* 2022, *161*, 112353, doi:10.1016/j.rser.2022.112353.

24. Mansouri; Lashab; Sera; Guerrero; Cherif Large Photovoltaic Power Plants Integration: A Review of Challenges and Solutions. *Energies (Basel)* 2019, *12*, 3798, doi:10.3390/en12193798.

25. Hijjawi, U.; Lakshminarayana, S.; Xu, T.; Piero Malfense Fierro, G.; Rahman, M. A Review of Automated Solar Photovoltaic Defect Detection Systems: Approaches, Challenges, and Future Orientations. *Solar Energy* 2023, *266*, 112186, doi:10.1016/j.solener.2023.112186.

26. Dhimish, M.; Holmes, V. Fault Detection Algorithm for Grid-Connected Photovoltaic Plants. *Solar Energy* 2016, *137*, 236–245, doi:10.1016/J.SOLENER.2016.08.021.

27. Manzoor, R.; Bhat, R.A.; Hafiz, A.M. Solar Cell Fault Detection Using Robust Machine Learning Algorithms. In Proceedings of the 2025 12th International Conference on Computing for Sustainable Global Development (INDIACom); IEEE, April 2 2025; pp. 01–06.

28. Hussain, M.; Dhimish, M.; Titarenko, S.; Mather, P. Artificial Neural Network Based Photovoltaic Fault Detection Algorithm Integrating Two Bi-Directional Input Parameters. *Renew Energy* 2020, *155*, 1272–1292, doi:10.1016/J.RENENE.2020.04.023.

29. Kothona, D.; Kouliousis, A.; Christoforidis, G.C. Fault Detection and Classification Methodology for Photovoltaic Systems Through AI-Based Digital Twin. In Proceedings of the 2024 3rd International Conference on Energy Transition in the Mediterranean Area (SyNERGY MED); IEEE, October 21 2024; pp. 1–5.

30. S. M. Ghoneim, S.; E. Rashed, A.; I. Elkalashy, N. Fault Detection Algorithms for Achieving Service Continuity in Photovoltaic Farms. *Intelligent Automation & Soft Computing* 2021, *29*, 467–479, doi:10.32604/iasc.2021.016681.

31. Kandeal, A.W.; Elkadeem, M.R.; Kumar Thakur, A.; Abdelaziz, G.B.; Sathyamurthy, R.; Kabeel, A.E.; Yang, N.; Sharshir, S.W. Infrared Thermography-Based Condition Monitoring of Solar Photovoltaic Systems: A Mini Review of Recent Advances. *Solar Energy* 2021, *223*, 33–43, doi:10.1016/j.solener.2021.05.032.

32. Ulrike Jahn, M.H.; Köntges, M.; Parlevliet, D.; Pagg, M.; Tsanakas, I.; Stein, J.S.; Berger, K.A.; Ranta, S.; French, R.H.; Richter, M.; et al. *Review on Infrared and Electroluminescence Imaging for PV Field Applications*; 2018.

33. Luo, X.; Li, X.; Yang, Q.; Wu, F.; Zhang, D.; Yan, W.; Xi, Z. Optimal Path Planning for UAV Based Inspection System of Large-Scale Photovoltaic Farm. In Proceedings of the 2017 Chinese Automation Congress (CAC); IEEE, October 2017; pp. 4495–4500.

34. Gallardo-Saavedra, S.; Hernández-Callejo, L.; Duque-Perez, O. Technological Review of the Instrumentation Used in Aerial Thermographic Inspection of Photovoltaic Plants. *Renewable and Sustainable Energy Reviews* 2018, *93*, 566–579, doi:10.1016/j.rser.2018.05.027.

35. Niccolai, A.; Gandelli, A.; Grimaccia, F.; Zich, R.; Leva, S. Overview on Photovoltaic Inspections Procedure by Means of Unmanned Aerial Vehicles. In Proceedings of the 2019 IEEE Milan PowerTech; IEEE, June 2019; pp. 1–6.

36. Kunz, O.; Schlipf, J.; Fladung, A.; Khoo, Y.S.; Bedrich, K.; Trupke, T.; Hameiri, Z. Outdoor Luminescence Imaging of Field-Deployed PV Modules. *Progress in Energy* 2022, *4*, 042014, doi:10.1088/2516-1083/ac9a33.

37. del Prado Santamaría, R.; Dhimish, M.; dos Reis Benatto, G.A.; Kari, T.; Poulsen, P.B.; Spataru, S. V. From Indoor to Daylight Electroluminescence Imaging for PV Module Diagnostics: A Comprehensive Review of Techniques, Challenges, and AI-Driven Advancements. *Micromachines (Basel)* 2025, *16*, 437, doi:10.3390/mi16040437.

38. Silva, J.A.; Serra, J.M.; Vallêra, A.M.; Lobato, K. Luminescence in Photovoltaics. In; 2019.

39. Vuković, M.; Wiig, M.S.; dos Reis Benatto, G.A.; Olsen, E.; Burud, I. A Review of Imaging Methods for Detection of Photoluminescence in Field-Installed Photovoltaic Modules. *Progress in Energy* 2024, *6*, 032001, doi:10.1088/2516-1083/ad4250.

40. Duran, E.; Piliougine, M.; Sidrach-de-Cardona, M.; Galan, J.; Andujar, J.M. Different Methods to Obtain the I-V Curve of PV Modules: A Review. In Proceedings of the 2008 33rd IEEE Photovolatic Specialists Conference; IEEE, May 2008; pp. 1–6.

41. Vidyanandan, K.V. An Overview of Factors Affecting the Performance of Solar PV Systems. *Energy Scan* 2017, *27*.

42. Fuyuki, T.; Kondo, H.; Yamazaki, T.; Takahashi, Y.; Uraoka, Y. Photographic Surveying of Minority Carrier Diffusion Length in Polycrystalline Silicon Solar Cells by Electroluminescence. *Appl Phys Lett* 2005, *86*, doi:10.1063/1.1978979.

43. Trupke, T.; Mitchell, B.; Weber, J.W.; McMillan, W.; Bardos, R.A.; Kroeze, R. Photoluminescence Imaging for Photovoltaic Applications. *Energy Procedia* 2012, *15*, 135–146, doi:10.1016/j.egypro.2012.02.016.

44. Trupke, T. Photoluminescence and Electroluminescence Characterization in Silicon Photovoltaics. In *Photovoltaic Solar Energy*; Wiley, 2016; pp. 322–338.

45. Redondo Plaza, A.; Ngungu, V.N.; Gallardo Saavedra, S.; Morales Aragonés, J.I.; Alonso Gómez, V.; Obregón, L.J.; Hernández Callejo, L. Partial Photoluminescence Imaging for Inspection of Photovoltaic Cells: Artificial LED Excitation and Sunlight Excitation. *Energies (Basel)* 2023, *16*, 4531, doi:10.3390/en16114531.

46. Fraunhofer Institute for Solar Energy Systems; PSE Projects GmbH *Photovoltaics Report*; 2023.

47. NREL Reference Air Mass 1.5 Spectra.

48. Doll, B.; del Rivero, E.C.; Hepp, J.; Pickel, T.; Buerhop, C.; Knecht, R.; Camus, C.; Hauch, J.; Parisi, J.; Brabec, C.J. Quantitative Assessment of the Influence of Camera and Parameter Choice for Outdoor Electroluminescence Investigations of Silicon Photovoltaic Panels. *Zeitschrift für Naturforschung A* 2019, *74*, 645–653, doi:10.1515/zna-2019-0025.

49. Rafferty, C.; King, C.; Ackland, B.; O'Neill, J.; Aberg, I.; Sriram, T.S.; Mackay, A.; Johnson, R. Monolithic Germanium SWIR Imaging Array. In Proceedings of the 2008 IEEE International Conference on Technologies for Homeland Security, HST'08; 2008.

50. BeyonSense | A Powerful SWIR Camera That Enables You to Catch the Invisible Available online: https://beyonsense.io/ (accessed on 1 August 2025).

51. dos Reis Benatto, G.A.; Mayordomo, A.A.; Del Prado Santamaria, R.; Kari, T.; Poulsen, P.B.; Spataru, S. V. Analysis of Solar Cell Electroluminescence Spectra for Daylight Inspection of C-Si PV Modules. In Proceedings of the 2023 IEEE 50th Photovoltaic Specialists Conference (PVSC); IEEE, June 11 2023; pp. 1–7.

52. Machín, A.; Márquez, F. Advancements in Photovoltaic Cell Materials: Silicon, Organic, and Perovskite Solar Cells. *Materials* 2024, *17*, 1165, doi:10.3390/ma17051165.

53. Kim, J.; Lee, S.; Chowdhury, S.; Yi, J. A Brief Review of Passivation Materials and Process for High Efficiency PERC Solar Cell. *Transactions on Electrical and Electronic Materials* 2022, *23*, 1–5, doi:10.1007/s42341-021-00366-5.

54. dos Reis Benatto, G.A.; Kari, T.; Del Prado Santamaría, R.; Mahmood, A.; Stoicescu, L.; Spataru, S.V. Evaluation of Daylight Filters for Electroluminescence Imaging Inspections of Crystalline Silicon Photovoltaic Modules. *Solar RRL* 2025, doi:10.1002/solr.202400654.

55. Elbarbary, Z.M.S.; Alranini, M.A. Review of Maximum Power Point Tracking Algorithms of PV System. *Frontiers in Engineering and Built Environment* 2021, *1*, 68–80, doi:10.1108/FEBE-03-2021-0019.

56. Nadeem, A.; Hussain, A. A Comprehensive Review of Global Maximum Power Point Tracking Algorithms for Photovoltaic Systems. *Energy Systems* 2023, *14*, 293–334, doi:10.1007/s12667-021-00476-2.

57. Başoğlu, M.E. Comprehensive Review on Distributed Maximum Power Point Tracking: Submodule Level and Module Level MPPT Strategies. *Solar Energy* 2022, *241*, 85–108, doi:10.1016/j.solener.2022.05.039.

58. Camail, P.; Allard, B.; Darnon, M.; Joubert, C.; Martin, C.; Trovão, J.P.F. Overview of DC/DC Converters for Concentrating Photovoltaics (CPVs). *Energies (Basel)* 2023, *16*, 7162, doi:10.3390/en16207162.

59. Lorente, D.G.; Pedrazzi, S.; Zini, G.; Dalla Rosa, A.; Tartarini, P. Mismatch Losses in PV Power Plants. *Solar Energy* 2014, *100*, 42–49, doi:10.1016/j.solener.2013.11.026.

60. Wurster, T.S.; Schubert, M.B. Mismatch Loss in Photovoltaic Systems. *Solar Energy* 2014, *105*, 505–511, doi:10.1016/j.solener.2014.04.014.

61. International Electrotechnical Commission IEC 60904-13 Photovoltaic Devices – Part 13: Electroluminescence Imaging of Photovoltaic Modules 2018.

62. Mantel, C.; Dos Reis Benatto, G.A.; Riedel, N.; Thorsteinsson, S.; Poulsen, P.B.; Parikh, H.; Spataru, S.; Sera, D.; Forchhammer, S. SNR Study of Outdoor Electroluminescence Images under High Sun Irradiation. In Proceedings of the 2018 IEEE 7th World Conference on Photovoltaic Energy Conversion (WCPEC) (A Joint Conference of 45th IEEE PVSC, 28th PVSEC & 34th EU PVSEC); IEEE, June 2018; pp. 3285–3289.

63. Ballestín-Fuertes, J.; Muñoz-Cruzado-Alba, J.; Sanz-Osorio, J.F.; Hernández-Callejo, L.; Alonso-Gómez, V.; Morales-Aragones, J.I.; Gallardo-Saavedra, S.; Martínez-Sacristan, O.; Moretón-Fernández, Á. Novel Utility-Scale Photovoltaic Plant Electroluminescence Maintenance Technique by Means of Bidirectional Power Inverter Controller. *Applied Sciences* 2020, *10*, 3084, doi:10.3390/app10093084.

64. Bullich-Massagué, E.; Cifuentes-García, F.-J.; Glenny-Crende, I.; Cheah-Mañé, M.; Aragüés-Peñalba, M.; Díaz-González, F.; Gomis-Bellmunt, O. A Review of Energy Storage Technologies for Large Scale Photovoltaic Power Plants. *Appl Energy* 2020, *274*, 115213, doi:10.1016/j.apenergy.2020.115213.

65. Aragon-Aviles, S.; Kadam, A.H.; Sidhu, T.; Williamson, S.S. Modeling, Analysis, Design, and Simulation of a Bidirectional DC-DC Converter with Integrated Snow Removal Functionality for Solar PV Electric Vehicle Charger Applications. *Energies (Basel)* 2022, *15*, 2961, doi:10.3390/en15082961.

66. Coello, J.; Pérez, L.; Domínguez, F.; Navarrete, M. On-Site Quality Control of Photovoltaic Modules with the PV MOBILE LAB. In Proceedings of the Energy Procedia: 2013 ISES Solar World Congress; Elsevier, January 1 2014; Vol. 57, pp. 89–98.

67. Navarrete, M.; Pérez, L.; Domínguez, F.; Castillo, G.; Gómez, R.; Martínez, M.; Coello, J.; Parra, V. On-Site Inspection of PV Modules Using an Internationally Accredited PV Mobile Lab: A Three-Years Experience Operating Worldwide. In Proceedings of the 31st European Photovoltaic Solar Energy Conference and Exhibition; 2015; pp. 1989–1991.

68. Doll, B.; Kornhas, J.; Hepp, J.; Buerhop, C.; Hauch, J.; Camus, C.; Brabec, C.J. Towards True Contactless Outdoor Luminescence of Silicon Photovoltaic Modules with Inhomogeneous Small Area Excitation Source. In Proceedings of the 2018 IEEE 7th World Conference on Photovoltaic Energy Conversion (WCPEC) (A Joint Conference of 45th IEEE PVSC, 28th PVSEC & 34th EU PVSEC); IEEE, June 2018; pp. 0390–0394.

69. Doll, B.; Hepp, J.; Hoffmann, M.; Schuler, R.; Buerhop-Lutz, C.; Peters, I.M.; Hauch, J.A.; Maier, A.; Brabec, C.J. Photoluminescence for Defect Detection on Full-Sized Photovoltaic Modules. *IEEE J Photovolt* 2021, *11*, 1419–1429, doi:10.1109/JPHOTOV.2021.3099739.

70. Guada, M.; Moretón, Á.; Rodríguez-Conde, S.; Sánchez, L.A.; Martínez, M.; González, M.Á.; Jiménez, J.; Pérez, L.; Parra, V.; Martínez, O. Daylight Luminescence System for Silicon Solar Panels Based on a Bias Switching Method. *Energy Sci Eng* 2020, *8*, 3839–3853, doi:10.1002/ese3.781.

71. Martínez, O.; Guada, M.; Moretón, A.; Rodríguez-Conde, S.; González, M.A.; Jiménez, J.; Pérez, J.; Martínez, M.; Florez, J.A.; Silva, H.; et al. Implementation of a Friendly Daylight Electroluminescence System for the Inspection of Solar Pv Panels. In Proceedings of the 33rd European Photovoltaic Solar Energy Conference and Exhibition; 2017; pp. 2021–2025.

72. Dos Reis Benatto, G.A.; Mantel, C.; Riedel, N.; Santamaria Lancia, A.A.; Thorsteinsson, S.; Poulsen, P.B.; Forchhammer, S.; Thorseth, A.; Dam-Hansen, C.; Frederiksen, K.H.B.; et al. Outdoor Electroluminescence Acquisition Using a Movable Testbed. In Proceedings of the 2018 IEEE 7th World Conference on Photovoltaic Energy Conversion (WCPEC) (A Joint Conference of 45th IEEE PVSC, 28th PVSEC & 34th EU PVSEC); IEEE, June 2018; pp. 0400–0404.

73. Stoicescu, L.; Reuter, M.; Werner, J.H. DaySy: Luminiscence Imaging of PV Modules in Daylight. In Proceedings of the 29th European Photovoltaic Solar Energy Conference Exhibition; 2014.

74. Kropp, T.; Berner, M.; Stoicescu, L.; Werner, J.H. Self-Sourced Daylight Electroluminescence From Photovoltaic Modules. *IEEE J Photovolt* 2017, *7*, 1184–1189, doi:10.1109/JPHOTOV.2017.2714188.

75. Terrados, C.; González-Francés, D.; Sulca, K.P.; de Castro, C.; González, M.A.; Martínez, O. Towards Contactless Daylight Photoluminescence of PV Strings During Operation by Electrical Modulation. *Progress in Photovoltaics: Research and Applications* 2025, doi:10.1002/pip.70004.

76. Bhoopathy, R.; Kunz, O.; Juhl, M.; Trupke, T.; Hameiri, Z. Inspecting Series Resistance Effects and Bypass Diode Failure Using Contactless Outdoor Photoluminescence Imaging. In Proceedings of the 2018 IEEE 7th World Conference on Photovoltaic Energy Conversion (WCPEC) (A Joint Conference of 45th IEEE PVSC, 28th PVSEC & 34th EU PVSEC); IEEE, June 2018; pp. 0377–0380.

77. Bhoopathy, R.; Kunz, O.; Juhl, M.; Trupke, T.; Hameiri, Z. Outdoor Photoluminescence Imaging of Photovoltaic Modules with Sunlight Excitation. *Progress in Photovoltaics: Research and Applications* 2018, *26*, 69–73, doi:10.1002/pip.2946.

78. Kunz, O.; Rey, G.; Juhl, M.K.; Trupke, T. High Throughput Outdoor Photoluminescence Imaging via PV String Modulation. In Proceedings of the 2021 IEEE 48th Photovoltaic Specialists Conference (PVSC); IEEE, June 20 2021; pp. 0346–0350.

79. Kunz, O.; Weber, J.W.; Rey, G.; Juhl, M.; Trupke, T. Daylight Photoluminescence Imaging via Optical String Switching. *Solar RRL* 2024, *8*, doi:10.1002/solr.202400385.

80. Weber, J.W.; Kunz, O.; Knaack, C.; Chung, D.; Barson, A.; Slade, A.; Ouyang, Z.; Gottlieb, H.; Trupke, T. Daylight Photoluminescence Imaging of Photovoltaic Systems Using Inverter-based Switching. *Progress in Photovoltaics: Research and Applications* 2024, *32*, 643–651, doi:10.1002/pip.3807.

81. Vuković, M.; Eriksdatter Høiaas, I.; Jakovljević, M.; Svarstad Flø, A.; Olsen, E.; Burud, I. Photoluminescence Imaging of Silicon Modules in a String. *Progress in Photovoltaics: Research and Applications* 2022, *30*, 436–446, doi:10.1002/pip.3525.

82. Vuković, M.; Høiaas, I.E.; Jakovljević, M.; Flø, A.S.; Olsen, E.; Burud, I. Outdoor Photoluminescence and Electroluminescence Imaging of Photovoltaic Silicon Modules in a String. In Proceedings of the 11th International Conference on Crystalline Silicon Photovoltaics; 2022; p. 030012.

83. Bhoopathy, R.; Kunz, O.; Juhl, M.; Trupke, T.; Hameiri, Z. Outdoor Photoluminescence Imaging of Solar Panels by Contactless Switching: Technical Considerations and Applications. *Progress in Photovoltaics: Research and Applications* 2020, *28*, 217–228, doi:10.1002/pip.3216.

84. Vuković, M.; Jakovljević, M.; S. Flø, A.; Olsen, E.; Burud, I. Noninvasive Photoluminescence Imaging of Silicon PV Modules in Daylight. *Appl Phys Lett* 2022, *120*, doi:10.1063/5.0097576.

85. Vuković, M.; Hillestad, M.; Jakovljević, M.; S. Flø, A.; Olsen, E.; Burud, I. Photoluminescence Imaging of Field-Installed Photovoltaic Modules in Diffuse Irradiance. *J Appl Phys* 2023, *134*, doi:10.1063/5.0160897.

86. Kunz, O.; Rey, G.; Bhoopathy, R.; Hameiri, Z.; Trupke, T. Outdoor PL Imaging of Crystalline Silicon Modules at Constant Operating Point. In Proceedings of the 2020 47th IEEE Photovoltaic Specialists Conference (PVSC); IEEE, June 14 2020; pp. 2140–2143.

87. Rey, G.; Kunz, O.; Green, M.; Trupke, T. Luminescence Imaging of Solar Modules in Full Sunlight Using Ultranarrow Bandpass Filters. *Progress in Photovoltaics: Research and Applications* 2022, *30*, 1115–1121, doi:10.1002/pip.3563.

88. Mahdavipour, Z. Defect Inspection of Photovoltaic Solar Modules Using Aerial Electroluminescence (EL): A Review. *Solar Energy Materials and Solar Cells* 2024, *278*, 113210, doi:10.1016/j.solmat.2024.113210.

89. Weber, T.; Sobottka, C.; Fladung, A.; Clemens, P.; Berghold, J. Outdoor Electroluminescence Imaging Of Crystalline Photovoltaic Modules: Comparative Study Between Manual Ground-Level Inspections And Drone-Based Aerial Surveys. In Proceedings of the 32nd European Photovoltaic Solar Energy Conference and Exhibition; 2016; pp. 1736–1740.

90. Islam, M.; Rashel, M.R.; Ahmed, M.T.; Islam, A.K.M.K.; Tlemçani, M. Artificial Intelligence in Photovoltaic Fault Identification and Diagnosis: A Systematic Review. *Energies (Basel)* 2023, *16*, 7417, doi:10.3390/en16217417.

91. Mateo Romero, H.F.; González Rebollo, M.Á.; Cardeñoso-Payo, V.; Alonso Gómez, V.; Redondo Plaza, A.; Moyo, R.T.; Hernández-Callejo, L. Applications of Artificial Intelligence to Photovoltaic Systems: A Review. *Applied Sciences* 2022, *12*, 10056, doi:10.3390/app121910056.

92. Hussain, T.; Hussain, M.; Al-Aqrabi, H.; Alsboui, T.; Hill, R. A Review on Defect Detection of Electroluminescence-Based Photovoltaic Cell Surface Images Using Computer Vision. *Energies (Basel)* 2023, *16*, 4012, doi:10.3390/en16104012.

93. Vidal de Oliveira, A.K.; Bedin, C.; de Andrade Pinto, G.X.; Mendes Ferreira Gomes, A.; Souza Reis, G.H.; Rafael do Nascimento, L.; Ruther, R. Low-Cost Aerial Electroluminescence (AEL) of PV Power Plants. In Proceedings of the 2019 IEEE 46th Photovoltaic Specialists Conference (PVSC); IEEE, June 2019; pp. 0532–0537.

94. Adams, J.; Doll, B.; Buerhop, C.; Pickel, T.; Teubner, J.; Camus, C.; Brabec, C.J. Non-Stationary Outdoor EL-Measurements with a Fast and Highly Sensitive InGaAs Camera. In Proceedings of the 32nd European Photovoltaic Solar Energy Conference and Exhibition; 2016; pp. 1837–1841.

95. Hernández-Callejo, L.; Gallardo-Saavedra, S.; Morales-Aragonés, J.I.; Alonso-Gómez, V.; Plaza, A.R.; Martínez, D.F. Methodology for Inspection of Defects in Photovoltaic Plants by Drone and Electroluminescence. In Proceedings of the Communications in Computer and Information Science; 2022; Vol. 1555 CCIS.

96. Dos Reis Benatto, G.A.; Mantel, C.; Spataru, S.; Santamaria Lancia, A.A.; Riedel, N.; Thorsteinsson, S.; Poulsen, P.B.; Parikh, H.; Forchhammer, S.; Sera, D. Drone-Based Daylight Electroluminescence Imaging of PV Modules. *IEEE J Photovolt* 2020, *10*, 872–877, doi:10.1109/JPHOTOV.2020.2978068.

97. Del Prado Santamaría, R.; Dos Reis Benatto, G.A.; Kari, T.; Morino, L.; Poulsen, P.B.; Spataru, S. V Challenges of Aerial Drone Electroluminescence in Solar Photovoltaic Field Inspections. In Proceedings of the 40th European Photovoltaic Solar Energy Conference and Exhibition; 2023.

98. Ciulla, G.; Lo Brano, V.; Di Dio, V.; Cipriani, G. A Comparison of Different One-Diode Models for the Representation of I–V Characteristic of a PV Cell. *Renewable and Sustainable Energy Reviews* 2014, *32*, 684–696, doi:10.1016/j.rser.2014.01.027.

99. Morales-Aragonés, J.I.; Williams, M.St.M.; Gómez, V.A.; Gallardo-Saavedra, S.; Redondo-Plaza, A.; Fernández-Martínez, D.; Sánchez-Pacheco, F.J.; Cuadro, J.G.F.; Hernández-Callejo, L. A Resonant Ring Topology Approach to Power Line Communication Systems within Photovoltaic Plants. *Applied Sciences* 2022, *12*, 7973, doi:10.3390/app12167973.

100. Morales-Aragones, J.I.; Williams, M.St.M.; Kupolati, H.; Alonso-Gómez, V.; Gallardo-Saavedra, S.; Redondo-Plaza, A.; Muñoz-García, M.Á.; Sánchez-Pacheco, F.J.; Hernández-Callejo, L. A Power-Line Communication System Governed by Loop Resonance for Photovoltaic Plant Monitoring. *Sensors* 2022, *22*, 9207, doi:10.3390/s22239207.

101. Redondo-Plaza, A.; Velasco-Bonilla, A.Z.; Morales-Aragones, J.I.; Zorita-Lamadrid, Á.L.; Alonso-Gómez, V.; Hernández-Callejo, L. Electroluminescence Imaging Based on FFT Analysis for Outdoor Photovoltaic Module Inspection: A Self-Powered Signal Modulation Approach. *Applied Sciences* 2025, *15*, 4606, doi:10.3390/app15094606.

102. dos Reis Benatto, G.A.; Kari Hass, T.; Del Prado Santamaria, R.; Viorel Spataru, S. Daylight Electroluminescence Imaging Methodology Comparison. In Proceedings of the roceedings of 40th European Photovoltaic Solar Energy Conference and Exhibition; 2023.

103. Tradacete-Ágreda, M.; Santiso-Gómez, E.; Rodríguez-Sánchez, F.J.; Hueros-Barrios, P.J.; Jiménez-Calvo, J.A.; Santos-Pérez, C. High-Performance IoT Module for Real-Time Control and Self-Diagnose PV Panels under Working Daylight and Dark Electroluminescence Conditions. *Internet of Things* 2024, *25*, 101006, doi:10.1016/j.iot.2023.101006.

104. Morales-Aragonés, J.I.; Gallardo-Saavedra, S.; Alonso-Gómez, V.; Sánchez-Pacheco, F.J.; González, M.A.; Martínez, O.; Muñoz-García, M.A.; Alonso-García, M. del C.; Hernández-Callejo, L. Low-Cost Electronics for Online I-V Tracing at Photovoltaic Module Level: Development of Two Strategies and Comparison between Them. *Electronics (Basel)* 2021, *10*, 671, doi:10.3390/electronics10060671.

105. Ortega, E.; Aranguren, G.; Jimeno, J.C. New Monitoring Method to Characterize Individual Modules in Large Photovoltaic Systems. *Solar Energy* 2019, *193*, 906–914, doi:10.1016/j.solener.2019.09.099.

106. Khan, O.; Xiao, W.; Zeineldin, H.H. Gallium-Nitride-Based Submodule Integrated Converters for High-Efficiency Distributed Maximum Power Point Tracking PV Applications. *IEEE Transactions on Industrial Electronics* 2016, *63*, 966–975, doi:10.1109/TIE.2015.2491888.

107. Pilawa-Podgurski, R.C.N.; Perreault, D.J. Submodule Integrated Distributed Maximum Power Point Tracking for Solar Photovoltaic Applications. *IEEE Trans Power Electron* 2013, *28*, 2957–2967, doi:10.1109/TPEL.2012.2220861.

108. Moorthy, J.G.; Manual, S.; Moorthi, S.; Raja, P. Performance Analysis of Solar PV Based DC Optimizer Distributed System with Simplified MPPT Method. *SN Appl Sci* 2020, *2*, 220, doi:10.1007/s42452-020-2010-2.

109. Fathy, A.; Atitallah, A. Ben; Yousri, D.; Rezk, H.; Al-Dhaifallah, M. A New Implementation of the MPPT Based Raspberry Pi Embedded Board for Partially Shaded Photovoltaic System. *Energy Reports* 2022, *8*, 5603–5619, doi:10.1016/j.egyr.2022.04.035.

110. Azab, M. DC Power Optimizer for PV Modules Using SEPIC Converter. In Proceedings of the 2017 IEEE International Conference on Smart Energy Grid Engineering (SEGE); IEEE, August 2017; pp. 74–78.

111. de Morais, J.C. dos S.; de Morais, J.L. dos S.; Gules, R. Photovoltaic AC Module Based on a Cuk Converter With a Switched-Inductor Structure. *IEEE Transactions on Industrial Electronics* 2019, *66*, 3881–3890, doi:10.1109/TIE.2018.2856202.

112. Sajadian, S.; Ahmadi, R. Distributed Maximum Power Point Tracking Using Model Predictive Control for Photovoltaic Energy Harvesting Architectures Based on Cascaded Power Optimizers. *IEEE J Photovolt* 2017, *7*, 849–857, doi:10.1109/JPHOTOV.2017.2680601.

Annex I: Electronic Schematics

The present Annex includes schematic of the following developments:

1. Schematic of the module-level electronic device for EL and PL modulation
2. Schematic of the module-level PV optimizer with non-invasive PL modulation and I-V tracing functionalities

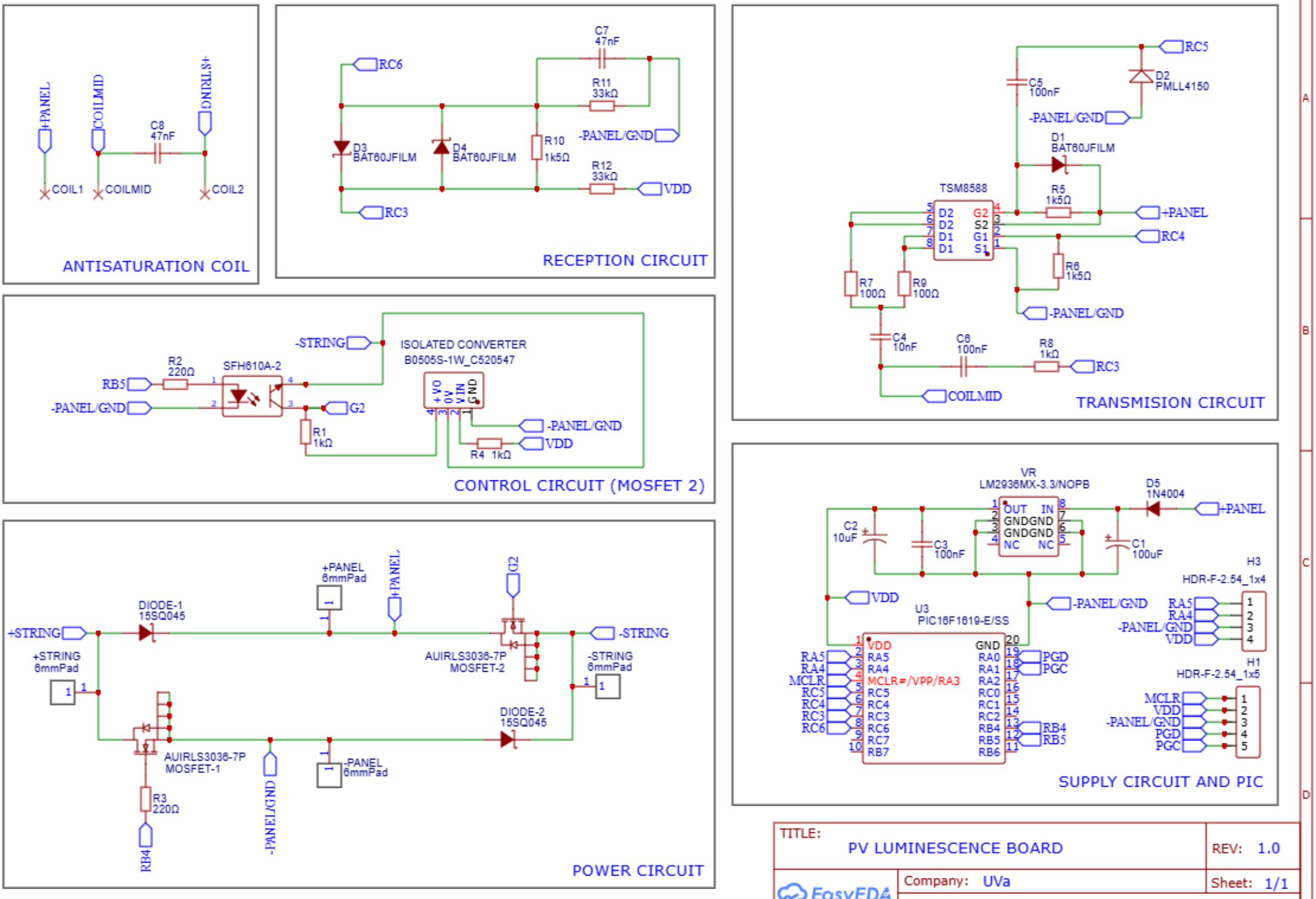
+PANEL
COILMID
-STRING
C8
47nF
COIL1
COILMID
COIL2
ANTISATURATION COIL
RC6
C7
47nF
R11
33kΩ
D3
BAT60JFILM
D4
BAT60JFILM
R10
1k5Ω
-PANEL/GND
R12
33kΩ
VDD
RC3
RECEPTION CIRCUIT
RC5
C5
100nF
D2
PMLL4150
-PANEL/GND
D1
BAT60JFILM
TSM8588
R5
1k5Ω
+PANEL
RC4
R6
1k5Ω
R7
100Ω
R9
100Ω
-PANEL/GND
C4
10nF
C6
100nF
R8
1kΩ
RC3
COILMID
TRANSMISION CIRCUIT
-STRING
ISOLATED CONVERTER
B0505S-1W_C520547
R2
220Ω
SFH610A-2
RB5
-PANEL/GND
G2
R1
1kΩ
-PANEL/GND
VDD
R4 1kΩ
CONTROL CIRCUIT (MOSFET 2)
VR
LM2936MX-3.3/NOPB
D5
1N4004
+PANEL
C2
10uF
C3
100nF
C1
100uF
H3
HDR-F-2.54_1x4
VDD
U3
PIC16F1619-E/SS
-PANEL/GND
RA5
RA4
-PANEL/GND
VDD
MCLR
RC5
RC4
RC3
RC6
PGD
PGC
RB4
RB5
H1
HDR-F-2.54_1x5
MCLR
VDD
-PANEL/GND
PGD
PGC
SUPPLY CIRCUIT AND PIC
+PANEL
6mmPad
+PANEL
G2
DIODE-1
15SQ045
+STRING
-STRING
+STRING
6mmPad
AUIRLS3036-7P
MOSFET-2
-STRING
6mmPad
DIODE-2
15SQ045
AUIRLS3036-7P
MOSFET-1
-PANEL
6mmPad
R3
220Ω
RB4
-PANEL/GND
POWER CIRCUIT
TITLE:
PV LUMINESCENCE BOARD
REV: 1.0
EasyEDA
Company: UVa
Sheet: 1/1
Date: 2024-02-20
Drawn By: alberredon

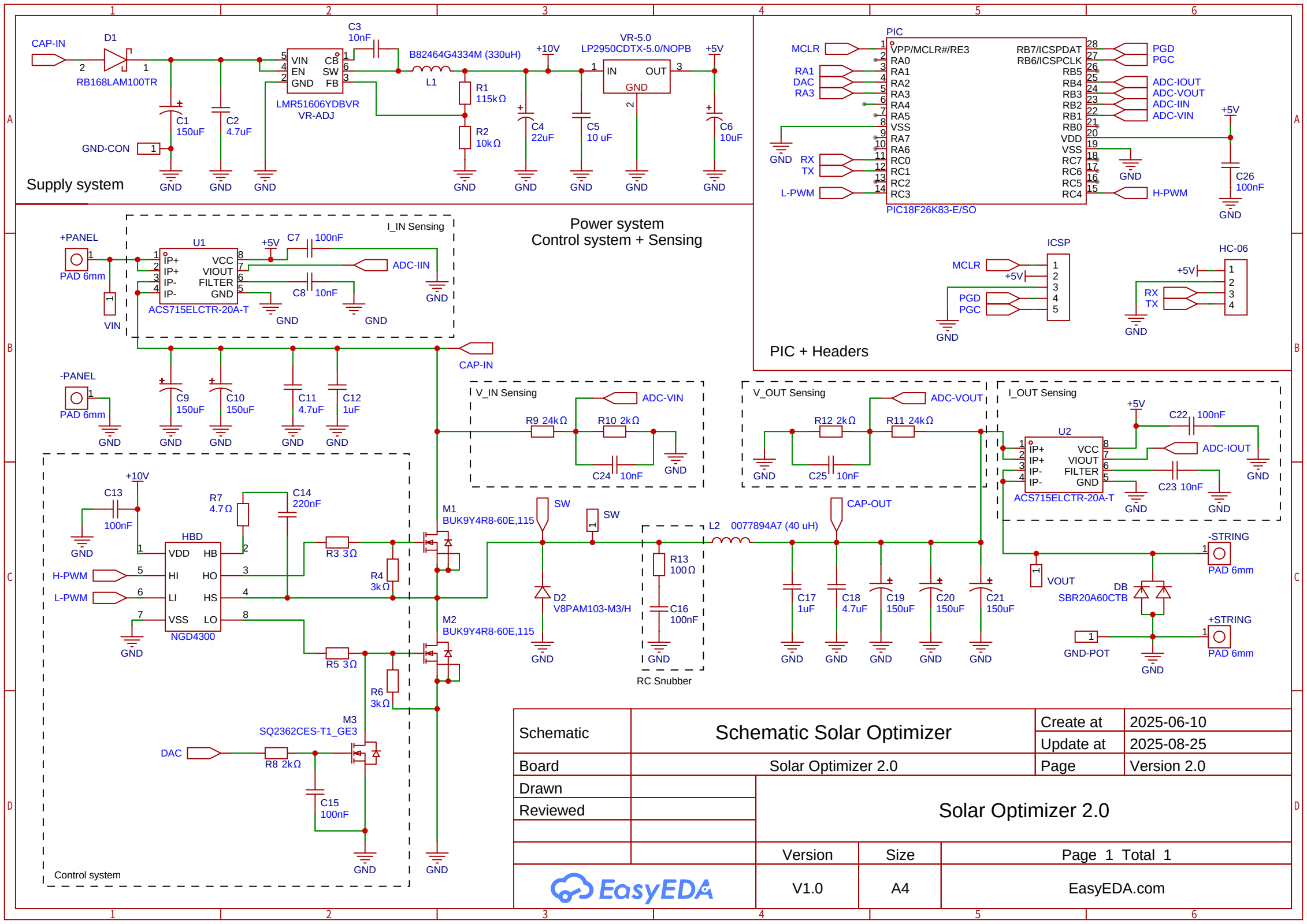

Schematic	Schematic Solar Optimizer	Create at	2025-06-10
		Update at	2025-08-25
Board	Solar Optimizer 2.0	Page	Version 2.0
Drawn		Solar Optimizer 2.0	
Reviewed			
		Version	Size / Page 1 Total 1
EasyEDA		V1.0	A4 / EasyEDA.com